Aix-Marseille Université
Numéro d'ordre :

THÈSE

Ecole doctorale Physique et Sciences de la matière
Mention : **matière condensée et nanosciences**

Pour obtenir le grade de :

Docteur en Sciences des matériaux, Physique, Chimie et Nanosciences d'Aix-Marseille Université

XAS-XEOL and XRF spectroscopies using Near-Field Microscope probes for high-resolution photon collection

Présentée par :

Maël DEHLINGER

Soutenue publiquement le vendredi 27 Septembre 2013 devant le jury suivant :

Rapporteurs :	Alexei ERKO – Helmholtz Zentrum Berlin
	Thierry GROSJEAN – FEMTO-ST Besançon
Examinateurs :	Jean-Marc THEMLIN – IM2NP Marseille
	Florence MARCHI – Institut Néèl Grenoble
Directeurs de thèse :	Didier TONNEAU – CINaM Marseille
	Carole FAUQUET – CINaM Marseille

Préparée au Centre Interdisciplinaire de Nanosciences de Marseille (Aix-Marseille Université, CINaM, 13288, Marseille, France).

To my parents Claudine and François…

Acknowledgements

I would like to thank everybody I met during this three-year work, researchers, students or university and laboratory staff. You made this thesis period an unforgettable one.

I am thankful to Dr Claude Henry, the CINaM manager, for having welcomed me in his laboratory and for allowing to perform this work.

I express my gratitude to my thesis manuscript reviewers, Prof Alexei Erko and Dr Thierry Grosjean, for spending valuable time to examine this work. I am also grateful to Prof Jean-Marc Themlin and Dr Florence Marchi for honouring me with their presence to my PhD thesis defense.

I cannot thank enough my tutors Prof Didier Tonneau and Dr Carole Fauquet for their guidance, availability and support during my PhD thesis. I am very grateful to them for having given me the time they don't necessary had to answer my questions and giving me precious advices. They also gave me a great help in manuscript writing, they shared my burden by the endless hours spent of reading in order to give me suggestions and corrections to finalize this manuscript. It was an honour to be your student.

I want to express my enormous gratitude to people that worked with us on the project. Franck Jandard who designed, built, made userfriendly and tested the laboratory test-bed. Moreover I want to thank him for the everyday assistance he gave me during the period he was here. I learnt a lot from all his skills on electronic devices and experimental setup crafting in a more general way. Thanks to Sebastien Lavandier for his kindness and help. This work wouldn't have been possible without Marcel Fernandez who fabricated with accuracy, acre and great sympathy the small mechanical parts of our experimental setup. I also want to thank Bruno Gely for the IT support and everyday kindness, Vasile Heresanu for our long discussions about X-rays and for checking that we worked in perfect conditions of safety and Artak Karapetyan for his advices, sympathy and for sharing his knowledge about ZnO and luminescence.

Thanks to the students who work with us as a training period: Chloé Dorczynski, Orawan Aumporn and Pauline Truc, for their participation in the experiments, their great interest in our area of research thematic and their cheerfulness. This work is partially theirs.

Thank you very much Frederic Bedu, Igor Ozerov and Romain Jeanette from the PLANETE nanofabrication facility, Philippe Bindzi from the laboratory workshop, Serge Nitsche and Damien Chaudanson from the electron microscopy service, Andres Saul and

Alexandre Zapelli who gave me helpful advices for the simulation task and guides me for the material available in the laboratory for simulation.

I would like to thank people I met during our European project meetings: Dr Aniouar Bjeoumikhov, Dr Zemfira Bjeoumikhova and Dr Vladimir Arkadiev from the IfG - Institute for Scientific Instruments GmbH, Dr Ivo Zizak from synchrotron BESSY, Dr Brahim Dahmani from Lovalite and Dr Sylvain Ferrero and Dr Daniel Pailharey from Axess-tech. I was very glad to meet you. Sylvain and Daniel came often as neighbours in the CINaM plant. It was always a real pleasure to see you.

Thanks to every people at the CINaM TPR1 4^{th} and 5^{th} floor. Your everyday sympathy was like a ray of sunshine every morning. I really spent a good time with you.

I want to thank the other CINaM PhD students I met during my stay. We can rely on each other to discuss about administrative problems and spend good time. I want especially to thank Racha Elzein and Ahmad Kenaan that shared the office with me and Roland Roche, Manuel Ildefonso and Pierre Dillard who gave their friendship everyday not only in the laboratory but also out of it when we spent time for hobbies. Thanks to Christian Davesnne for his long time friendship since our first year in university.

And last but not least, many thanks to my parents François Dehlinger and Claudine Dehlinger-Saunier, to my brother Flavien and my sister Coralie who encouraged me for many years and who gave me very useful advices. I think to my two nephews Milo and Kawrantin who are the most amazing little guys I know and to my so beautiful niece Leann. They remind me there is a life out of the thesis and out of university. Heartfelt thanks to my beloved Emilie who has been sharing my life since many years. You are always present for me even if you had to go to work very far away from Marseille. Without you I don’t know if I had strength enough to achieve this thesis. Thank you my love!

Résumé

L'analyse chimique élémentaire non-destructive à haute resolution latérale demeure un enjeu important pour les domaines des sciences de la vie et de la physique. Par exemple les industries du verre et de l'électronique (RRAM, FeRAM, smart materials, cellules solaires) ont besoin d'instruments de caractérisation de résolution latérale inférieure à 100nm pour le traitement des matériaux, l'optimisation des procédés, le contrôle de spécifications et l'analyse de défaillance [1].

Les microscopes en champ proche (Scanning Probe Microscopes (SPM)) ont largement participé à l'essor des nanosciences, offrant pour la première fois, et dans l'espace direct, la possibilité d'effectuer de la microscopie jusqu'à la résolution atomique [2]. Ces équipements permettent différentes spectroscopies in-situ pour sonder les propriétés locales de la surface via la pointe du microscope (propriétés magnétiques, états électroniques, adhésion…). Cependant il n'est pas possible d'effectuer une cartographie chimique de l'échantillon sans connaître la composition *a priori* de celui-ci. Durant les dix dernières années, de nombreux instruments de caractérisation ont ainsi été développés pour obtenir l'imagerie de la surface et la cartographie chimique avec le même appareil.

Ainsi, la toute première idée concernant la combinaison d'un SPM avec une analyse chimique locale est proposée au tout début des années 90 avec Gimzewsky [3]. L'expérience consiste en la collecte locale de photoélectrons par la pointe d'un Microscope à Effet Tunnel (Scanning Tunneling Microscope (STM)) sous ultravide pendant que la région pointe-échantillon est illuminée par une lampe à halogène. Gimzewzky obtint une cartographie de contraste de photoémission en utilisant le photocourant généré en tant que signal de régulation, révélant ainsi des structures émettrices d'échelle submicroniques. Cependant une connaissance *a priori* de la surface était toujours nécessaire pour l'interprétation des données.

Les spectroscopies de rayons-X sont des techniques très précises qui peuvent fournir de manière non-destructive, des informations chimiques émanant de la surface ou de la profondeur d'un échantillon aussi bien que sa caractérisation structurelle. Avec le développement des nanosciences, la tendance générale concernant les spectroscopies de rayons-X sur les lignes de faisceaux synchrotrons est d'augmenter la résolution latérale en diminuant la taille du faisceau d'illumination. Compte tenu du faible rendement des optiques focalisatrices, des détecteurs à grande ouverture ont été développés en parallèle. Malgré le fait qu'une haute résolution latérale de l'ordre de 30 nm puisse être obtenue sur les lignes de

lumière les plus performantes, il demeure impossible d'aligner la tache d'illumination primaire à un endroit spécifique sur la surface. C'est la raison pour laquelle coupler la spectroscopie de rayons-X avec la microscopie à sonde locale pour obtenir simultanément la topographie d'un échantillon et sa cartographie chimique à très haute résolution latérale devrait jouer un rôle important dans le domaine des nanosciences dans un futur proche. L'idée est de garder une tache d'illumination de rayons-X très brillante et de collecter localement le signal provenant de la surface avec une haute résolution latérale via la pointe-sonde d'un SPM.

Les premières expériences dans ce domaine ont été effectuées en environnement synchrotron afin de bénéficier d'une source très brillante. Cela est toujours la voie suivie par plusieurs équipes à travers le monde. En effet, Tsuji et al. [4] ont mesuré l'émission totale d'électrons (Total Electron Yield (TEY)) avec la pointe d'un Microscope à Effet Tunnel tout en faisant varier l'énergie du faisceau primaire de part et d'autre du seuil d'absorption des éléments composants la surface (Ni et Au). Ils ont obtenu des spectres similaires à ceux de Spectroscopie Étendue de Structure Fine d'Absorption de Rayons-X (Extended X-ray Absorption Fine Structure, EXAFS) et de spectroscopie de structure au voisinage du seuil d'absorption de rayons X (X-ray Absorption Near Edge Spectroscopy, XANES) en traçant le courant pointe-échantillon en fonction de l'énergie des photons-X incidents. Eguchi et al. ont aussi fait des mesures de TEY sur un motif de test consistant en un échiquier de Fe et Ni [5]. En fixant l'énergie de l'illumination X au-dessus et en-dessous des seuils d'absorption du Fe et du Ni, ils ont été capable d'obtenir des images spécifiques de chaque élément avec une résolution latérale de 10nm.

Ching-Yuan Chiu et al. ont simulé la collection de photoélectrons via une nano-pointe sous illumination synchrotron [6]. Ils ont montré qu'en champ proche, le courant de photoélectrons seul ne peut pas expliquer le niveau de photocourant collecté par la pointe du STM. En effet une part non-négligeable du signal total vient des électrons secondaires. Les différentes contributions du courant total sont détaillées par V. Rose et al. [7]. Le développement de pointes recouvertes de 500nm d'une couche de SiO_2 isolant exceptés à l'apex (longueur inférieure à 0.5µm) est aussi présenté [8, 9], comme précédemment conseillé par Gimzewski [3].

Saito et al. ont détecté une modulation du courant de pointe sur des nano-îlots de Ge sur Si(111) alors qu'il faisaient varier l'énergie du faisceau primaire de rayons-X autour du seuil d'absorption K du Ge [10]. Ils ont été capables d'identifier un nano-îlot de Ge en

mesurant son seuil d'absorption, en l'imageant et en faisant la cartographie du courant pointe-échantillon au-dessus et en-dessous du seuil.

Récemment, une combinaison entre SPM et STXM (Scanning Transmission X-ray Microscopy, Microscopie à Balayage par Transmission de Rayons X) fut développée par Schmid et al. [11]. Dans cette expérience, le faisceau de rayons-X est focalisé sur un échantillon semi-transparent. Le faisceau transmis est habituellement collecté par une photodiode. Cependant, les auteurs ont remplacé la photodiode par une pointe d'AFM spécialement conçue pour collecter les photoélectrons. La résolution latérale de cette technique est limitée par la taille du faisceau d'illumination primaire et les auteurs soutiennent qu'une résolution spatiale de 20nm peut être atteinte.

Ishii et al. ont proposé une méthode utilisant de la Microscopie Capacitive par Balayage (Scanning Capacitance Microscopy (SCM)) sous rayonnement synchrotron [12]. L'irradiation X entraîne la photoionisation des défauts de surface qui relâchent les porteurs libre piégés. La valeur de capacité entre la pointe et l'échantillon est sensible à cette modification. En mesurant la variation de cette capacité, les auteurs peuvent faire une cartographie des défauts piégeurs d'électrons près de la surface d'un semiconducteur [13]. Finalement, la dépendance sur l'énergie des photons de la valeur de la capacité fournit un spectre XAFS concernant les sites de défaut. [12]. Ishii et Hamilton ont également conçu un Microscope à sonde de Kelvin (Kelvin Force Microscope (KFM)) combinée avec une source de rayons-X (X-KFM) pour étudier les états électroniques des centres piégeurs d'électrons [14]. Ils sont capables d'effectuer simultanément de la topographie AFM (Atomic Force Microscope, Microscope à Force Atomique) conventionnelle et de la mesure locale X-KFM afin de localiser les sites piégeurs. L'appareil est aussi capable d'effectuer des spectres similaires au XAS (X-ray Absorption Spectroscopy, spectroscopie d'absorption de rayons-X) à une position donnée de la pointe en traçant la force Kelvin en fonction de l'énergie incidente.

L'observation locale des propriétés élastiques de nanostructures fut effectuée par Chevrier et al. en combinant un AFM avec de la micro diffraction de rayons-X [15]. Les motifs de diffraction X sont enregistrés par un réseau bidimensionnel d'éléments de détecteur pendant que la pointe d'AFM applique une pression sur un cristal de taille micrométrique. Ce travail est effectué en utilisant une microsource à rayons-X. Cela permet la mesure du module d'élasticité du cristal.

Pilet et al. se sont concentrés sur plusieurs modes conventionnels de l'AFM tels que le non-contact, le contact-intermittent, la Microscopie à Force Magnetique (Magnetic Force

Microscopy (MFM)) ou la Microscopie à sonde de Kelvin (KFM) aussi bien que sur les mesures STXM [16]. Ainsi ils ont pu caractériser différents types d'échantillons : des mélanges de polymères, une nanostructure de Cr/Ti fabriqué par lithographie et des multicouches magnétiques.

Dans ce contexte, le Centre Interdisciplinaire de Nanoscience de Marseille a aussi développé une tête de microscope SNOM-SFM (Scanning Near-Field Optical Microscope – Shear Force Microscope, Microscope Optique en Champ Proche – Microscope à Force de Cisaillement) testé dans un premier temps en acquisition XAS-XEOL locale (X-ray Absorption Spectroscopy – X-Ray Excited Optical Luminescence, Spectroscopie d'absorption de rayons-X – Luminescence Optique Induite par Rayonnement-X) au synchrotron ESRF dans le cadre d'un premier projet européen ('X-Tip', Strep program # NMP4-CT-2003-505634). L'objectif est ici d'obtenir un appareil de laboratoire équipé avec une source de laboratoire qui offre un rapport signal/bruit significatif. Cette étude fut financée par un second projet européen ('LUMIX', Eureka # E4383). Il faut noter que la luminescence collectée n'a pas de corrélation avec le signal de la boucle de régulation du Microscope à Force de Cisaillement utilisé pour le contrôle de la distance pointe-échantillon. Cela permet d'éviter la présence d'artefacts dans l'acquisition des images due à une variation de la distance pointe-échantillon durant l'illumination par rayons-X.

Dans ce travail nous avons démontré que coupler la Microscopie à Sonde Locale avec la Spectroscopie à Rayons-X peut permettre l'obtention simultanée de la topographie d'un échantillon et de la cartographie de luminescence ou la spectroscopie locale d'un échantillon.

Le **Chapitre I** présente les principes des techniques expérimentales utilisées. La Microscopie en Champ Proche et particulièrement la Microscopie à Force de Cisaillement (SFM) sont décrits. Le domaine de la spectroscopie de Rayons-X est également présenté, en particulier la Spectroscopie de Fluorescence-X (XRF) et la Spectroscopie XAS-XEOL. Les optiques de focalisation des rayons-X, lentilles monocapillaires et polycapillaires, sont décrites.

La cartographie locale de luminescence visible induite par rayons-X en utilisant la pointe d'un SNOM est reportée dans le **Chapitre II**. Ces expériences ont été effectuées avec succès avec différentes types de sources : Rayonnement synchrotron (résultats obtenus par Larcheri et al. dans une précédente thèse [17]), un laser He-Cd et même une source à rayons-X de faible puissante microfocalisée. Le banc d'essai utilisé pour ces expériences est décrit figure R.1.

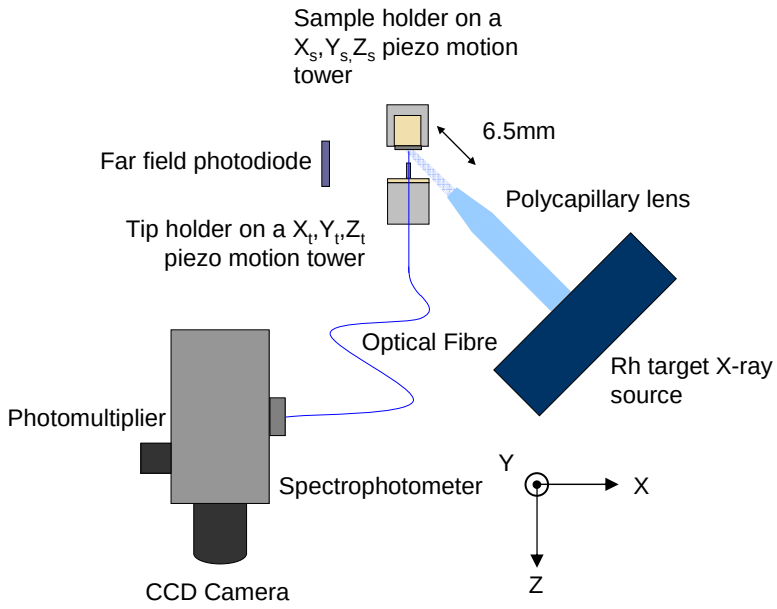

Fig.R.1*: Montage experimental de la cartographie simultanée de luminescence et de la topographie grâce à la pointe-sonde du SNOM.*

Afin de maintenir constant l'alignement entre la pointe et le faisceau primaire X, nous avons choisi de garder la pointe à une position fixe vis-à-vis du faisceau primaire tandis que l'échantillon est déplacé dans un plan perpendiculaire au porte pointe durant le processus d'imagerie. Pour cette raison, l'échantillon est placé sur un tube piezoscanner commercial de déplacement x, y, z de marque NT-MDT. Le déplacement fin est opéré via ce scanner et la fenêtre maximale de déplacement est de 120µm x 120µm. L'élongation maximale du piezo dans la direction x (contrôlée par la boucle de régulation du microscope) est environ de 5µm. Le scanner est fixé sur une tour de déplacement piézoélectrique (Attocube, ACN150) permettant une déplacement plus grossier de l'échantillon selon les axes X_s, Y_s et Z_s.

La pointe est une fibre optique effilée recouverte d'aluminium (diamètre d'ouverture : 70nm, bande passante : 400-600nm) collée sur un diapason de quartz oscillant à 32kHz. Ce système est disponible sur le marché et est soudé sur une carte de circuit imprimé équipé de trois aimants. Les deux contacts du diapason sont connectés via deux des trois aimants. Ce dispositif est placé sur le porte-échantillon équipé de trois aimants et fixé sur une autre tour de déplacement piézoélectrique X_t, Y_t, Z_t (Attocube ACN150). Le diapason est alimenté via les contacts des aimants. La pointe est perpendiculaire à la surface de l'échantillon. Tout ce système tient sur une bride métallique de 20cm de diamètre et est solidaire à un système d'amortissement.

Durant le scan topographique, le signal de luminescence émis par l'échantillon sous l'illumination X est collecté à travers la fibre optique effilée et est guidée soit vers une

photodiode pour la collecte de toute la luminescence soit vers un spectrophotomètre (Princeton SP2300) pour l'acquisition de spectres de luminescence. Le signal du photomultiplicateur est envoyé vers le système d'acquisition de donnée du contrôleur SMENA qui permet d'afficher les images jumelles de cartographie topographique et de luminescence visible.

La résolution latérale de la technique est principalement donnée par l'ouverture de fibre optique (70nm dans notre cas) et le rayon de courbure de l'apex (100nm) pour la topographie.

L'enjeu de ces expériences est l'obtention d'un rapport signal/bruit suffisant avec une source de rayons-X de laboratoire micro-focalisée en utilisant une lentille polycapillaire. Voici un résumé de la section II.2.3 illustrant ce concept.

Un échantillon composé d'un mélange de poudres de ZnO/ZnS incorporé dans de la résine PMMA sur un substrat de silicium fut utilisé pour le test du banc d'essai. Une distribution de taille de grains comprise entre 2.5 et 35µm fut observée par microscopie optique. L'échantillon fut aussi observé par Microscope Electronique à Balayage (Scanning Electronic Microscope (SEM)) associé à de l'analyse EDX *in-situ* (Energy Dispersive X-ray spectroscopy, analyse dispersive en énergie), et deux types de grains de morphologie et de composition différente furent repérés (Fig R.2). Ils sont respectivement principalement composés de ZnO et de ZnS.

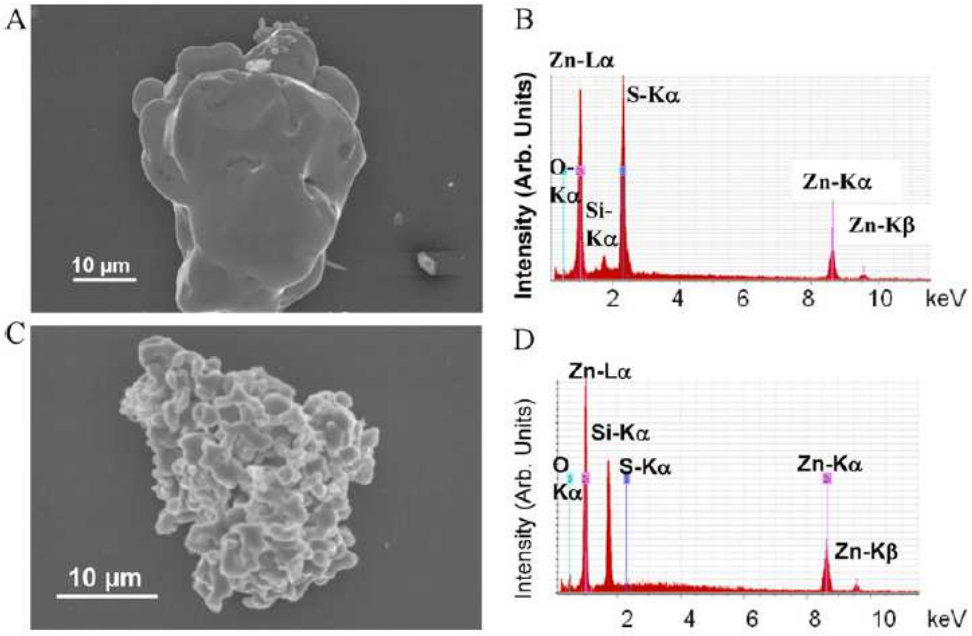

Fig R.2: *(a) et (c) images SEM de grains de ZnO et de ZnS incorporés dans de la résine PMMA sur un substrat de silicium. (b) et (d) Analyse EDX des grains présentés respectivement en (a) et en (c). Energie du faisceau primaire : 15keV.* [18]

Un spectre de photoluminescence a été acquis en champ lointain à l'aide d'une fibre optique de 400µm de diamètre de cœur positionnée à environ 10mm de l'échantillon. Le spectre (Fig. R.3) présente deux gaussiennes centrées à 458 et 524nm ce qui correspond respectivement aux pics de défaut du ZnS [19] et du ZnO [20, 21]. Les pics excitoniques correspondants au ZnS (à environ 323-353nm) [13] et au ZnO (380nm) [22] sont hors de la bande passante de la fibre optique et ne peuvent être détectés.

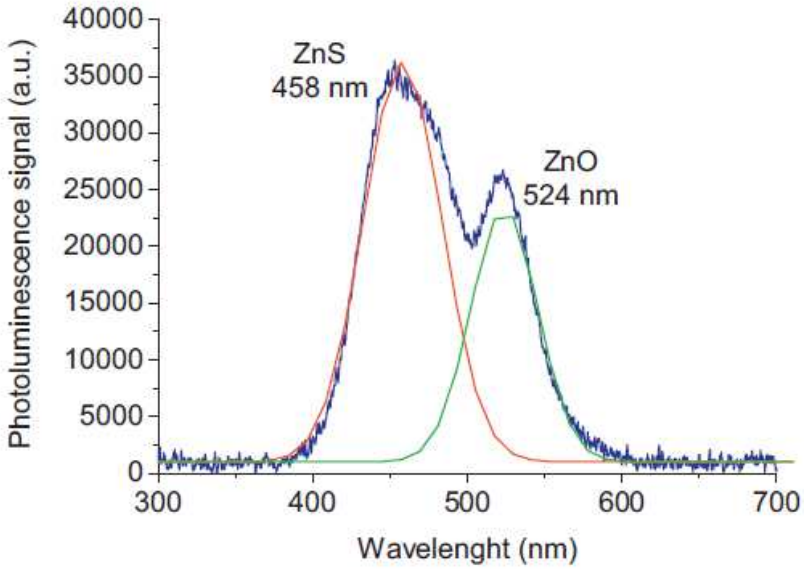

Fig R.3: *Spectre de luminescence d'un groupement de grains de ZnO/ZnS sur un substrat de Si. L'acquisition est effectuée en champ lointain en utilisant une fibre optique de grand diamètre de cœur (400 nm) [18].*

Ensuite une acquisition simultanée de luminescence et de la topographie fut effectuée avec notre microscope SNOM sous illumination de rayons-X produits par une source à cible de Rh. Les images sont présentées figure R.4. Le champ visualisé est de 115µm x 115µm. Concernant la cartographie de luminescence (acquise simultanément à la topographie) (Fig. R.4b)), le spectromètre est centré sur 524nm, longueur d'onde du pic de défaut du ZnO.

L'image topographique (Fig. R.4a)) montre un grain d'environ 20µm de diamètre de hauteur de l'ordre de grandeur de l'élongation maximale du piezo-Z. Ceci explique le phénomène de saturation dans le niveau de couleur du grain.

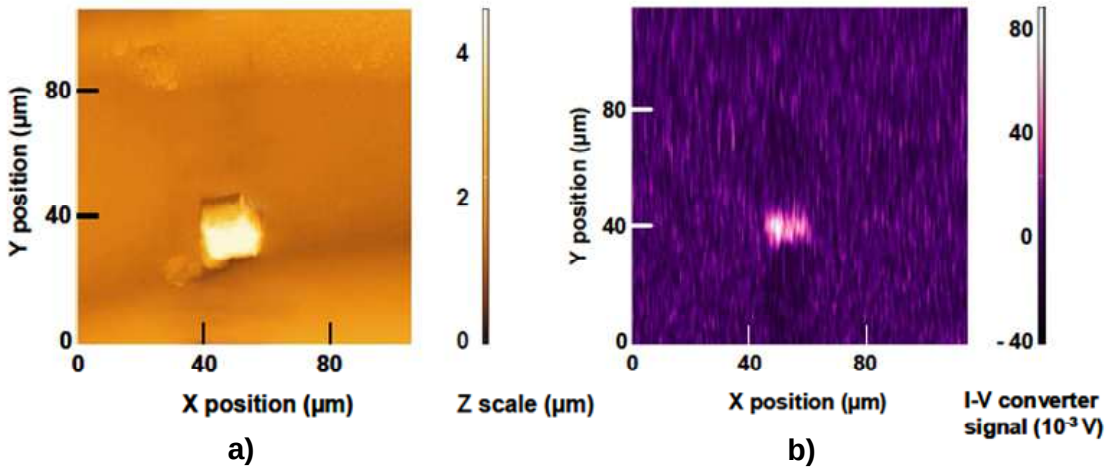

Fig R.4: *Imagerie d'un échantillon de ZnS/ZnO en utilisant notre Microscope à Force de Cisaillement. La fenêtre de scan est de 115µm×115µm. (a) Image topographique (b) et cartographie de luminescence simultanée. Le spectromètre est centré à 524nm, longueur d'onde correspondant aux pics de défaut du Zn0* [18].

La luminescence vient principalement du centre de l'agrégat. De plus aucun signal significatif correspondant à la longueur d'onde du pic de défaut du ZnS n'a pu être mesuré dans la même région (spectre non montré ici). Ceci indique que les centres émetteurs responsable de l'émission de la luminescence sont principalement du ZnO et que l'agrégat imagé est principalement composé de ZnO sur ses premiers microns de surface [20, 21].

Le grain semble plus petit sur l'image de luminescence que sur l'image topographique. Ceci peut être dû à de l'émission de lumière hors de l'acceptante de l'apex de la fibre optique comme expliqué dans la section II.2.2 de ce manuscrit (voir fig. II.7)

Cependant l'acquisition de luminescence visible limite l'utilisation de cette technique principalement à la caractérisation des matériaux semiconducteurs. La Spectroscopie de Fluorescence-X (XRF) pourrait être utilisée pour caractériser une plus grande variété d'éléments, les limites étant fixées par l'énergie maximum du faisceau primaire et par la détectabilité des éléments. Ainsi, en remplaçant la fibre optique effilée de la tête SNOM par un capillaire à Rayons-X cylindrique, il serait possible de faire de l'analyse XRF locale. Le **Chapitre III** examine la faisabilité de cette technique. Un banc d'essai sur ce concept a été développé (Fig R.5) et est utilisé afin de déterminer la résolution ultime qui puisse être obtenue.

Un faisceau de rayons-X fourni par une source de faible puissance (35 kV x 800 µA) à cible de Rh est focalisée sur un échantillon à l'aide d'une lentille polycapillaire de distance focale 7mm [23, 18]. L'angle d'incidence du faisceau est de 30° par rapport à la surface.

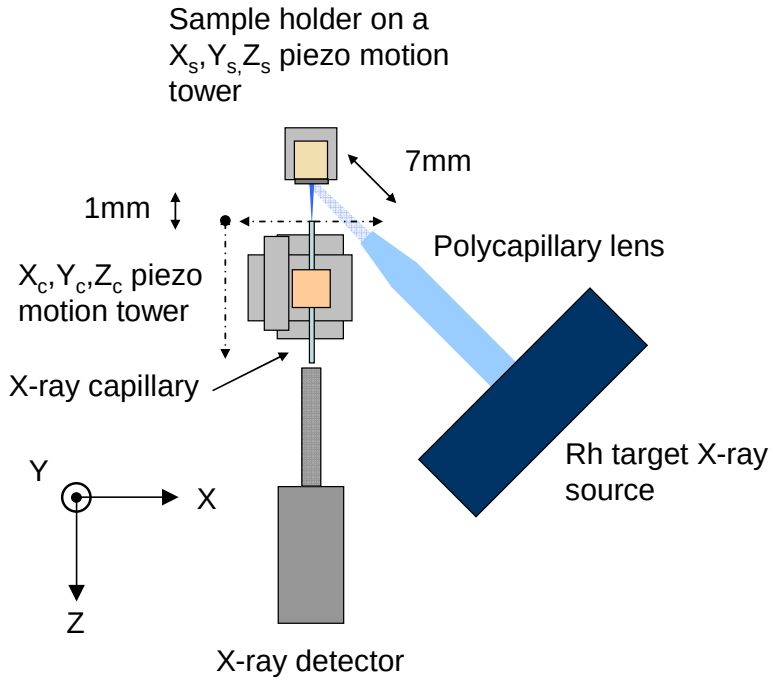

Fig. R.5: *Montage expérimental du banc d'essai de collecte locale de fluorescence X. L'échantillon est placé dans le plan focal de la lentille polycapillaire (7mm). La distance entre l'échantillon et l'extrémité du capillaire cylindrique est de 1mm.*

Les capillaires à rayons-X sont aujourd'hui très utilisés en tant qu'optique de focalisation. L'originalité de ce travail repose sur leur utilisation pour la collection de photons X. Ces optiques offrent la possibilité d'approcher artificiellement un détecteur EDX, évitant l'ombrage du faisceau primaire excitateur. La fluorescence issue de l'échantillon est analysée par un détecteur SDD (Silicon Drift Detector, Brüker GmbH, surface 10mm²) EDX à travers un capillaire à rayons-X de 50mm de long et d'un 1mm de diamètre extérieur. Le capillaire cylindrique est placé sur une tour de déplacement piézoélectrique X_c, Y_c, Z_c autorisant des déplacements par pas 30nm tandis que le détecteur reste dans une position fixe. La distance de travail est fixée à 1mm pour toutes les expériences. Ce choix est justifié dans la section III.2.2.

Les caractéristiques du faisceau excitateur polychromatique (ie la taille du faisceau et le nombre de photons en fonction de l'énergie des photons) ont dans un premier temps été mesurées. Ensuite, nous avons caractérisé la géométrie du volume émetteur de fluorescence d'un échantillon de cobalt pur. Pour cela, le capillaire cynlindrique est positionné sur une tour de déplacement piézoélectrique X_s, Y_s, Z_s. L'influence du rayon du capillaire sur le niveau de signal collecté fut étudiée en utilisant des capillaires de rayons allant de 50 à 0.5 µm.

Le banc de test a ensuite été utilisé en tant que microscope à rayons X pour caractériser deux motifs de test métalliques consistant, l'un en une grille de microscope TEM de molybdène collée sur un échantillon de cobalt, l'autre en des plots de titane mince (200 nm) déposés sur l'échantillon de cobalt. Le pas du motif et la largeur de piste de molybdène sont notés respectivement Φ_{track} et d_{track}. L'expérience est schématiquement représentée fig. R.6. Un capillaire de rayon 25µm est utilisé pour œs mesures. Il est placé à la distance de travail optimale de de 1mm. Pour tracer le profil de l'échantillon nous avons choisi de déplacer l'échantillon dans le plan perpendiculaire au capillaire de collection pour ne pas perdre l'alignement capillaire-faisceau primaire. Tous les 10µm nous enregistrons un spectre XRF et calculons l'aire du pic de Mo Kα (17.4 keV). Ensuite nous reportons chaque valeur sur un graphique en fonction de la position de l'échantillon (Fig. R.7).

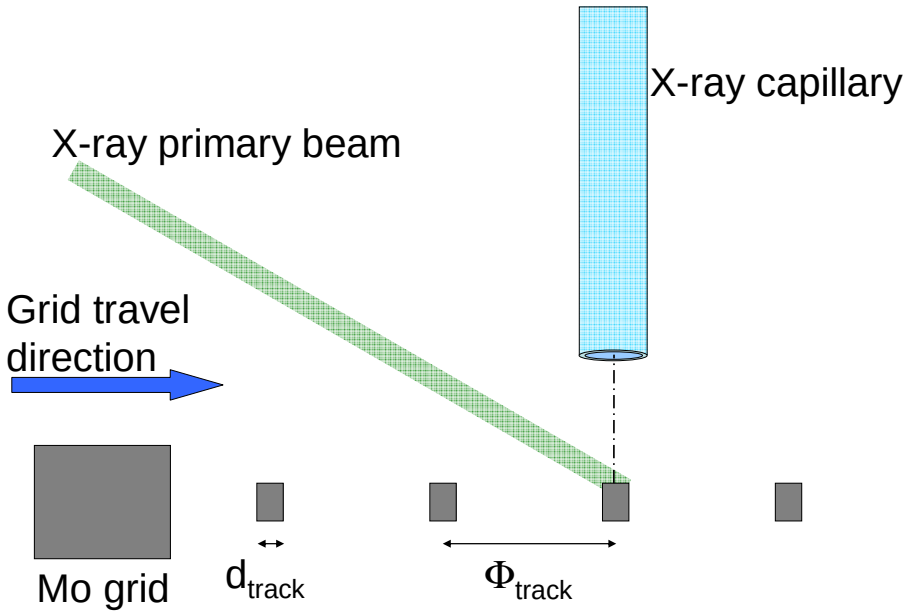

Fig R.6 : *Schéma de la procédure expérimentale pour le profilage XRF. L'échantillon est une grille de TEM en molybdène collée sur du cobalt. La grille est positionnée dans le plan focal de la lentille polycapillaire et est déplacée perpendiculairement à l'axe du capillaire utilisé pour la détection (r_{cap} 25 µm).*

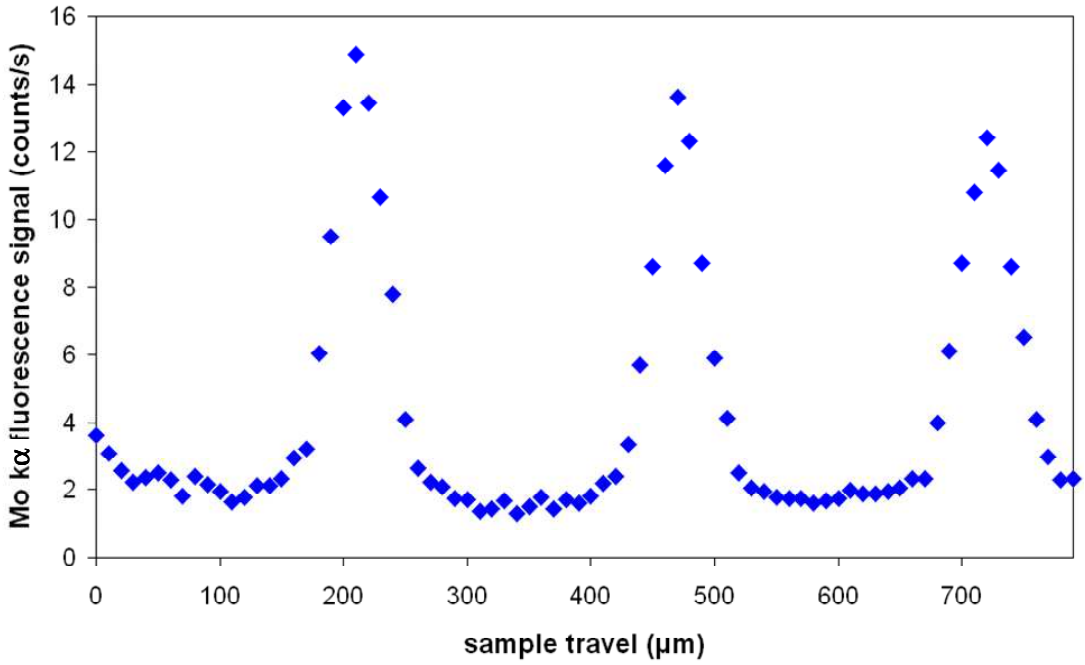

Fig.R.7 : *Variation du signal de Mo kα en fonction de la position de l'échantillon. Le rayon du capillaire de détection est de 25µm.*

La variation du signal du pic de MoKα présente des oscillations qui suivent le motif de la grille. On peut en déduire une distance Φ_{track} moyenne de 255µm en parfait accord avec des mesures effectuées par microscopie optique (251 µm).

Une taille de barreau apparente d_{track} de 88 µm est mesurée, très différente de la valeur 36 µm obtenue par microscopie optique. En effet l'utilisation de capillaire pour la détection XRF entraîne des effets de convolution comme mentionné dans la section III.2.2. Le diamètre du spot d'illumination (22µm de rayon à 1/e du maximum) et le diamètre du capillaire sont du même ordre de grandeur que la taille du barreau. La collection de Mo commence (et finit) alors que la position du capillaire est décalée vis à vis de bords du barreau de molybdène (Fig R.8).

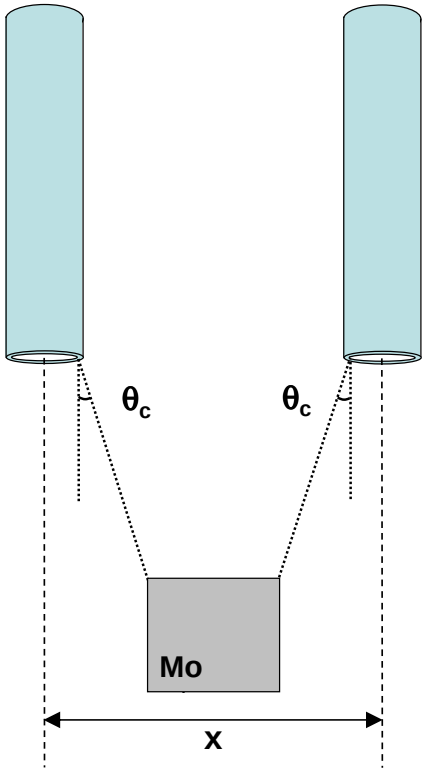

Fig.R.8: *Excursion latérale x du capillaire le long de laquelle un signal de Mo est détecté.*

Tenant compte de ces considérations géométriques, le signal de Mo devrait être détecté le long de la distance x, telle qu'en première approximation:

$$x = 2\ rcap + 2\ WD \tan \theta_{cMo} + d_{track} \qquad \text{Eq (R.1)}$$

où θ_{cMo} est l'angle critique de réflexion pour la raie MoKα (1,70 mrad). Considérant une taille de barreau d_{track} de 36 µm et une distance de travail and WD = 1 mm, une valeur de x = 89 µm est attendue, en bon accord avec les mesures.

Durant l'excursion du capillaire, le signal de MoKα varie et est maximum quand le capillaire est aligné avec le centre d'un barreau de Mo. Φ_{track} peut être déterminé en tant que la distance entre deux maxima successifs dans la fig R.7.

Dans un deuxième temps la même expérience a été réalisée sur le motif de titane mince évaporé sur le substrat de cobalt. Différents rayons de capillaire ont été utilisés : rcap = 50µm, 25µm, 10µm et 5µm. Ces séries d'expériences démontrent que la collection locale de fluorescence-X est possible en laboratoire avec un niveau significatif de signal/bruit, même sur des couches minces.

La résolution latérale de la technique dépend du rayon du capillaire de collecte et de sa distance par rapport à l'échantillon. Un enjeu majeur est l'estimation de la résolution latérale ultime atteignable en utilisant une telle configuration. Pour répondre à cette question, nous avons développé un programme de simulation afin de déterminer le niveau de signal XRF collecté à travers de plus fins capillaires. Le programme, détaillé dans le **Chapitre IV** est dérivé de la méthode des éléments finis et est basé sur les équations des paramètres fondamentaux. Il est paramétré avec les données du banc d'essai (géométrie, caractéristiques du faisceau primaire, collection de fluorescence-X à travers un capillaire cylindrique). Les résultats de la simulation dans le cas d'un échantillon homogène sont en bon accord avec les résultats expérimentaux.

La figure R.9 montre l'influence du rayon du capillaire de collecte sur le niveau de signal. Les triangles verts sont les données expérimentales et les points bleus relié sont les résultats de simulation. Pour de grands rayons de capillaires le signal varie comme $r_{cap}^{1.8}$.

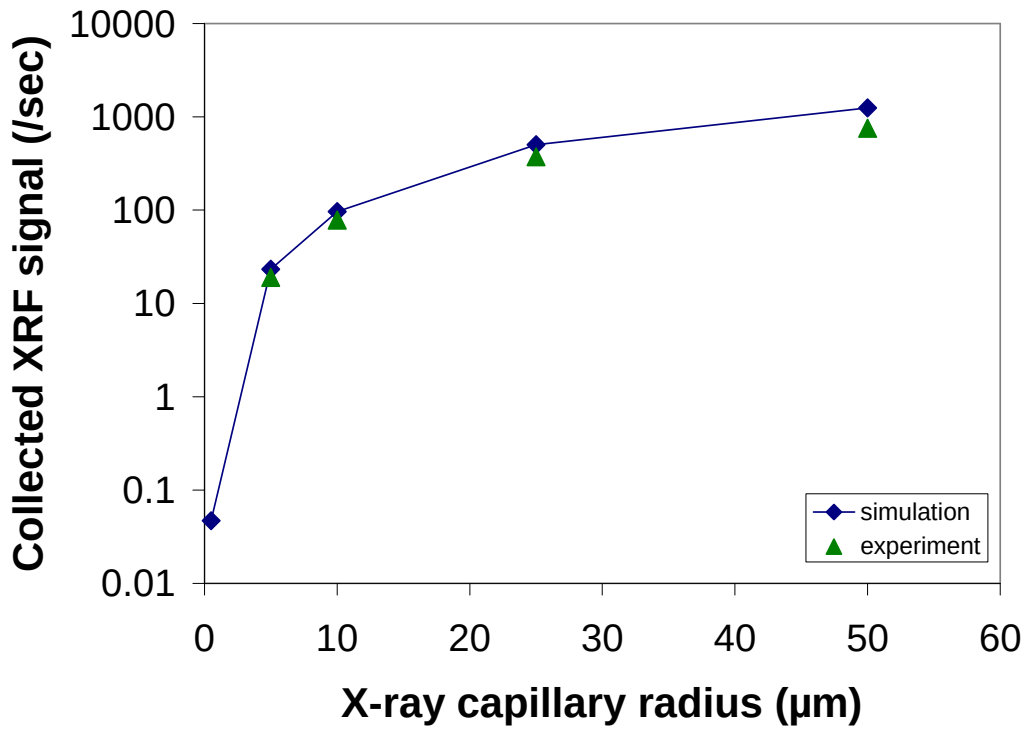

Fig R.9: *Niveau de signal XRF collecté en fonction du rayon du capillaire de collecte. La taille du capillaire est de 50mm et sa distance de travail est de 1mm.*

Nous observons sur ce graph que dans le cas d'un capillaire de rayon 0.5µm, le signal chute rapidement. Le programme de simulation permet de déterminer quelles sont les

paramètres optimaux pour l'utilisation d'un capillaire de rayon 0.5µm à travers l'étude de l'influence de la longueur du capillaire et de la distance de travail sur le niveau de signal.

Ce programme permet d'assurer qu'une résolution latérale de 1µm peut être obtenue en laboratoire avec une source à rayons-X de basse puissance focalisée et avec un détecteur EDX equipé d'un capillaire à rayons-X de rayons intérieur 0.5µm à condition qu'il soit long de 20mm et positionné à une distance de travail inférieure à 27µm.

En utilisant une source plus brillante telle qu'une source de rayons-X à anode tournante ou à jet de métal liquide [24], une hausse significative du signal peut être espérée (jusqu'à un facteur 100). De plus en remplaçant le capillaire cylindrique par un elliptique à l'entrée du détecteur, cela conduirait à un gain supplémentaire d'un facteur 20 sur le niveau de signal [25, 26]. Ainsi une résolution latérale submicronique sur l'analyse de fluorescence-X peut être effectivement possible avec une source d'excitation de laboratoire. Bien entendu, travailler en environnement synchrotron conduirait à un plus haut niveau de signal ce qui permettrait de diminuer encore le rayon du capillaire et une résolution latérale inférieure à 100 nm pourrait probablement être atteinte.

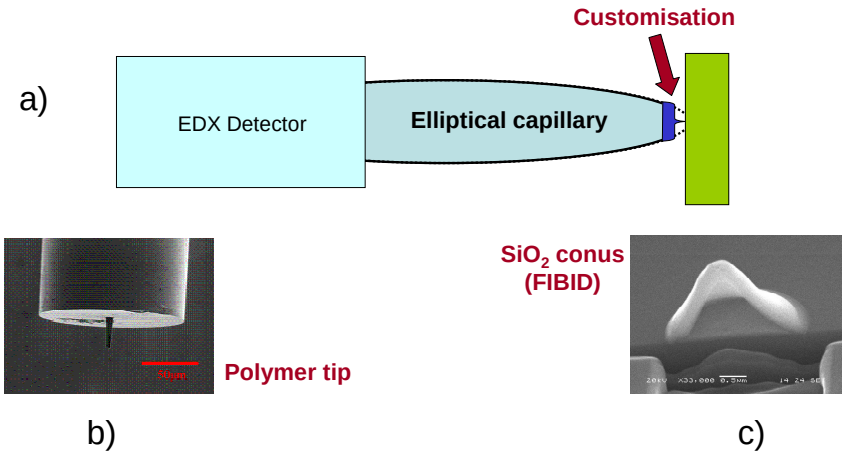

Fig R.10: *(a) La collection de rayons-X est effectuée à travers le capillaire elliptique sur lequel se trouve un apex en polymère utilisé en tant que sonde du Microscope en Champ Proche ; (b) Exemple d'apex en polymère ajouté à une fibre optique photonique (courtoisie de LovaLite SA); (c) Cône de SiO_2 déposé par CVD assistée par Faisceau d'Ion Focalisé (Focus Ion Beam (FIB)) (courtoisie de H. Dallaporta, CINaM).*

Ce travail ouvre la voie du couplage entre l'analyse XRF et la Microscopie à Force de Cisaillement. L'idée est de remplacer la fibre optique effilée de notre tête Shear force (force de cisaillement) fabriquée au laboratoire par un capillaire à rayons-X. Cependant, dans ce cas, il devrait être approché jusqu'en en interaction champ proche mécanique avec

l'échantillon. Une distance de travail de 100nm pourrait être atteinte avec l'utilisation d'un apex en polymère à l'extrémité du capillaire. En effet le relevé topographique peut être réalisé par cet apex tandis que les rayons-X pourraient facilement être collectés car le polymère est quasi-transparent aux rayons-X (voir Fig.R.10).

Une autre configuration consisterait en l'utilisation du capillaire pour exciter l'échantillon tandis que la fluorescence X serait collectée en configuration classique. Le capillaire servirait donc à la fois pour illuminer avec le faisceau primaire et pour les mesures SPM (Fig R.11). Le capillaire a besoin d'être fonctionalisé comme expliqué au dessus.

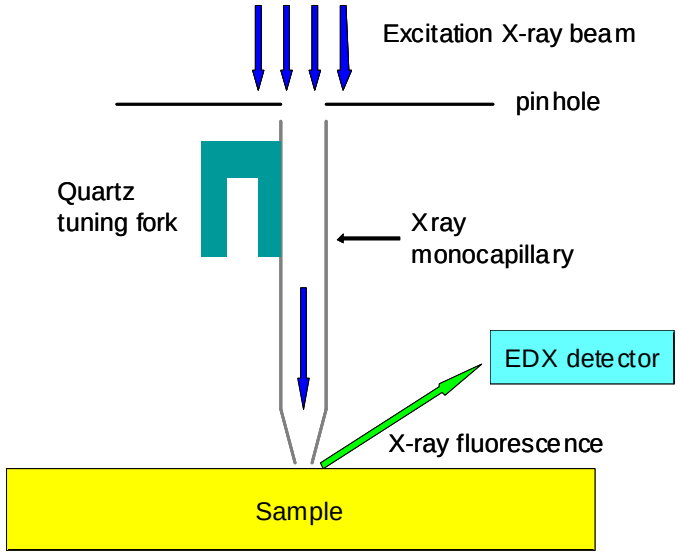

Fig R.11: *Autre configuration possible de l'instrument. Dans ce cas l'échantillon est excité localement à travers le monocapillaire à rayons-X agissant à la fois comme source d'illumination et comme pointe-sonde de SPM. Le signal XRF est collecté en configuration classique. Pour coïncider avec les besoins du Microscope à Force de Cisaillement, l'extrémité du capillaire a besoin d'être fonctionnalisée.*

La géométrie idéale du banc d'essai définie par calculs numérique doit être testée pour définir les conditions expérimentales permettant d'atteindre une résolution latérale de 1µm avec une source de faible puissance microfocalisée. Des expériences peuvent aussi être réalisées sur une ligne de lumière synchrotron pour déterminer la résolution latérale ultime de cette technique. Ainsi la tête de SNOM fabriquée au laboratoire devra être adaptée pour être équipée d'un capillaire elliptique et la résolution ultime pourra ainsi être évaluée. Toutes ces mesures devront être comparées à des résultats de simulation numérique.

Le programme est aussi adapté pour l'analyse d'échantillon composé de plusieurs éléments. Des calculs supplémentaires devront êtres lancés afin de définir la sensibilité de la technique selon les caractéristiques des échantillons (effet de matrice, inclusions, profondeur,…).

Références

[1] International Technology Roadmap for Semiconductors, 2007 Edition, Emerging Research Materials. Available at: http://www.itrs.net/Links/2007ITRS/2007_Chapters/2007_ERM.pdf (last accessed: 18/07/2013)

[2] G. Binning, H. Rohrer, “Scanning Tunneling Microscopy - from birth to adolescence”, reviews of modern physics, 59, 3, part 1, 1987

[3] J.K. Gimzewski, R. Berndt and R.R. Schlittler, “Observation of local photoemission using a scanning tunneling microscope”, ultramicroscopy, 42-44, 366-370, 1992

[4] K. Tsuji, K. Wagatsuma, K. Sugiyama, K. Hiraga and Y. Waseda, “EXAFS- XANES-like spectra obtained by X-ray excited scanning tunneling microscope tip current measurement”, Surf. Interface Anal, 27, 132-135, 1999

[5] T. Okuda, T. Eguchi, K. Akiyama, A. Harasawa, T. Kinoshita, Y. Hasegawa, M. Kawamori, Y. Haruyama and S. Matsui, “Nanoscale chemical imaging by scanning tunneling microscopy assisted by synchrotron radiation”, Phys. Rev. Lett, 102, 105503, 2009

[6] C.-Y. Chiu, Y.-L. Chan, Y.J. Hsu and D.H. Wei, “Collecting photoelectrons with a scanning tunneling microscope nanotip”, Apll. Phys. Lett , 92, 103101, 2008

[7] V.Rose, J.W. Freeland, “Nanoscale chemical imaging using synchrotron x-ray enhanced scanning tunneling microscopy”, AIP. Conf. proc. 1234, p. 445-448, 2009

[8] V. Rose, T.Y. Chien, J. Hiller, D. Rosenmann, R.P. Winarski, “X-ray nanotomography of SiO_2-coated $Pt_{90}Ir_{10}$ tips with sub-micron conductive apex”, Appl. Phys. Lett, 99, 173102, 2011

[9] V.Rose, K.Wang, T.Y. Chien, J. Hiller, D. Rosenmann, J. W. Freeland, C. Preissner and S.-W. Hla, “Synchrotron X-ray scanning tunneling microscopy: fingerprinting near to far field transitions on Cu(111) induced by synchrotron radiation”, Adv. Funct. Mater, 23, 2646, 2013

[10] A. Saito, J. Maruyama, K. Manabe, K. Kitamoto, K. Takahashi, K. Takami, M. Yabashi, Y. Tanaka, D. Miwa, M. Ishii, Y. Takagi, M. Akai-Kasaya, S. Shin, T. Ishikawa, Y. Kuwahara and M. Aono, “Development of a scanning tunneling microscope for in situ experiments with a synchrotron radiation hard-x-ray microbeam”, J. Synchrotron Rad. 13, 216, 2006

[11] I. Schmid, J. Raabe, B. Sarafimov, C. Quitmann, S. Vranjkovic, Y. Pellmont and H.J. Hug, “Coaxial arrangement of a scanning probe and an X-ray microscope as an novel tool for nanoscience”, Ultramicrosc., 110, 1267-1272, 2010

[12] M. Ishii, “Capacitance X-ray absorption fine structure measurement using scanning probe A method for local structure analysis of surface defects”, Physica B 308-310, 1153-1156, 2001

[13] M. Ishii, “Capacitance XAFS method: X-ray absorption spectroscopy of low-dimensional structures”, J. Synchrotron Rad, 8, 331-333, 2001

[14] M. Ishii, N. Rigopoulos, N. Poolton and B. Hamilton, “X-ray absorption microspectroscopy using Kelvin force microscopy with an X-ray source”, Physica B, 376-377, 950-954, 2006

[15] M.S. Rodrigues, T.W. Cornelius, T. Scheler, C. Mocuta, A. Malachias, R. Magalhães, O. Dhez, F. Comin, T. H. Metzger and J. Chevrier, “In situ observation of the elastic deformation of a single epitaxial SiGe crystal by combining atomic force microscopy and micro x-ray diffraction”, J. of Appl. Phys, 106, 103525, 2009

[16] N. Pilet, J. Raabe, S. E. Stevenson, S. Romer, L. Bernard, C. R. McNeill, R. H. Fink, H. J. Hug and C. Quitmann, “Nanostructure characterization by a combined x-ray absorption/scanning force microscopy system, Nanotechnology”, 23, 475708, 2012

[l7] S. Larcheri, “Joint use of x-ray synchrotron radiation microbeams and tip-assisted photon detection for nano-scale XAFS spectroscopy and chemically sensitive surface mapping”, Università Degli Studi di Trento, Italia, 2007, thesis

[18] F. Jandard, C. Fauquet, M. Dehlinger, A. Ranguis, A. Bjeoumikhov, S. Ferrero, D. Pailharey, B. Dahmani and D. Tonneau, “Mapping of X-ray induced luminescence using a SNOM probe”, Applied Surface Science 267, 81-85, 2013

[19] J.C. Lee, D.H. Park, “Self-defects properties of ZnS with sintering temperature”, Mater. Lett. 57, 2872–2878, 2003

[20] X.L. Wu, G.G. Siu, C.L. Fu, H.C. Ong, “Photoluminescence and cathodoluminescence studies of stoichiometric and oxygen-deficient ZnO films”, Appl. Phys. Lett. 78, 2285–2287, 2001

[21] K. Vanheusden, W.L. Warren, C.H. Seager, D.R. Tallant, J.A. Voigt, B.E. Gnade, “Mechanisms behind green photoluminescence in ZnO phosphor powders”, J.
Appl. Phys. 79, 7983–7989, 1996

[22] U. Ozgür, Ya.I. Alivov, C. Liu, A. Teke, M.A. Reshchikov, S. Dogan, V. Avrutin, S.-J. Cho, H. Morkoc, “A comprehensive review of ZnO materials and devices”, J. Appl. Phys. 98, 041301, 2005

[23] M. Dehlinger, C. Dorczynski, C. Fauquet, F. Jandard and D. Tonneau, “Feasibility of simultaneous surface topography and XRF mapping using Shear Force Microscopy”, Int. J. Nanotechnol. Vol 9, Nos. 3-7, 460- 470, 2012

[24] O. Hemberg, M. Otendal and H.M. Hertz, “Liquid-metal-jet anode electron-impact X-ray source”, Appl Phys Lett, 83, 7, 1483, 2003

[25] A. Bjeoumikhov, S. Bjeoumikhova, R. Wedell, “Capillary optics in X-ray Analytics”, Part Part Syst Char, 22, 384–390, 2006

[26] A. Bjeoumikhov, N. Langhoff, S. Bjeoumikhova, R. Wedell, “Capillary optics for micro x-ray fluorescence analysis”, Rev Sci Instrum, 76, 063115-1–063115-7, 2005

Contents

Introduction

Non destructive elemental and chemical analysis at high lateral resolution remains a major challenge for life and physical sciences. For example electronic and glass industries (RRAM, FeRAM, smart materials, solar cells) need sub-100nm resolution characterization tools for material processing, reverse engineering, control and failure analysis [1].

Scanning Probes Microscopes (SPM) are tools of primary importance because they promoted nanoscience, offering for the first time the possibility to perform microscopy up to atomic resolution in the direct space [2]. These equipments allow various in-situ spectroscopies to probe surface local properties (magnetic, electronic states, adhesion…) through the microscope tip. However, it remains not possible to perform the sample chemical mapping without *a priori* knowledge of the sample composition. During the last ten years, numbers of characterization tools were thus developed to obtain with the same apparatus sample imaging and chemical mapping.

The very first idea to combine SPM with a local chemical analysis appeared in the early 90's by Gimzewski [3]. The experiment consisted in photoelectron local collection by a STM tip under UHV conditions while the tip-surface region was illuminated by a quartz-halogen lamp, a very intense illumination source. He got a contrast photoemission map by using the photocurrent as regulation signal highlighting sub-micron scale emitting structures. However, an a priori knowledge of the top surface composition was still required for interpretation.

X-ray spectroscopies are very accurate techniques providing non destructive in-depth or surface chemical information as well as structural characterization. With the development of nanosciences, the general trend for X-ray spectroscopies at synchrotron beamlines is to increase the lateral resolution by decreasing the beam size probe. Due to the low efficiency of the X-ray focusing optics, wide aperture detectors are developed in parallel. Despite high lateral resolution in the range of 30 nm can be achieved in chemical analysis on some advanced synchrotron beamlines, it remains not possible to align the primary beam spot on a peculiar place of the surface. That is the reason why the coupling of X-ray spectroscopies with Scanning Probe Microscopy (SPM) to get simultaneously sample topography and chemical mapping at very high lateral resolution should play a key role in the field of

nanosciences in the near future. The idea is to keep a high brightness X-ray microspot and to locally record the surface signal via the SPM probe at very high lateral resolution.

The earliest experiences in this field were performed in synchrotron environment because of the source high brightness. This is still the way followed by several teams around the world. Indeed, Tsuji et al. [4] measured the Total Electron Yield (TEY) with a STM tip while tuning the primary beam energy through the absorption edges of the sample elements (Ni and Au). They obtained, EXAFS- (Extended X-ray Absorption Fine Structure) and XANES- (X-ray Absorption Near Edge Spectroscopy) like spectra by plotting the tip-sample current as a function of the incident photon energy. Eguchi et al. also performed TEY measurements on Fe and Ni checkboard like pattern [5]. By tuning the X-ray primary beam under and above Ni and Fe absorption edges, the authors were able to obtain specific element images with a lateral resolution of 10nm.

Ching-Yuan Chiu et al. simulated the photoelectron collection via a nanotip under synchrotron illumination [6]. They pointed out that in near-field condition, photoelectron current alone cannot explain the photocurrent magnitude collected by the STM tip. Indeed, a non-negligible part of the whole signal comes from secondary electrons. The different contributions within the total current signal is detailed by V. Rose et al. [7]. The development of smart tips made of PtIr coated by a 500nm-thick insulating SiO_2 layer except at the apex (length smaller than 0.5µm) is also presented [8, 9], as earlier advised by Gimzewski [3].

Saito et al. detected tip current modulation on Ge nano-island on Si(111) while tuning primary X-ray illumination across the Ge absorption K-edge [10]. They were able to identify a Ge nano island by measuring its absorption-edge, to image it and to map the tip-sample current below and after the edge.

Recently, coaxial alignment combination between SPM and STXM (Scanning Transmission X-ray Microscopy) was developed by Schmid et al. [11]. In this experiment, the X-ray beam is focused on a semi-transparent sample. The transmitted beam is usually collected by a photodiode. However, the authors replaced the photodiode by a smart AFM tip, specially designed to collect photoelectrons. The lateral resolution of this technique is limited by the size of the primary illumination and authors claimed that a 20nm spatial resolution can be achieved.

Ishii et al. proposed a method using a Scanning Capacitance Microscope under tuneable synchrotron radiation [12]. X-ray irradiation leads to the photoionization of the surface defects that release the trapped free carriers. The tip-sample capacitance value is sensitive to this modification. By measuring the tip apex-sample surface capacitance

variation, the authors could perform a defect map of the free electron traps at a semiconductor near surface [13]. Finally the photon energy dependence of the capacitance provides site-selective XAFS spectra on the defects [12]. Ishii and Hamilton et al. designed also a Kelvin Force Microscope combined with an X-ray source (X-KFM) to investigate the electronic states of the electron-trapping centres [14]. They are able to perform simultaneous conventional AFM topography mapping and local X-KFM measurements in order to localize the trapping centres. The apparatus is also able to perform XAS-like spectra at a given tip position by plotting the Kelvin force as a function of the incident energy.

Local observation of nanostructures elastic properties was performed by Chevrier et al. by combination of an Atomic force Microscope (AFM) with micro X-ray diffraction [15]. X-ray diffraction patterns are recorded by a two-dimensional array detector while the AFM tip applies a pressure on a single micrometer size crystal. This work was performed using an X-ray microsource. It allowed to measure the crystal elasticity modulus.

Pilet et al. focused on several conventional AFM operating modes such as non-contact, intermittent contact, Magnetic Force Microscopy (MFM) or Kelvin Force Microscopy (KFM) as well as STXM measurements. [16]. By this way, they could characterize different kind of samples: polymer blends, Cr/Ti model nanostructure fabricated by lithography and magnetic multilayers.

In this context, the ‘Centre Interdisciplinaire de Nanosciences de Marseille’ also developed a home-made SNOM-SFM head (Scanning Near-field Optical Microscope – Shear-Force Microscope) tested first in local XAS-XEOL acquisition (X-ray Absorption Spectroscopy-X-ray Excited Optical Luminescence) at ESRF during a first European project (‘X-Tip’, Strep program # NMP4-CT-2003-505634). A major challenge was obtain an on-table apparatus equipped with a laboratory source and offering a significant signal/noise ratio. This study was supported by a second European project (‘LUMIX’, Eureka # E4383). It is noticeable that the luminescence collected has no correlation with the SFM feedback loop signal used for tip to sample distance control. This avoids artefacts in recorded images due to tip-sample distance variation during X-ray illumination.

In this thesis, all chapters are deliberately self consistent**.** That is the reason why some parts are repeated.

Chapter I presents the principle of the experimental techniques used. Near-field microscopy and in particular Shear-Force Microscopy (SFM) are described. X-ray spectroscopy physical background is also presented in particular XRF and XAS-XEOL spectroscopy. X-ray capillary optics, monocapillary or polycapillary lenses, are described.

Mapping of local X-ray induced visible luminescence using a SNOM probe is reported in **Chapter II**. The main results obtained by Larcheri at al. in a preceding thesis [17] with the instrument in ESRF-Grenoble are first summarized. Then the equipment was tested in lab using a He-Cd laser. The key issue was to obtain enough signal to noise ratio with a low power laboratory source micro-focused using a polycapillary lens. This is reported in the second part of Chapter II.

However, luminescence is a property limiting studies to mainly semiconducting materials. X-ray fluorescence signal (XRF) can be used to characterize a wider range of elements, limited by the primary beam maximum energy and by the element detectability. Thereby, by replacing the sharp optical fibre of the SNOM head by a cylindrical X-ray capillary, it should be possible to perform local XRF analysis. **Chapter III** investigates the feasibility demonstration of this technique. A test-bed carrying out this concept was developed and used to estimate the ultimate resolution that could be obtained. X-ray capillaries are usually used as X-ray focusing optics. The originality of this work lies in their use for photon collection. Indeed, this offers the possibility to artificially approach the EDX detector, avoiding the steric hindrance of the primary beam.

Simulations by the finite element method allowed to calculate the variations of the collected signal as a function of XRF microscopy test-bed geometry: capillary inner radius, capillary length and working distance. The model used is detailed in **Chapter IV**. The results are presented and compared to the ideal model of a point-source emitter.

Discussion about signal/noise ratio and lateral resolution of local XRF mapping through cylindrical capillaries is given. From this work, it appears that using elliptical capillaries for detection and approaching toward the sample in mechanical near-field interaction is a promising way to perform local XRF spectroscopy.

References

[1] International Technology Roadmap for Semiconductors, 2007 Edition, Emerging Research Materials. Available at: http://www.itrs.net/Links/2007ITRS/2007_Chapters/2007_ERM.pdf (last accessed: 18/07/2013)

[2] G. Binning, H. Rohrer, “Scanning Tunneling Microscopy - from birth to adolescence”, reviews of modern physics, 59, 3, part 1, 1987

[3] J.K. Gimzewski, R. Berndt and R.R. Schlittler, “Observation of local photoemission using a scanning tunneling microscope”, ultramicroscopy, 42-44, 366-370, 1992

[4] K. Tsuji, K. Wagatsuma, K. Sugiyama, K. Hiraga and Y. Waseda, “EXAFS- XANES-like spectra obtained by X-ray excited scanning tunneling microscope tip current measurement”, Surf. Interface Anal, 27, 132-135, 1999

[5] T. Okuda, T. Eguchi, K. Akiyama, A. Harasawa, T. Kinoshita, Y. Hasegawa, M. Kawamori, Y. Haruyama and S. Matsui, “Nanoscale chemical imaging by scanning tunneling microscopy assisted by synchrotron radiation”, Phys. Rev. Lett, 102, 105503, 2009

[6] C.-Y. Chiu, Y.-L. Chan, Y.J. Hsu and D.H. Wei, “Collecting photoelectrons with a scanning tunneling microscope nanotip”, Apll. Phys. Lett , 92, 103101, 2008

[7] V.Rose, J.W. Freeland, “Nanoscale chemical imaging using synchrotron x-ray enhanced scanning tunneling microscopy”, AIP. Conf. proc. 1234, p. 445-448, 2009

[8] V. Rose, T.Y. Chien, J. Hiller, D. Rosenmann, R.P. Winarski, “X-ray nanotomography of SiO_2-coated $Pt_{90}Ir_{10}$ tips with sub-micron conductive apex”, Appl. Phys. Lett, 99, 173102, 2011

[9] V.Rose, K.Wang, T.Y. Chien, J. Hiller, D. Rosenmann, J. W. Freeland, C. Preissner and S.-W. Hla, “Synchrotron X-ray scanning tunneling microscopy: fingerprinting near to far field transitions on Cu(111) induced by synchrotron radiation”, Adv. Funct. Mater, 23, 2646, 2013

[10] A. Saito, J. Maruyama, K. Manabe, K. Kitamoto, K. Takahashi, K. Takami, M. Yabashi, Y. Tanaka, D. Miwa, M. Ishii, Y. Takagi, M. Akai-Kasaya, S. Shin, T. Ishikawa, Y. Kuwahara and M. Aono, “Development of a scanning tunneling microscope for in situ experiments with a synchrotron radiation hard-x-ray microbeam”, J. Synchrotron Rad. 13, 216, 2006

[11] I. Schmid, J. Raabe, B. Sarafimov, C. Quitmann, S. Vranjkovic, Y. Pellmont and H.J. Hug, “Coaxial arrangement of a scanning probe and an X-ray microscope as an novel tool for nanoscience”, Ultramicrosc., 110, 1267-1272, 2010

[12] M. Ishii, “Capacitance X-ray absorption fine structure measurement using scanning probe A method for local structure analysis of surface defects”, Physica B 308-310, 1153-1156, 2001

[13] M. Ishii, “Capacitance XAFS method: X-ray absorption spectroscopy of low-dimensional structures”, J. Synchrotron Rad, 8, 331-333, 2001

[14] M. Ishii, N. Rigopoulos, N. Poolton and B. Hamilton, “X-ray absorption microspectroscopy using Kelvin force microscopy with an X-ray source”, Physica B, 376-377, 950-954, 2006

[15] M.S. Rodrigues, T.W. Cornelius, T. Scheler, C. Mocuta, A. Malachias, R. Magalhães, O. Dhez, F. Comin, T. H. Metzger and J. Chevrier, “In situ observation of the elastic deformation of a single epitaxial SiGe crystal by combining atomic force microscopy and micro x-ray diffraction”, J. of Appl. Phys, 106, 103525, 2009

[16] N. Pilet, J. Raabe, S. E. Stevenson, S. Romer, L. Bernard, C. R. McNeill, R. H. Fink, H. J. Hug and C. Quitmann, “Nanostructure characterization by a combined x-ray absorption/scanning force microscopy system, Nanotechnology”, 23, 475708, 2012

[17] S. Larcheri, “Joint use of x-ray synchrotron radiation microbeams and tip-assisted photon detection for nano-scale XAFS spectroscopy and chemically sensitive surface mapping”, Università Degli Studi di Trento, Italia, 2007, thesis

CHAPTER I: Experimental techniques

Near Field Microscopes are powerful tools for surface topography analysis up to atomic lateral resolution. These equipments allow various in-situ spectroscopies, to probe surface local magnetic properties [1], electronic states [2] or even to identify and localize specific chemical group on very small features [3]. However, a-priori elemental analysis is not possible. On the other hand, X-ray spectroscopies are fine analysis techniques providing chemical and structural properties of a material, based on the spectroscopy of photons or of photoelectrons emitted by the sample under X-ray illumination. They require a high brightness excitation X-ray source, usually a synchrotron beam, to irradiate the sample. However, it is not possible to image simultaneously the sample surface neither to position the X-ray primary beam on a peculiar micro or nano-object for further individual analysis. We have thus chosen to combine both techniques in a unique instrument to acquire simultaneously the sample topography and the chemical mapping at high resolution. In the first section, I will present the principles of scanning probe microscopy, while section II describes the X-ray spectroscopy techniques used in this work. Considerations about X-ray sources are given in section III and X-ray capillary optics are presented in section IV.

I.1: Scanning Probe Microscopy

Scanning Probe Microscopy includes various instruments working on the same concept of a sharp tip positioned in near field interaction with a surface at nanometric distances. This small tip-sample gap is maintained constant thanks to a feedback loop that keeps the tip-sample interaction at a setpoint value fixed by the user, while the tip scans the surface in raster scan mode (Fig I.1).

The microscope tip is fixed to piezoscanner motion stages allowing its displacement in X, Y, Z directions above the sample surface by applying V_x, V_y and V_z bias on each piezoscanner.

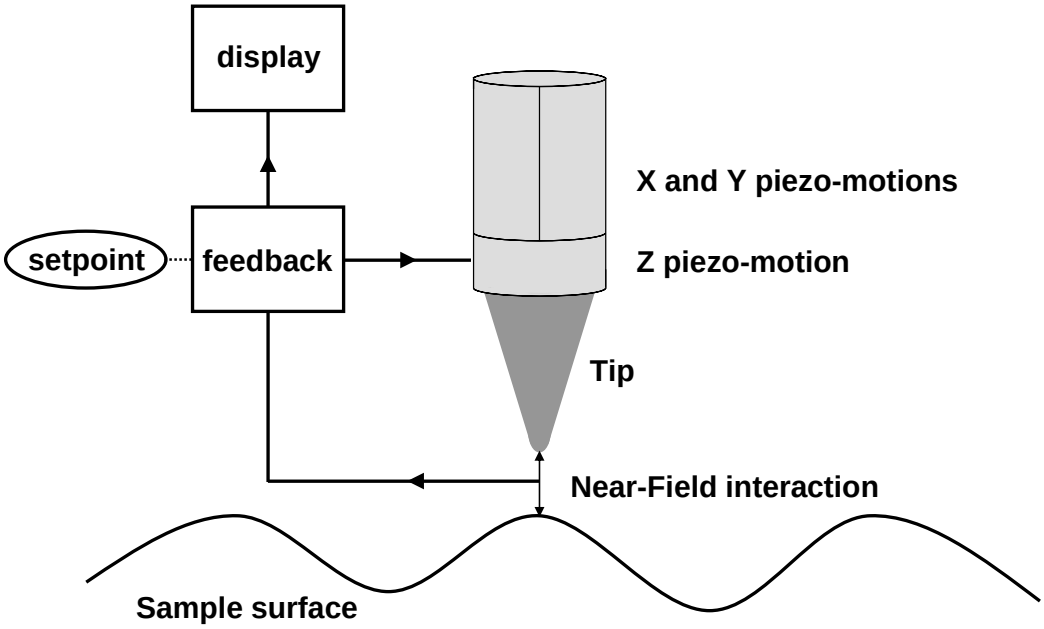

Fig.I.1: *Scanning Probe Microscope principle. A sharp tip fixed on piezoscanner motions is approached in near field interaction with the sample surface. A feedback loop acts on the Z piezo-motion in order to keep the Near-Field interaction constant at a setpoint value as the tip is raster scanned over the sample.*

For each XY position of the surface, the V_z voltage needed to maintain the tip-sample interaction constant is stored in a 2D-matrix. The knowledge of the Z-piezo calibration allows to calculate the sample topography.

The tip shape and sharpness is a key point limiting the lateral resolution of these techniques. Each Near-field microscope is based on a specific probe-sample interaction.

Among the various near-field techniques, I will focus on the most important ones, i.e. STM (Scanning Tunneling Microscopy), AFM (Atomic Force Microscopy). Because SNOM (Scanning Near-Field Optical Microscope) is used in this study, I will also present this technique.

I.1.1: STM

In the 1980s Gerd Binnig and Heinrich Rohrer designed the first Near-Field Microscope, a Scanning Tunneling Microscope (STM) at IBM Zurich [4]. In this case, the tip-sample interaction is the tunnelling current flowing between a metallic tip and a conducting

surface, when the surface is biased. Indeed, at tip-sample distance of few Ångströms the electron wavefunction has a non zero probability to be transmitted through the potential barrier induced by the tip to sample separation, even if the electron energy is lower than the barrier height (Fig.I.2a). When the sample is biased and the tip positioned above the sample, the tunnelling current decreases exponentially with the probe-sample distance. For example the tunnel current increases by a factor of 10 if the tip-sample distance is only 2 Å smaller. This high sensitivity leads to a very high vertical dynamic, that allows to probe the surface at high vertical and lateral resolution (FigI.2b)). This powerful technique enables sample local DOS (Density of States) probing by switching the sign of the sample bias: the sample empty states (respectively filled states) are probed when the sample is biased positively (respectively negatively) regarding to the tip (see Fig.I.3a) (respectively Fig.I.3b)). Because both the tip and the sample must be conducting, the technique is usually run under ultra-high vacuum conditions to prevent tip and sample contamination and oxidation [5; 6].

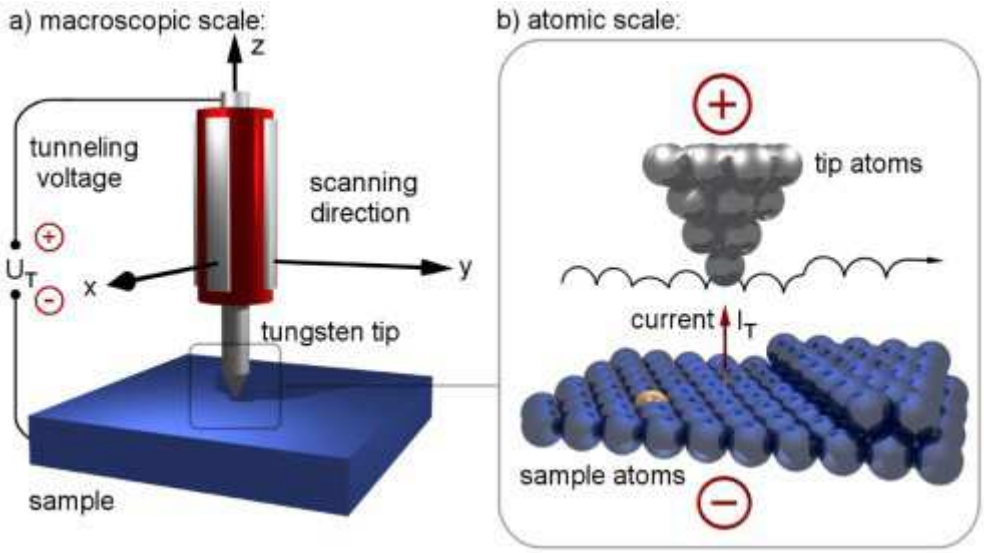

Fig I.2: *Scheme of the Scanning Tunneling Microscope* (*STM) scheme principle. a) microscope overview at macroscopic scale, b) atomic scale* [7]

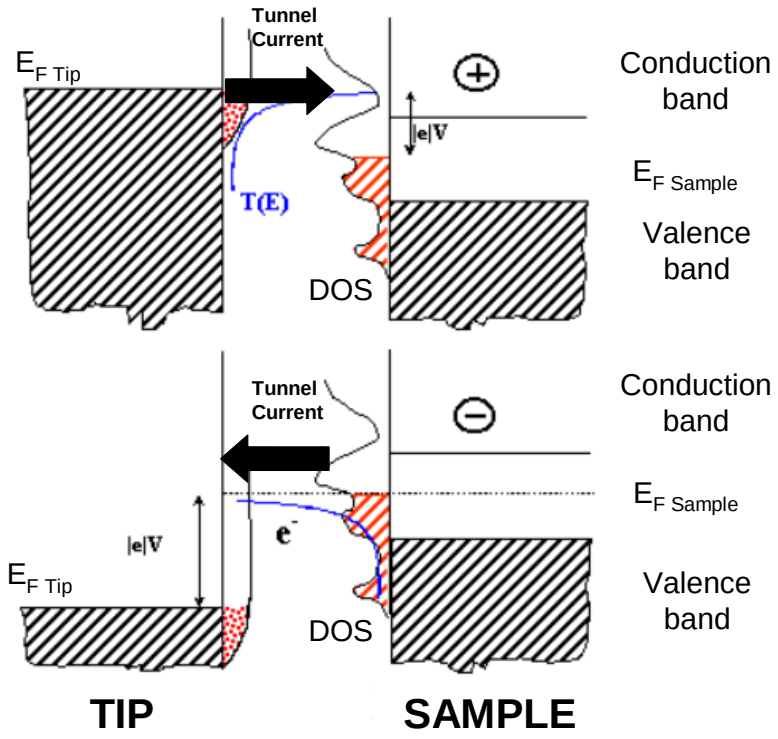

Fig I.3: *DOS probing by STM on a n-type Si [111] surface.a) Vsample>0 (empty states) b) Vsample<0 (filled states)* [from 8]

I.1.2: AFM

The use of STM is dedicated only to the study of conducting or semi conducting samples. That is the reason why in 1985, Gerd Binnig, Christoph Gerber and Calvin Quate developed the first Atomic Force Microscope (AFM) [9] based on the control of another tip-sample interaction: the repulsive or attractive forces at short distances.

The regulation of this instrument is based on the attractive/repulsive forces existing between the probe-tip and the sample, mainly the Van der Waals forces. The AFM tip is situated at the end of a low spring constant (in the range of 0.1 N/m) cantilever which bends up or down under the forces action. A laser beam is reflected on the top of the cantilever towards a 4-quadrant photodiode to measure its vertical deflection (see Fig. I.4).

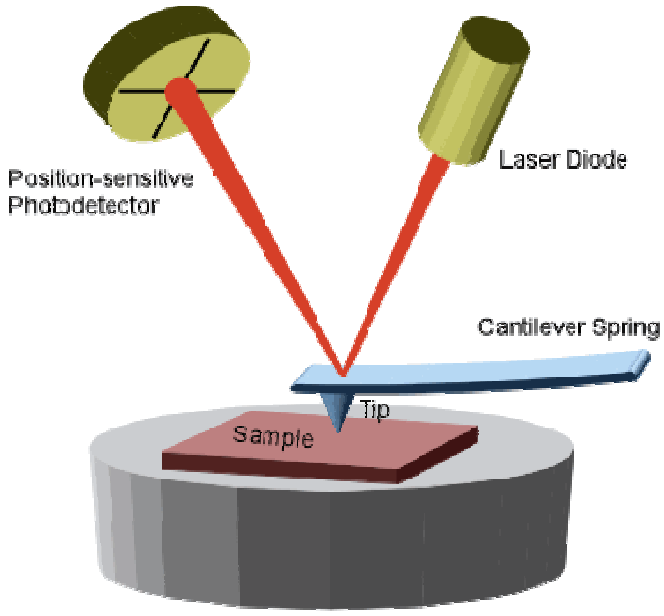

Fig I.4: *Scheme of the Atomic Force Microscope (AFM) principle* [10].

The vertical spot position is maintained at a constant setpoint value by the feedback loop during sample scanning by the AFM tip. A tip-sample iso-interaction mapping can be obtained by recording the (XYZ) values of the piezo ceramic voltages. The advantage of the technique is that AFM allows the study of all kinds of samples, including insulators. The atomic resolution with an AFM was reached for the first time in 1987 [11].

Many AFM modes exist. In contact mode the tip-sample interaction is based on sample-tip repulsive forces. The cantilever deflection is kept in the linear regime during scanning. Otherwise, in the non-contact and semicontact mode the cantilever oscillates at its natural frequency during scanning. In the first case, the tip is never in contact with the surface, while in the second case, the tip is in intermittent contact with the sample surface during cantilever vibration.

Other tip-sample forces can be detected: magnetic, electric etc….depending on the sample physical property to be studied. The AFM tip must be customized taking into account the tip-sample interaction to control. If the scan direction is perpendicular to the longitudinal axis of the cantilever (lateral direction) the friction force causes cantilever twisting. This leads to an horizontal displacement of the laser reflection on the photodiodes. This measure leads to the friction forces distribution throughout the sample surface.

I.1.3: SNOM

The SNOM (Scanning Near Field Optical Microscope) came out from Synge idea that the optical diffraction limit could be overcome if a small hole of diameter $a<<\lambda$ in a metal screen would be used to image a surface at distances $d < a$. The instrument is based on an AFM or on an AFM-type microscope variety called shear-force microscope (SFM) [12].

I.1.3.1: The shear force microscope

In this case, the tip is fixed to a quartz tuning fork excited at its natural frequency in the range of 30 kHz. This excitation induces tip vibration in a plane perpendicular to the sample surface (see figure I.4). The tip extremity oscillation magnitude is in the 10 nm range. Approaching the sample surface to the tip in near-field interaction leads to a frequency shift and to a vibration amplitude variation because of the presence of the additional shear forces between the tip and the surface. Either the amplitude value or the vibration frequency is maintained at a constant value (setpoint) at each XY point of the surface. The feedback system acts on the Z motion of the tuning fork holder in order to maintain this value at the setpoint value.

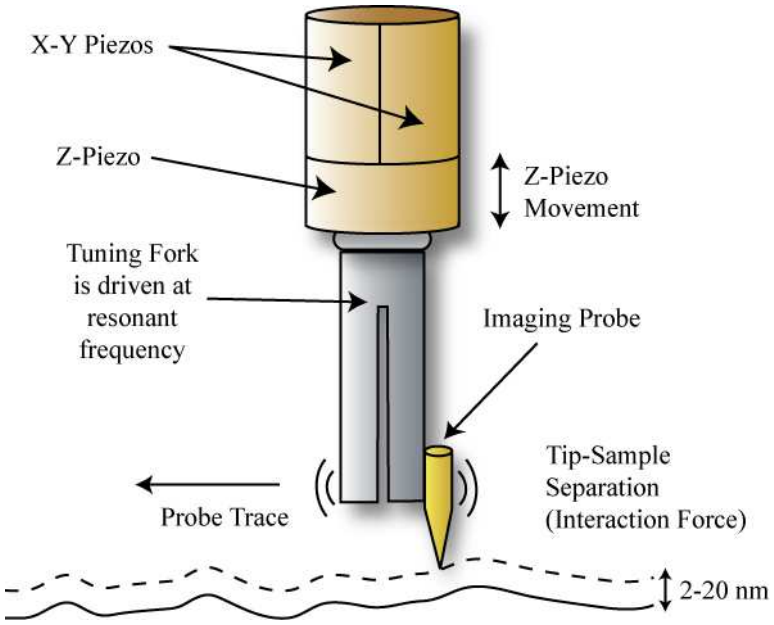

Fig I.4: *Conceptual drawing of the tuning fork Shear-Force Microscope (SFM).* [13]

I.1.3.2: The Scanning Near-Field Optical microscope

The Scanning Near-Field Optical microscope is usually a shear-force based microscope working with a sharp optical fibre stuck on a quartz tuning fork and used as near-field probe [14-17]. The extremity of the fibre is usually coated by a metallic layer, letting a low aperture diameter at the level of its apex. This ensures better collection of the light by the fibre. The regulation of the tip-sample distance is ensured by the shear-force microscope. Three main configurations exist: transmission, reflection and luminescence modes. The sample can be illuminated in near UV-Visible or Near IR region through the sharp optical fibre.

Local sample emission occurs in 4π directions. In the transmission mode, light is collected by a photomultiplier (PMT) through the sample (Fig.I.5). The reflection is dedicated to non transparent samples. The light scattered by the sample is reflected toward the PMT (Fig.I.6). Sample luminescence can also be collected (Fig.I.7). In this case, both previous configurations can be used. In this case light collected is sent to a spectrophotometer or to a PMT equipped with a notch filter [18].

The resolution of the instrument is limited by the fibre aperture, since the working distance is well below the diffraction limit. For example, the minimum aperture of pulled metalized optical fibre found on the market is about 20nm. The signal level is proportional to the incident excitation source power. It must be limited due to thermal damage of both probe and sample.

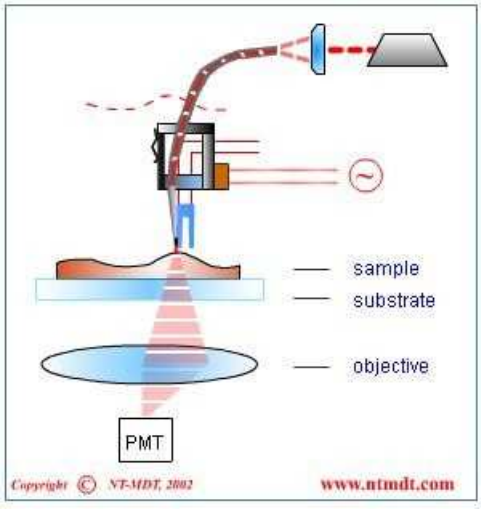

Figure I.5 : *SNOM : Transmission mode* [19]. *(Courtesy Nt-Mdt^{TM}).*

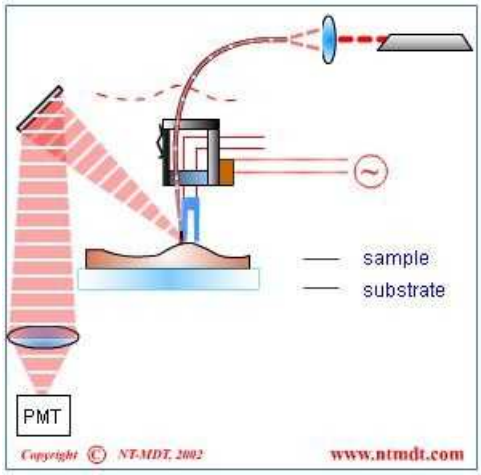

Figure I.6: *SNOM Reflection mode* [19].

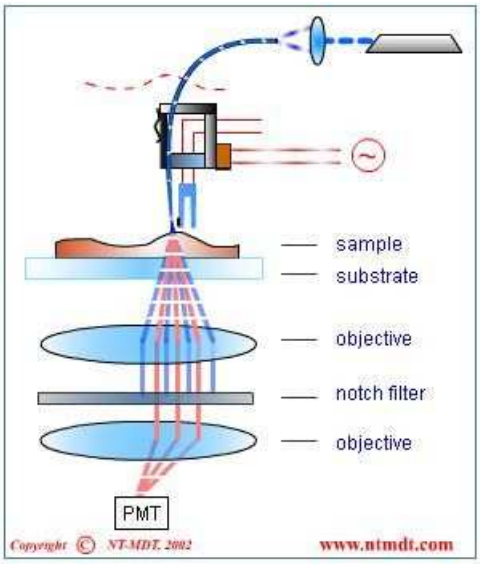

Figure I.7 : SNOM Luminescence mode [19].

To go beyond this limit, the apertureless SNOM concept was proposed where the tip acts as an electromagnetic antenna to enhance the collected signal. Light is focused at the level of the apex of a STM or AFM tip, leading to the presence of a strong electromagnetic field within the narrow tip-sample gap. The amplification is due to the confinement of the field between the sample and the tip, which can be further magnified by the excitation of plasmon or by photon resonance occurring at a wavelength, specific to the tip-sample twin system. This leads to a nanometre-scale resolution of the technique [20-22].

I.2: Interaction of X-rays with matter

X-ray spectroscopies are very powerful techniques allowing elemental and structural characterization of samples at atomic scale. This is due to the small wavelength of the X-ray photons, between about 0.01 nm to about 10 nm, so that photons interact closely with the atoms and their neighbours. They are also sensitive to the density of material. Those techniques are thus of primary choice for material characterization in nanoscience.

X-rays penetrates deeply and interacts with matter, depending on their energy and on the irradiated material. Their absorption in matter follows the Beer-Lambert law:

$$I = I_0 \exp^{-\mu_l x} \qquad \text{Eq (I.1)}$$

Where I_0 and I are respectively the primary beam intensity and the beam intensity after crossing a material thickness *x*. μ_l is the absorption coefficient (in cm^{-1}).

The main interactions of X-rays with matter are:

- Photoelectric effect: this is the main effect for incident photon energies in the range of about 1-100 keV. The incident photon is absorbed by the atom and gives its energy to a core electron, called photoelectron, which is ejected. The final atomic state is a ionized atom with a core-level hole (see figure I.8).

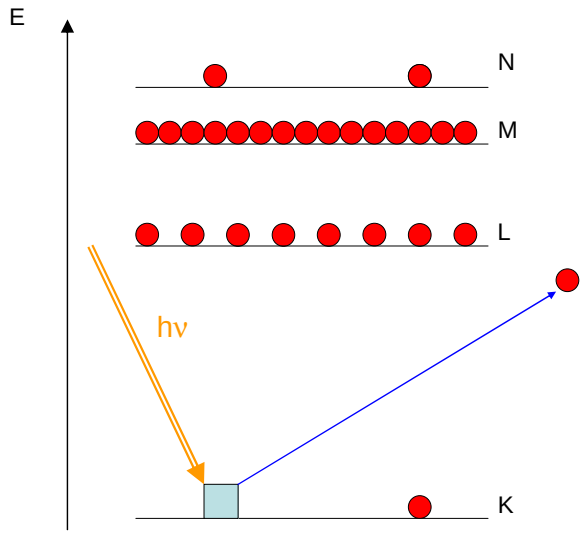

Fig.I.8: *Illustration of the photoelectric effect. An X-ray photon of energy hν is totally absorbed by a K-shell electron that is ejected leaving a core hole.*

The photoelectron energy is determined by the following formula:

$$E_c = h\nu - B \qquad \text{Eq (I.2) [23]}$$

Where E_c is the photoelectron kinetic energy, h is the Planck constant, ν is the frequency of the incident photon and B is the electron binding energy.

- Compton scattering: it consists in the inelastic scattering of the incident photon on an electron of a given atom. The photon gives a part of its energy to an electron that is ejected, and the photon diffuses with a lower energy in a different direction. In the final state the atom is ionised. It occurs for medium energy incident photons, in the range of 100keV-10 MeV.
- Thomson effect: the incident photon is elastically scattered in 2 π directions on an atom without energy loss.

- Pair production: it occurs when a photon interacts with the nucleus of an atom. An electron-positron pair is created providing the incident photon has an energy exceeding twice the rest energy ($m_e c^2$) of an electron (1.022 MeV) It thus occurs at high primary energy.

Fig I.9 shows the predominance of the three main processes (photoelectric effect, Compton effect, pair production) as a function of the incident photon energy and of the atomic number Z absorbing atom.

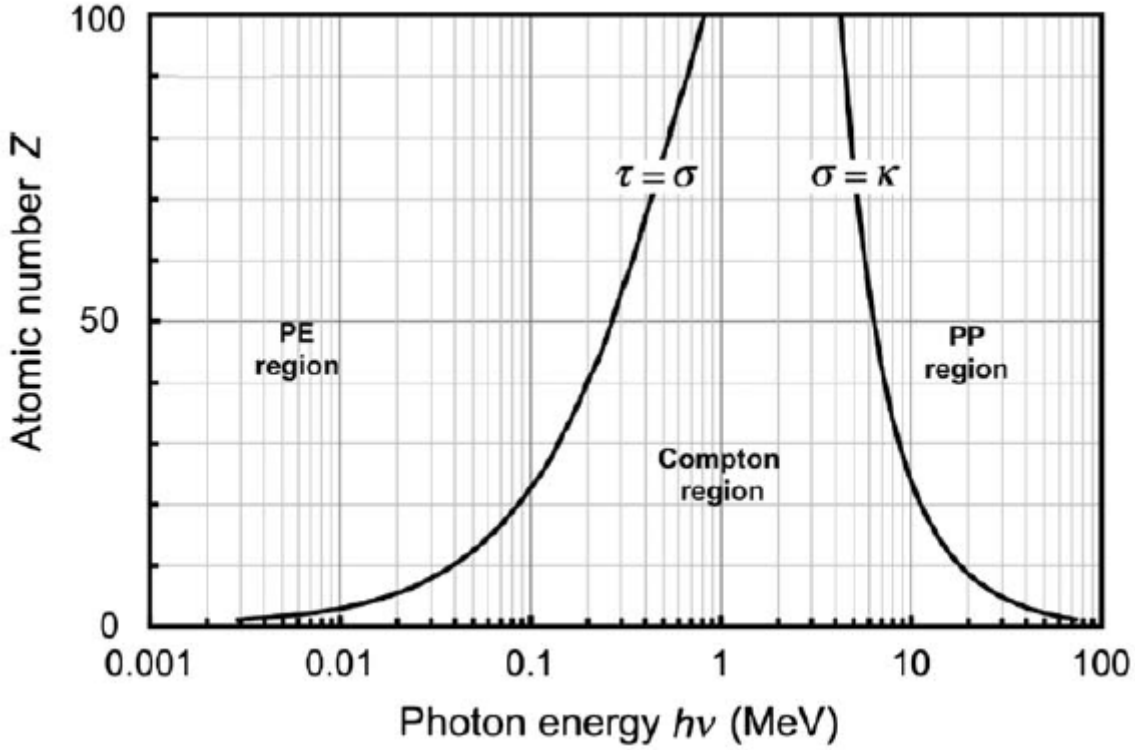

Fig I.9: *Representation of the relative predominance of the three main processes of photon interaction with absorbing atom and incident photon energy: photoelectric effect Compton effect and pair production. The two curves connect points where photoelectric and Compton cross sections are equal ($\tau = \sigma_C$, left) and where Compton effect and pair production cross sections are equal ($\sigma_C = \kappa$, right).* [24]

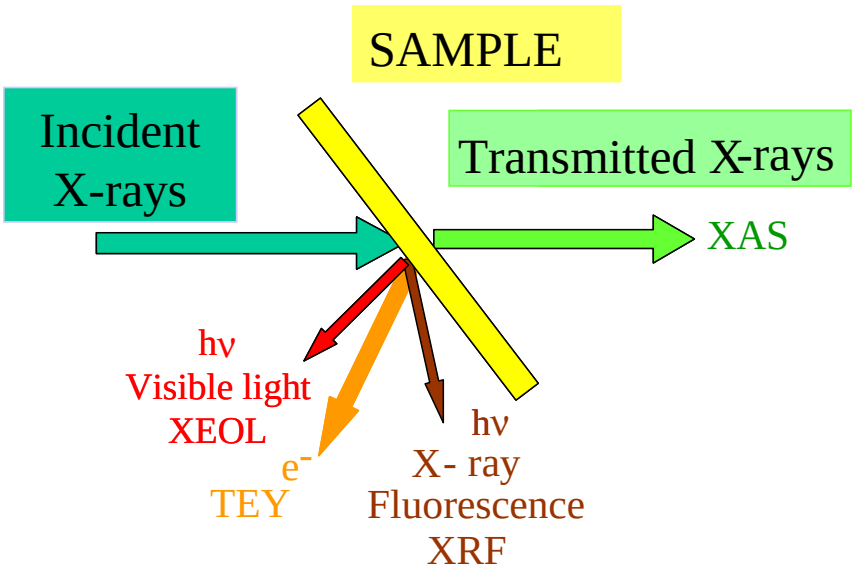

Fig. I.10 : *Scheme of the main particles emitted by a sample under X-ray illumination*

In this work, X-ray photons of less that 35 keV were used so that the particles emitted by the sample are mainly electrons and photons (see Fig.I.10). Because core holes are created in the atom after X-ray absorption in these energy ranges, a rearrangement of the electronic structure of the atom occurs leading to various emission processes including Auger electron emission, X-ray fluorescence, and visible luminescence (XEOL), as will be developed in sections I.2.1 to I.2.4.

I.2.1: X-ray absorption spectroscopy (XAS)

If the sample is thin enough, and the photon flux high enough, there is a significant but attenuated X-ray transmitted beam (see Fig.I.10). The analysis of this beam as a function of X-ray primary energy allows to study X-ray Absorption Spectroscopy (XAS).

The absorption coefficient μ is roughly given by

$$\mu \approx \frac{Z^4}{A.E^3} \qquad \text{Eq (I.3) [25]}$$

where Z and A are the element atomic number and mass number respectively, and E the incident photon energy. The strong dependence of μ with Z involves the atomic selectivity of X-ray absorption, so that good contrast can be achieved in materials' spectroscopy.

The absorption coefficient decreases when the primary beam photon energy increases but this variation is punctuated by sharp jumps (thresholds) that correspond to the photon

energy release toward a core electron, that is ejected (see next section). The absorption edges occur at photon energies corresponding to the core electron binding energy (Fig.I.11). These energies are characteristic of the absorbing elements and are indexed in tables.

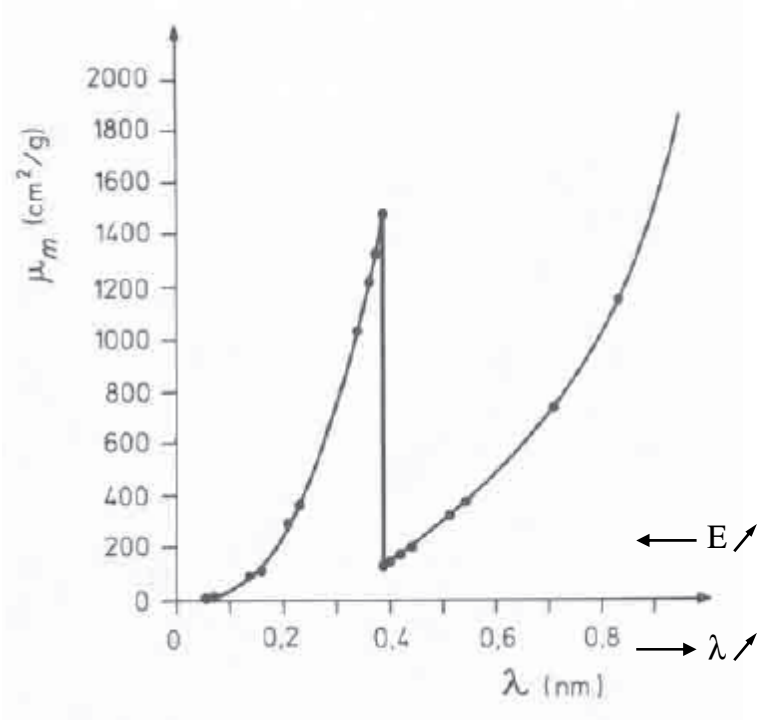

Fig.I.11 : *Absorption edge of Argon (K threshold)* [23]

The absorption coefficient may also be expressed in several extensions such as the mass absorption coefficient ($\mu_m = \mu_l / \rho$ where ρ is the material density). In the case of several elements, we can easily express the resulting absorption coefficient by adding that of every element, each being multiplied by its mass ratio.

In the solid state, if recorded as a function of the incident photon energy, the absorption coefficient exhibits oscillations over 50 to 1000eV after the absorption edge. Fig.I.12 shows a typical spectrum of FeO [23; 26; 27].

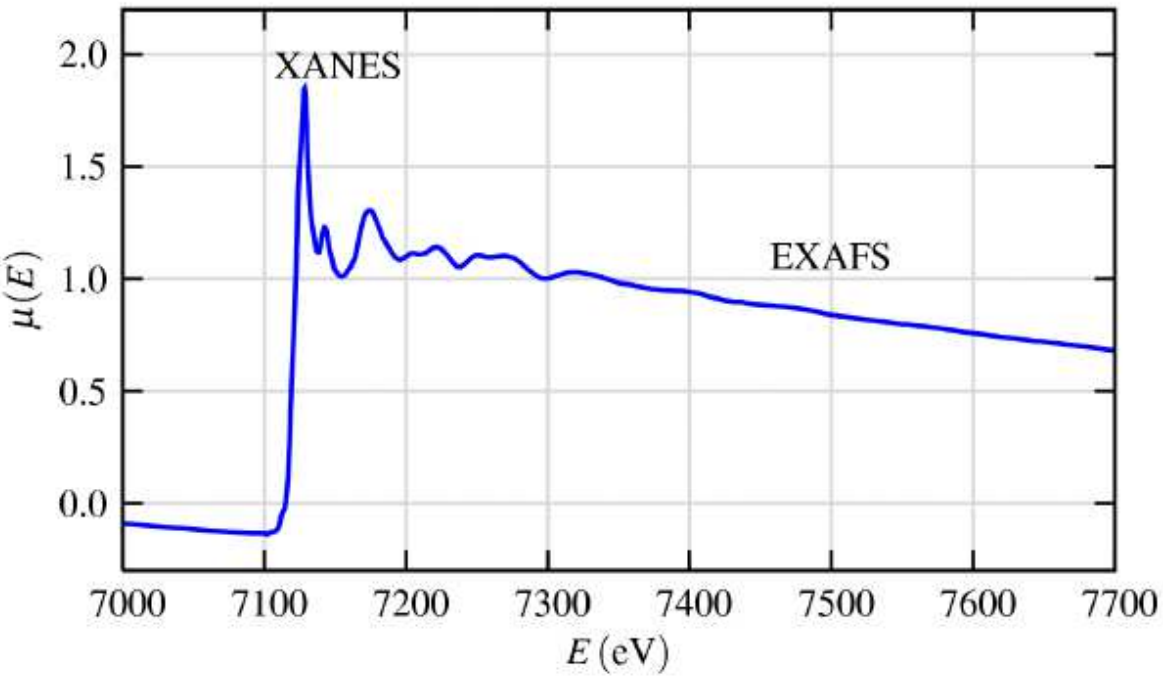

Fig I.12: *XAS spectrum of FeO* [27].

This oscillation phenomenon comes from the photoelectron spherical wave scattering by the neighbouring atoms. Interferences between the scattered and incident wave act on the final state amplitude that modulates the absorption coefficient. This modulation depends on the distance between the emitting and back scattering atom, on their chemical nature and on the photoelectron energy.

The oscillations are thus sensitive to both neighbouring atomic species as well as interatomic distances. Computational simulations from a cluster model representing the absorbing atom and its nearest neighbours have to be performed to fit the spectrum and to identify the structural and chemical properties of the detected element and its chemical environment in the solid. The results are very accurate. The X-ray absorption spectrum is usually interpreted following two separated processes: up to ~50 eV from the edge, the spectroscopy is called XANES (X-ray Absorption Near-Edge Structure), while the remote oscillations are used for Extended X-ray Absorption Fine Structure Spectroscopy (EXAFS) [26], see figure I.12.

I.2.2: Auger effect

In Fig I.13 is illustrated the Auger effect. In this case, an electron from an outer shell (L in Fig I.13) fills the hole left by the photoelectron. The energy in excess is given to a third electron (from N level in Fig I.13) that is ejected, called the Auger electron. The kinetic energy E_c of this electron, called Auger electron, is given by:

$$E_c = E_A - E_B - E_D \qquad \text{Eq (I.4)}$$

where E_A is the energy of the initial core hole shell created by photoelectric effect, E_B is the energy of the second electron shell before it fills the core hole and E_D the energy of the third electron shell before the emission.

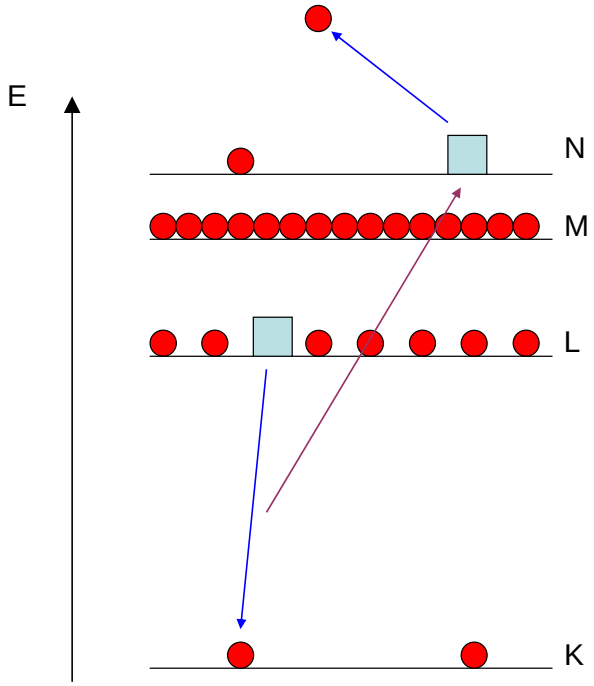

Fig.I.13 : *Illustration of Auger electron emission as a consequence of photoelectric effect*

Auger transitions are indexed with the three levels involved in the excitation-desexcitation process using Siegbahn notation (see next section) and with the Auger electron kinetic energy. For example carbon presents a C KLL transition at 272 eV. This effect competes with X-ray fluorescence. It is more probable for light elements (see figure I.14).

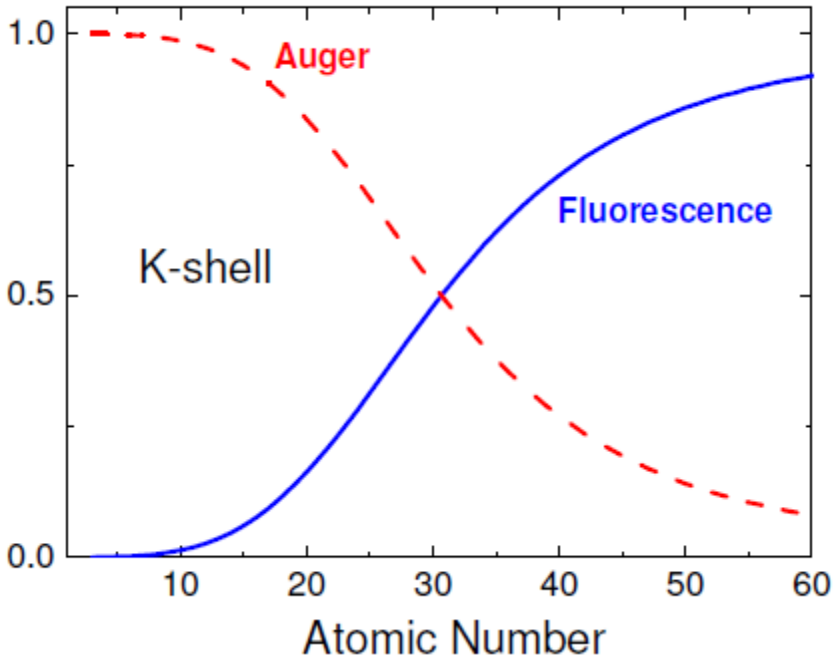

Fig.I.14: *Comparison of Auger yield and fluorescence yield as a function of atomic number* [28].

I.2.3: XRF

I.2.3.1: Primary fluorescence

This effect results from an allowed radiative transition between an electron of an outer shell and the core hole left by the photoelectron (see figure I.15). The energy of the photon released is given by:

$$E_{h\nu} = E_A - E_B$$

where E_A is the energy of the core hole level and E_B is the energy of the outer shell electron. The energy of this released photon is in the range of X-rays.

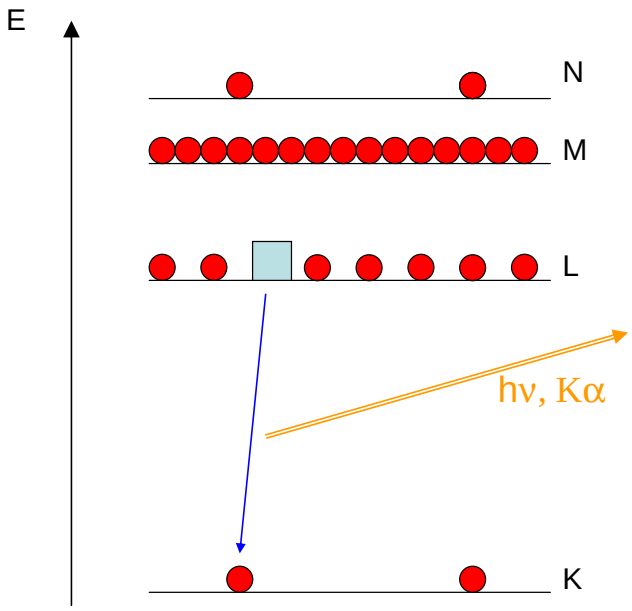

Fig I.15: *Illustration of X-ray fluorescence emission as a consequence of photoelectric effect*

The nomenclature of the emitted X-rays comes from Siegbahn notation. The transition is characteristic of the element and is labelled using the levels involved in the excitation-desexcitation process. The label is composed of a letter that defines the shell that is filled with the outer electron (K, L, M, N, …) and of a greek letter that informs on the electron original level (see Fig I.16) [29-31]. For example when X-ray fluorescence is due to electron fall from an outer level to the first one (n=1), the transition is labelled K. If the origin shell of the electron that fills the core is just above the photoelectron shell, the transition is labelled α. The fluorescence ray schematically presented in Fig I.15 corresponds to the case of Kα transition. A new nomenclature system for X-ray spectroscopy (IUPAC) has been introduced for clarity reasons but Siegbahn notation is still widely used in the scientific community [31].

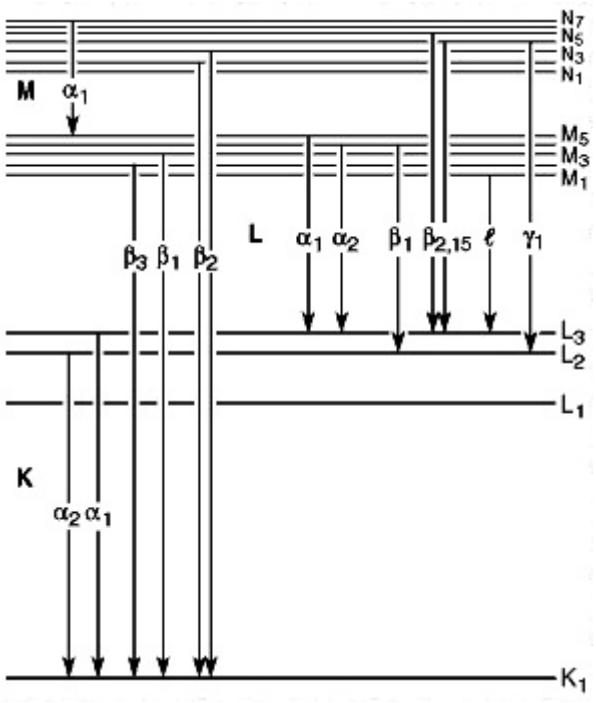

Fig I.16: *Illustration of Siegbahn notation for various emission lines* [29]

These transitions are governed by quantum-mechanical selection rules with various probabilities that result in various emission lines intensity. X-ray fluorescence emission is in competition with Auger effect and is the most probable effect for heavy (high atomic number Z) elements.

X-ray emission lines are characteristic of elements and are tabulated, so that spectroscopy is highly sensitive to the chemical composition of the sample [32].

XRF spectroscopy consists in recording the number of X-ray photons emitted as a function of their energy. A typical example is given in the figure I.17 in the case of a Cobalt sample irradiated by a 35kV Rh Kα X-ray source. In this figure, we can see two peaks that are the two main characteristic lines of Cobalt, the Kα line at 6.9 keV and the Kβ line at 7.6 keV with the expected intensity ratio, coming from the desexcitation probabilities of both lines.

X-Ray Fluorescence is a fast and non destructive technique for determining elemental composition of materials and is widely used in numerous domains, such as materials science [33], cultural patrimony [34], archaeology [35], medical and biology [36], environment [37]…because of its non destructive nature. This technique is still extended through innovative instrumentation developments, quantification, sample preparation methods and application fields [33, 38].

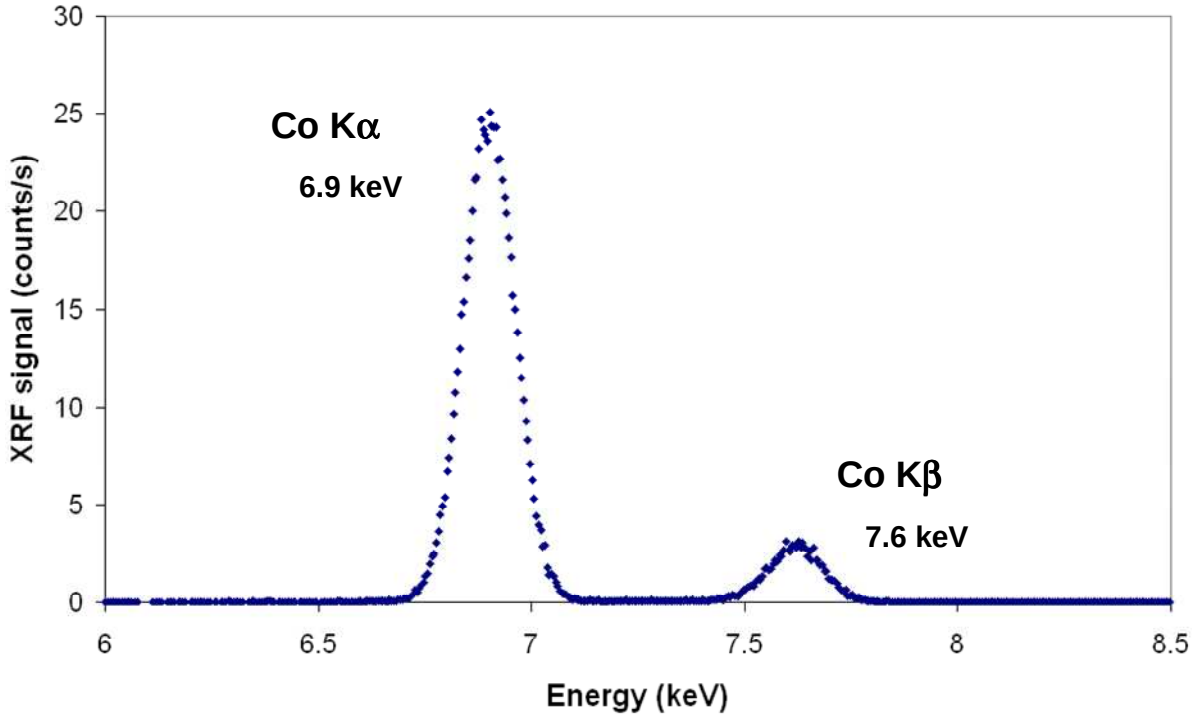

Fig.I.17*: X-ray fluorescence spectrum characteristic of cobalt. Co Kα and Co Kβ are detected at 6.9 keV and 7.6 keV respectively.*

I.2.3.2: Secondary fluorescence

The X-ray fluorescence photon can be reabsorbed while escaping from the sample, leading to secondary excitation and secondary fluorescence emission. This phenomenon occurs only if the fluorescence photon energy is high enough to excite the absorbing atom inner shell. Two kinds of secondary fluorescence phenomena exists: inter-element or self-element. Inter-element fluorescence has the highest yield for elements whose atomic numbers differ of two [39]. Self-element secondary fluorescence is based on the excitation of different groups of X-ray lines belonging to the same element (for example K- to L-lines, L- to M-lines,…). It is highly probable for light elements. Secondary fluorescence can also originate from secondary excitation by photo- and Auger-electrons, from primary beam or X-ray fluorescence scattering [40, 41]. Secondary fluorescence can consequently be non negligible according to the sample composition and the primary beam energy. For example, secondary fluorescence can contribute up to about 20-25% of the fluorescence intensity on a pure sample [40]. For example, in the case of a Fe-Cr sample, 55% of the Cr fluorescence intensity comes from secondary fluorescence [42, 43].

I.2.3.3: Matrix effect

In XRF element quantitative analysis, the fluorescence intensity of a given atom is not directly proportional to its concentration in the sample. Other elements accompanying have an influence on the signal. This is called 'the matrix effect'.

This phenomenon is due to the multi-element effect on the primary beam intensity through matter and to the X-ray fluorescence reabsorption or XRF signal enhancement induced by secondary and tertiary fluorescence. Macroscopic effects can also be taken into account such as inhomogeneities in the sample, pressed or loose powders… [39].

Corrections are therefore essential to determine the concentration of an element in a multi-element sample. It is nowadays widely performed by fundamental parameter method or through calibration curves [44, 45].

I.2.4: XAS-XEOL

After photoelectron ejection from the atom, all electrons of the atom will take part to the electronic rearrangement. During this process, electrons can be transferred to the conduction band. If these electrons recombine with a hole present in the valence band, a radiative recombination of the electron-hole pair can take place if the transition is allowed by quantum mechanics. The luminescence produced is in the visible domain if the sample is semiconducting. Defect centres can also be promoters of luminescence if the defect levels are positioned within the solid band gap. Impurities in the material, holes or doping create inter-band levels and modify the gap inter-level desexcitation path [46]. Photoluminescence is usually studied under laser irradiation because the high photon density delivered by the laser leads to a high signal/noise ratio.

If tuneable X-rays delivered by a synchrotron source are used for excitation, the spectroscopic study of this visible luminescence as a function of the X-ray primary beam is called XEOL (X-ray Excited Optical Luminescence). The spectra are often highly correlated with XAS from where it takes its origin (see fig.I.18 for XAS-XEOL spectra examples) [26, 47]. Indeed, the synchrotron source allows delivery of photons whose energy corresponds to the absorption edge of a given element contained in the sample, leading to preferential photoelectric effect occurrence from this element and thus finally to specific core-hole recombination involving this element [48]. It thereby offers the same XAS selectivity with

element. A XEOL spectrum of ZnO is given in Fig. I.18 as example, where the XEOL intensity increases at the Zn absorption edge (Zn K1s electron binding energy of 9659 eV) and oscillates for incident photons of higher energy [49].

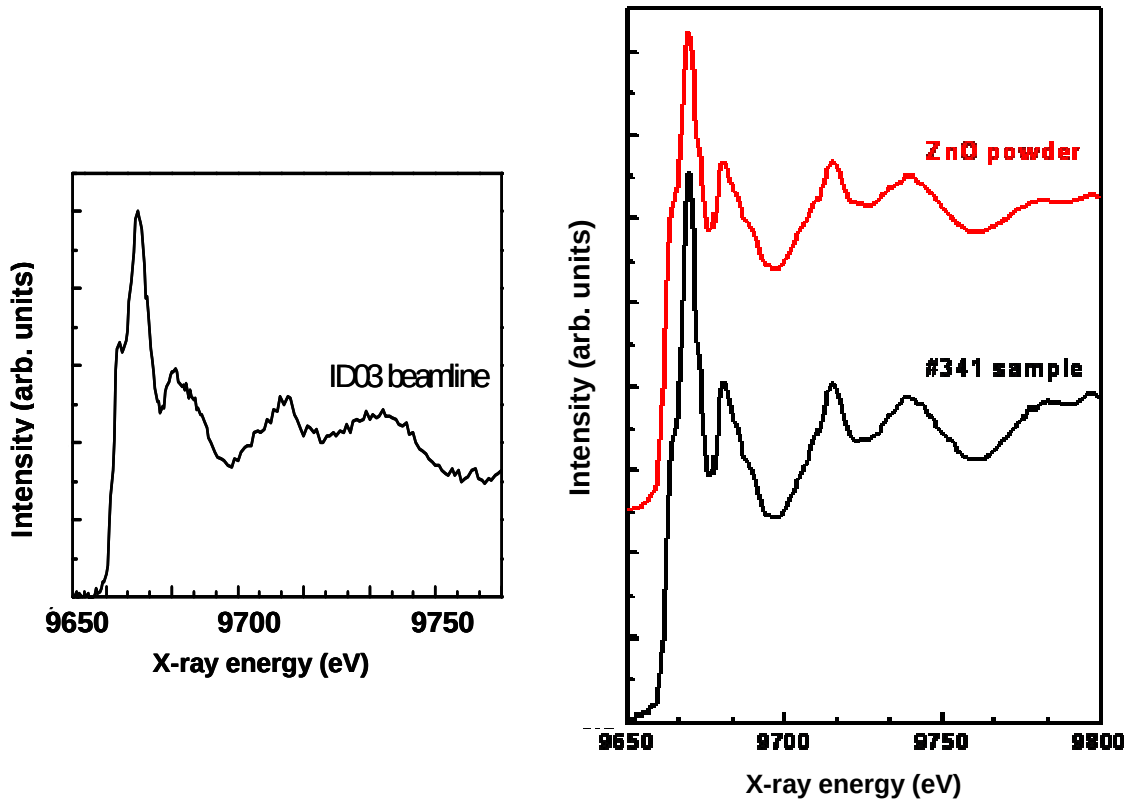

(b) **(a)**

Fig I.18 : *XEOL spectra of a) commercial stoichiometric ZnO powder (top) ; a ZnO layer (bottom) ; b)XEOL spectrum of the same ZnO layer obtained with our SNOM-SFM apparatus (described in chapter II)* [26, 50], (courtesy of S. Larcheri)

I.3: X-ray sources

Several types of X-ray sources exist and were used in this work. We can differentiate large scale facilities such as synchrotrons and, on the other hand, laboratory sources. These sources operate in different ways. Very bright sources are necessary to improve the signal/noise ratio of the techniques described in section I.2, especially for nanoobject signal detection. That is the reason why efforts have been devoted to the development of high brightness sources. In the figure I.19 is represented the evolution of sources brightness with time.

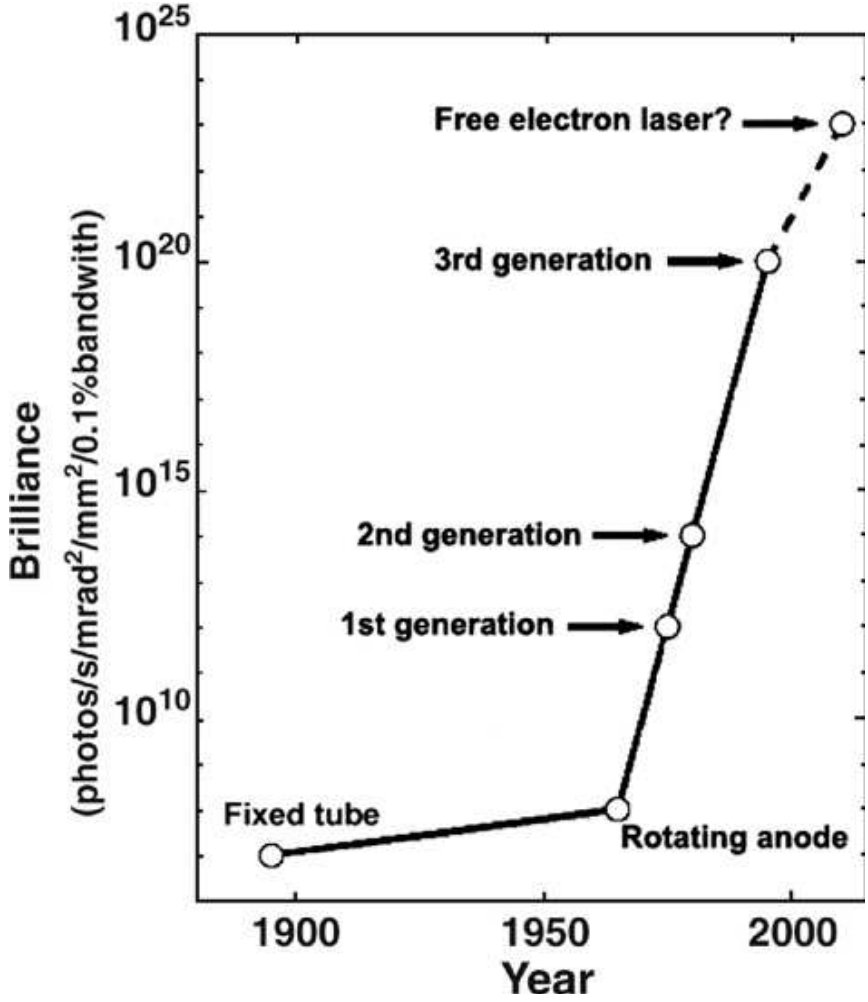

Fig I.19 : *Brightness of the X-ray sources as a function of time* [51].

I.3.1: Synchrotron X-ray sources

Synchrotrons are large scale facilities producing high intensity X-ray beams. These beams are tuneable in energy.

In order to produce synchrotron radiation, electrons are strongly accelerated in a storage ring in synchronization with their pass. They are forced to follow the curve path under magnetic fields and oscillate by antenna effect thanks to an undulator. An X-ray radiation is produced by Bremstrahlung tangentially to the storage ring. Doppler effect occurs which has the effect of emission wavelength shortening, leading to radiation frequencies in the X-ray range [32, 52, 53].

The produced radiation is very intense, pulsed, very collimated (divergence of a few mrad at SOLEIL [54]), with a good space and time coherency and very stable in position and intensity.

I.3.2 Laboratory X-ray sources

All of them operate in the same way, and are based on the Coolidge tube. A tungsten filament (cathode) heated by Joule effect at high temperature, emits electrons accelerated toward a metallic target (anode). Target atoms are excited under electron beam impact and their desexcitation process follows ways similar to those presented in part I.2. X-rays are thus emitted either by X-ray fluorescence, or by Bremsstrahlung. It originates from Coulomb interactions between incident electrons and the nuclei of the sample which curve the electron trajectory. As in the case of synchrotron radiation, this speed change leads to X-ray photon emission in a broad continuous spectral range. A laboratory X-ray source emission spectrum highlights thus target material characteristic and X-ray fluorescence peaks superimposed on a Bremstrahlung continuous spectrum (see Fig. I.20).

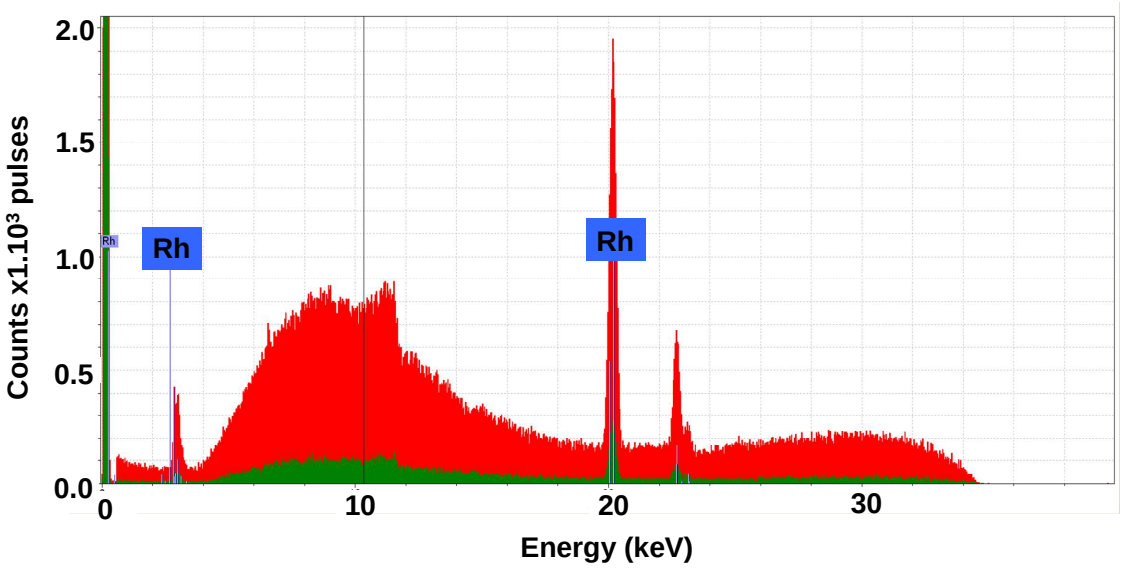

Fig I.20: *Spectrum of an Rh-target microsource at 35kV / 800µA (red) and 35kV / 100µA (green). Courtesy of IFG.*

More than 99% of the electrical power is lost and heats the target. The cooling of the target is thus of primary importance to increase the lifetime of the anode. It is performed by

air, water or by Pelletier effect cooling, depending on the source. The electron gun target system is placed inside a high static vacuum sealed chamber equipped with a beryllium window transparent to X-rays.

Rotating anode sources are based on the same principle. However, in this latter case, the continuous target rotation under electron beam excitation allows to change continuously the electron impact zone on the target, decreasing the heating effect. Consequently, such sources allow to significantly increase the target current.

Recently, liquid metal-jet-anode X-ray sources have been developed. In this case, the electrons are tightly focused on a liquid gallium jet target [55; 56] The high thermal conductivity of liquid gallium allows to increase the electrical power injected which leads to a very bright source (1.10^{11} Photons/(s·mm^2·mrad^2·line)) [57]

I.3.3 Free Electron Laser (FEL)

Free electron laser sources are another type of large scale facilities which can produce X-rays. Electrons are coherent so that their contribution efficiently add as they are accelerated (from 6-8GeV up to 17.5GeV at XFEL [58]) and guided along very huge undulators (hundred maters long in the case of XFEL [58]). As a result, short of flashes of highly coherent X-ray emission [59-61] are produced. Up to now, free electron laser sources provide highly coherent X-ray beam with average brightness between 10^{22} and 10^{23} photons / s / mm^2 / mrad^2. 10^{25} photons / s / mm^2 / mrad^2 are expected for European XFEL planed to start in 2015 [58].

In this work we have used a low power Rh target microsource provided by IFG-GmbH with 28 W maximum input electrical power (800 µA, 35 kV). The importance of such sources has grown significantly thanks to the developments of polycapillary lenses that focus X-rays onto micrometer size spots. This enables to deliver photons at high flux density.

I.4 X-ray capillary optics

Focusing X-rays is not trivial, and this field of research started in the XXth century when high power X-ray fluxes were needed.

Compton showed in 1923 that X-ray could be reflected on a smooth surface at grazing incidence angle. In 1931 Jentzch and Näring demonstrated the feasibility of using total reflection to guide X-rays. In 1948 was developed the first optical system by Kirckpatrick and

Baez [62], consisting in the use of two orthogonally crossed mirrors, each of them focusing X-ray beams in one direction. Then, Wolter developed another grazing angle X-ray mirror system in 1951 [63]**.** He invented three different ways to build an X-ray telescope by using hyperbolic and parabolic mirrors. They are widely used in astronomy. Montel Optics appeared in 1957 and consist in two mirrors mounted perpendiculary side by side [64].

Nowadays many other X-ray diffractive optic devices have been designed and marketted. First multilayer X-ray mirrors which work on diffraction at wide angles under Bragg conditions at the interface between two layers [65**].** Fresnel zone plates can focus X-rays on a nanometer range size spot (down to 30 nm [32, 66]). Curved mirrors have also been developed [67]. Diffractive optics are spectral-selective.

Refractive optics were also developed in the late 1990's by Snigirev although they were considered as inappropriate for focusing X-rays because refractive index of materials in the X-ray range is near unity and that strong absorption occurs. It consists in many individual refractive lenses arranged in a linear array made in low atomic weight materials (see for example ref [68]).

Capillary optics, invented in the early 80's by Kumakhov [69], are now widely used to guide and focus X-ray beams. We have used such optics in this study. A short description of their principle is given in the following sections. A review about X-rays micro focusing optics can be found in [70].

I.4.1: X-ray monocapillaries

In ref [71] Kumakhov and Komarov explained that they wanted to design X-ray and gamma optics to address five issues

(1) broad-band optics efficient from 0.1keV to 10 MeV

(2) high angular aperture

(3) high energy density delivery

(4) transformation of a divergent radiation to a nearly parallel beam, and focusing a parallel beam into a small spot

(5) The X- and gamma-ray optics should be compact and suitable for a manufacturing process.

For X-ray radiation the refractive index value is generally lower than 1 [72]. According to the Snell-Descartes refraction law, the only way to reflect X-rays is by total external reflection with an incident angle, (measured with respect to the surface) lower than a critical angle θ_{cr}. This critical angle is given by the following formula:

$$\theta_c(rad) = \frac{0.02\sqrt{\rho(g.cm^{-3})}}{E(keV)} \qquad \text{Eq (I.4) [73]}$$

where ρ is the reflecting matter density in $g.cm^{-3}$ and E is the primary beam energy in keV. θ_c value is around 4 mrad in the case of Co Kα line at 6.9 keV reflected on SiO_2. A mirror is not well suitable for X-ray reflection, even at grazing incidence, because of the low critical angle value. This problem can be solved using a curved mirror [74].

The solution found by Kumakhov [71] is to guide X-rays by multiple reflections in glass hollowed bent channels. If a given photon reaches the channel wall with an incident angle lower than the total external reflection critical angle, it will be reflected one or many times until it reaches the channel exit (see figure I.21a)). In the best configuration, the angular aperture of such a device is twice the critical angle of the material.

Capillaries can be made of glass. Usually light glass is used (borosilicate), but sometimes heavy glass (lead glass) may be more advantageous. Indeed the heavier is the glass, the larger is the value of the critical angle $\theta_c(E)$, although the absorption becomes larger. The best type of glass must be chosen depending on the optics application [75].

By bending the channel, photons will be guided at a focus point depending on the channel bending, as schematized in Fig. I.21b).

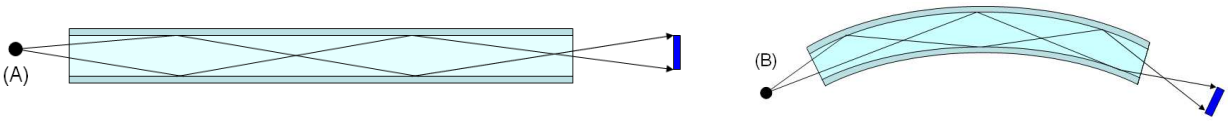

Fig I.21: *(A)Hollowed cylindrical channel guiding X-rays from a punctual source. (B) Bent hollowed channel guiding an X-ray photon beam from a point source.*

There are some limitations on the capillary curvature. Indeed a photon can be guided to the channel exits only if it is reflected on the inner wall with an incident angle $\theta<\theta_c$. Photons that penetrates the capillary perpendicularly to its entrance are reflected or not on the capillary walls depending on both capillary diameter and radius of curvature. The following equation must be verified:

$$\gamma \equiv \frac{r\theta_c^2}{2d} \geq 1 \qquad \text{Eq (I.5) [75]}$$

where d and r are respectively the capillary inner diameter and radius of curvature. If $\gamma<1$, a part of photons that enters in the capillary will be lost because of a too large incident angle. The channel cross section has a semi-moon form. Fig.I.22 illustrates this point in the case of $\gamma > 1$ (a) and of $\gamma < 1$ (b).

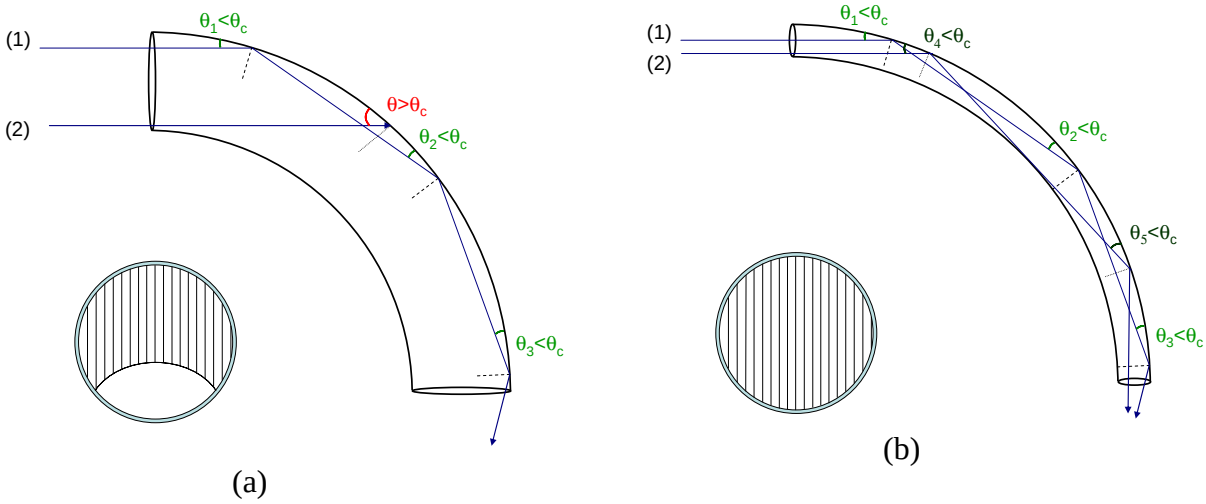

Fig I.22: *Illustration of the channel inner diameter influence on the X-ray guiding ability in the case where $\gamma>1$ (a) and $\gamma< 1$ (b). In each case, a close view of the cross section of the entrance is schematically presented. Photons passing through the striped area are guided. The reflection critical angle is enhanced for better understanding* [75].

I.4.2: Polycapillary lenses

From the preceeding considerations, by using a bench of bent channels, it is possible to focus X-rays from a punctual source to a small bright spot. This is achieved in polycapillary lens technology. Some examples are shown in figure I.23. Such X-ray lenses are able either to focus (“full lens”) or to collimate (“semi-lens”) the beam.

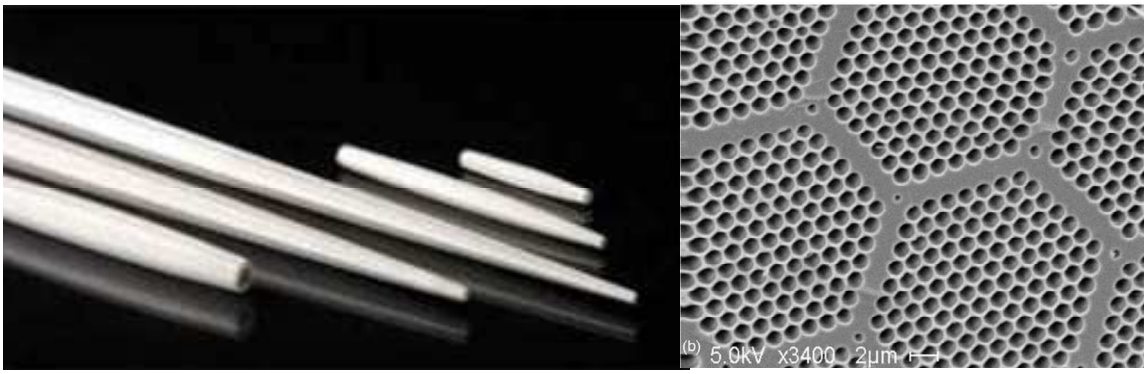

Fig I.23: P*olycapillary lenses (left)* [76], *SEM micrograph of a polycapillary lens cross section* [77]

Each polycapillary lens is designed and built on demand for a given source. The user must specify the target spot size, the focused spot diameter and the working distance (or focal distance). Fig.I.24 shows a polycapillary lens scheme.

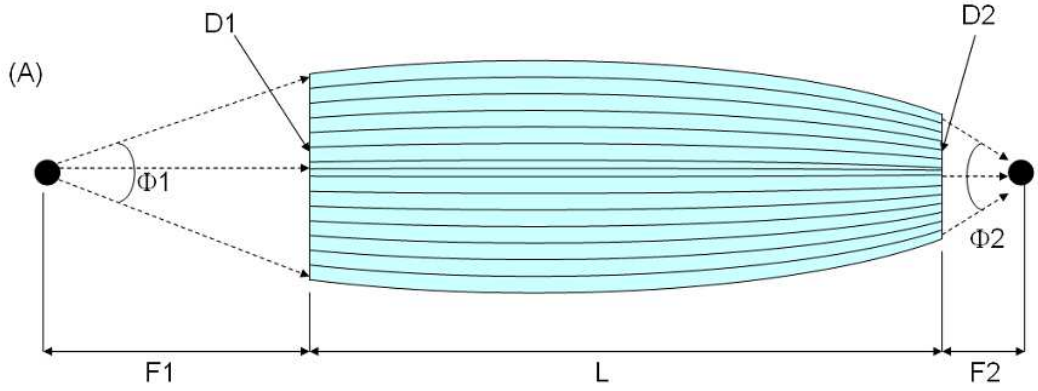

Fig I.24: *Scheme of a polycapillary lens*

ϕ is the lens angular aperture, D_{in} and D_{out} are the input and output lens diameter. f_1, f_2 are the source and focus focal distance respectively, L is the polycapillary length. The focus size varies with X-ray energy because of the critical angle dependence (see Eq I.3). The polycapillary lens provides a Gaussian shape beam whose FWHM is measured by scanning the focal plane with a 5µm lead pinhole equipping an EDX detector. Finally a lens is characterized by an intensity gain. This parameter is the ratio between the intensity measured by a detector through a capillary and the direct beam intensity through a pinhole of the same diameter. The detector-source distance is the same for both measurements.

An example of an X-ray source spectrum with and without focusing polycapillary lens is given in figure I.25. It evidences the intensity gain provided by the lens.

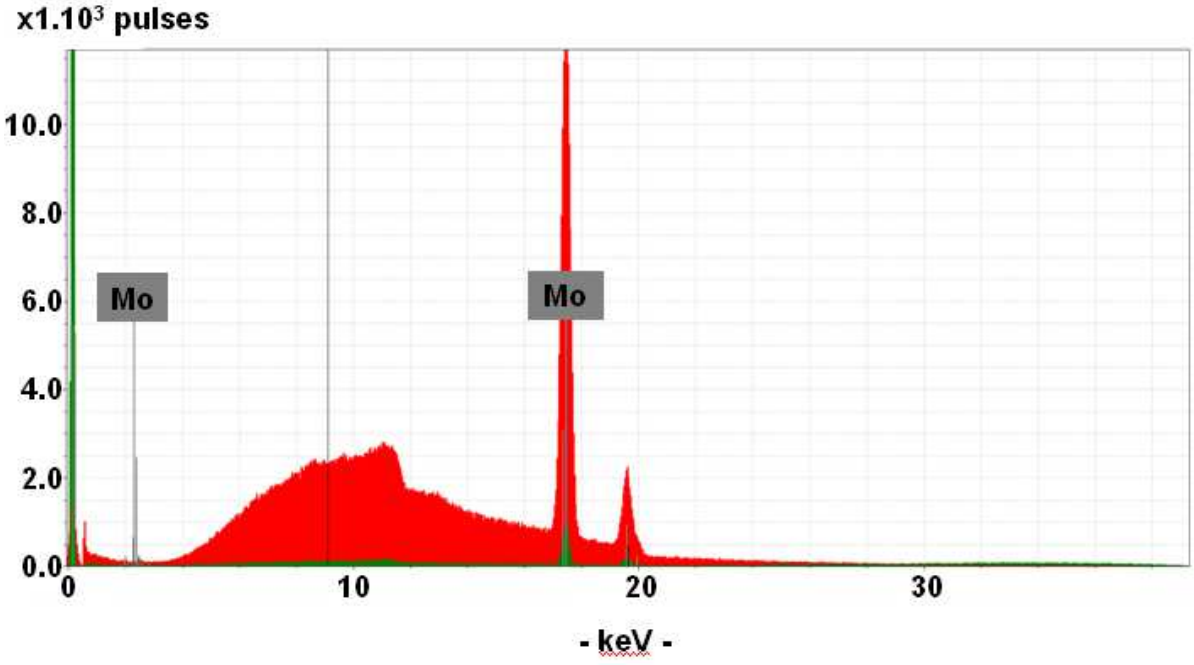

Fig I.25: *Spectra of X-ray emission from a Mo target microsource. In red: with a polycapillary lens (40 kV / 3µA), in green: without lens (40kV / 300µA). Courtesy of IFG-GmbH*

Underneath we present the polycapillary lens characteristics used in our experiments in Table I.1.

LENS 126mls05							
GEOMETRICAL PARAMETERS							
f_1, mm					49.2±0.1		
f_2, mm					7±0.1		
L, mm					103.8		
D_{in}, mm					5		
D_{out}, mm					1.5		
D_{max}, mm					7.2		
Φ, rad					0.101		
FOCUS PARAMETERS							
E, keV	3-5	5-7.5	7.5-10	10-15	15-20	20-25	25-30
Focus size, µm	31	35	35	25	18	17	17
Intensity gain	9459	1883	21349	21746	17827	7391	1574

Table I.1: *Polycapillary lens 126mls05 parameters. It was provided by IfG - GmbH (Institute for Scientific Instruments, Berlin)*

The polycapillary lens is optimized for a specific energy range (between 7.5 and 15 keV in our case) and the best intensity gain does not correspond to the shortest focus size, as can be seen in Table I.1. This is due to the critical angle variation with X-ray energy. This phenomenon is similar to chromatic aberrations in classical geometrical optics.

Our polycapillary lens is designed by IFG GmbH (Berlin) to maximize the intensity gain of our Rh target X-ray source, with a 7 mm exit focal distance. We chose this distance in order to keep opened the X-ray beam spot area avoiding shadowing effects by other equipments fitted to the source.

I.4.3: Elliptical capillaries

Elliptical monocapillaries can be provided also on demand. The principle is presented in figure I.26. Such capillaries are obtained from an elliptical shape bubble existing inside of the glass tube during pulling under heating. They have a better gain than cylindrical monocapillaries thanks to a wider angular acceptance. They are single reflection optics. With asymmetric elliptical capillaries, it possible to obtain a focus size smaller than the source size. [75]

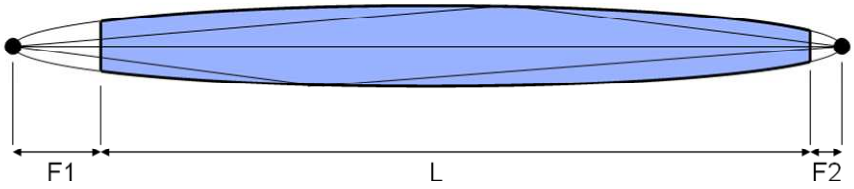

Fig.I.26: *Hollowed elliptical X-ray capillary. F1 and F2 are the capillary focal distances and L is its length.*

I.5 Summary

In this chapter, are presented the experimental techniques involved in the coupling of X-ray spectroscopies with Scanning Probe Microscopy. First I have described the Scanning Probe Microscopy principles and in particular those about the Scanning Near-field Optical Microscope as it was used for experimental work. Then I focused on the interaction of X-rays with matter to introduce X-ray Excited Optical Luminescence and X-Ray Fluorescence principles. Then I presented the main X-ray sources and their characteristics and finally X-ray capillary optics that now equip most of the focused sources. Moreover these optics were also used for detection in this work as it will be reported in Chapters II and IV.

References

[1] D. Rugar, H.J. Mamin, P. Guethner, S.E. Lambert, J.E. Stern, I. McFadyen, T. Yogi, "Magnetic force microscopy: General principles and application to longitudinal recording media", J. Appl. Phys, 68, 1169, 1990

[2] O. Pietzsch, A. Kubetzka, M. Bode, R. Wiesendanger, "Spin-Polarized Scanning Tunneling Spectroscopy of Nanoscale Cobalt Islands on Cu (111)", Phys. Rev. Lett., 92, 057202, 2004

[3] A.S. Duwez, S. Cuenot, C. Jerome, S. Rapino, F. Zerbetto, "Mechanochemistry: targeted delivery of single molecules", NatureNanotechnology, 1, 122, 2006

[4] G. Binning, H. Rohrer, "Scanning Tunneling Microscopy - from birth to adolescence", reviews of modern physics, 59, 3, part 1, 1987

[5] G. Binnig and H. Rohrer, "Scanning Tunneling Microscopy", Surf. Sci. 126, 236-244, 1983.

[6] L.E.C. van de Leemput and H. van Kempen, "Scanning Tunneling Microscopy", Rep. Prog. Phys. 55, 1165-1240, 1992.

[7] http://www.ieap.uni-kiel.de/surface/ag-kipp/stm/stm.htm from S. Woedtke, Ph.D. thesis, Inst. f. Exp. u. Ang. Phys. der CAU Kiel, 2002. (last accessed: 18/07/2013)

[8] http://pelletier.chez-alice.fr/chap1/c1.htm (last accessed 22/07/2013)

[9] G. Binnig, C. F. Quate and Ch. Gerber, "Atomic Force Microscope", Phys. Rev. Lett. 56, 9, 1986

[10] http://www3.physik.uni-greifswald.de/method/afm/eafm.htm (last accessed: 18/07/2013)

[11] G. Binnig, C. Gerber, E. Stoll, T.R. Albrecht and C.F. Quate, "Atomic resolution with atomic force microscope", Surface Science, 189–190, 1-6, 1987

[12] E. Synge, "A suggested Method for extending Microscopic Resolution into the Ultra-Microscopic Region", Philos. Mag., 6 , 356-362, 1928

[13] http://ansom.research.pdx.edu/introduction/sfm/ image adapted from: D. B. Nowak, "The Design of a Novel Tip Enhanced Near-field Scanning Probe Microscope for Ultra-High Resolution Optical Imaging" Ph.D dissertation, Portland State University, UMI 3419910, 2010.

[14] D. W. Pohl, W. Denk and M. Lanz, "Optical stethoscopy: Image recording with resolution λ/20", Appl. Phys. Lett., 44, 651, 1984

[15] A. Lewis, M. Isaacson, A. Harootunian and A. Muray, "Development of a 500 Å Spatial Resolution Light Microscope", Ultramicrosc., 13, 227, 1984.

[16] F. Zenhausern, M.P. O'boyle and H.K. Wickramasinghe, "Apertureless near-field optical microscope", Appl. Phys. Lett., 65, 1623, 1994

[17] E. Betzig, P. L. Finn, and J. S. Weiner, "Combined shear force and near-field scanning optical microscopy", Appl. Phys. Lett., 60, 2484, 1992

[18] M. Burresi, D. van Oosten, T. Kampfrath, H. Schoenmaker, R. Heideman, A. Leinse and L. Kuipers, "Probing the Magnetic Field of Light at Optical Frequencies", Science, 326, 550, 2009

[19] http://www.ntmdt.com/spm-principles (last accessed: 18/07/2013)

[20] S. Patanè, P.G. Gucciardi, M. Labardi and M. Allegrini, "Apertureless near-field optical microscopy ", Rivista Del Nuovo Cimento, 27, 1-46, 2004.

[21] M. Labardi, P.G. Gucciardi and M. Allegrini, "Near field optical microscopy", Riv. Nuovo Cimento, 23, 4, 2000

[22] Y. Kawata, C. Xu and W. Denk, "Feasibility of molecular-resolution fluorescence near-field microscopy using multi-photon absorption and field enhancement near a sharp tip", J. Appl. Phys., 85 1294, 1999

[23] P. Chevalier, Techniques de l'ingénieur, a214 Interaction du rayonnement avec la matière, 1986, http://www.techniques-ingenieur.fr

[24] W. Abdel-Rahman, E. B. Podgorsak, "Energy transfer and energy absorption in photon interactions with matter revisited: A step-by-step illustrated approach", Radiation Physics and Chemistry, 79, 552–566, 2010

[25] J. Als-Nielsen, D. McMorrow, "Elements of Modern X-ray Physics", John Wiley & Sons, Inc., Hoboken, NJ, USA., 2011, chapter 7: photoelectric absorption

[26] S. Larcheri, Joint use of x-ray synchrotron radiation microbeams and tip-assisted photon detection for nano-scale XAFS spectroscopy and chemically sensitive surface mapping, Università Degli Studi di Trento, Italia, 2007, thesis

[27] M. Newville, "Fundamental of XAFS", Consortium for Advanced Radiation Sources, available at http://xafs.org/Tutorials (last accessed: 18/07/2013)

[28] Y.-P. Sun, "Spontaneous and stimulated X-ray Raman scattering", Department of Theoretical Chemistry and Biology, School of Biotechnology, Royal Institute of Technology, Stockholm, Sweden 2011, thesis

[29] http://www4.nau.edu/meteorite/Meteorite/Book-GlossaryS.html at SIEGBAHN NOTATION (last accessed: 18/07/2013)

[30] Y. Cauchois, J. Despujols, Techniques de l'ingénieur, k750, "Constantes des spectres d'émission X", 1990, http://www.techniques-ingenieur.fr (in french)

[31] Nomenclature system for X-ray spectroscopy (1991) IUPAC. available at http://old.iupac.org/reports/V/spectro/partVIII.pdf (last accessed: 18/07/2013)

[32] See for example: X-Ray Data Booklet, Center for X-ray Optics and Advanced Light Source, Lawrence Berkeley National Laboratory, 2009, http://xdb.lbl.gov/ (last accessed 18/07/2013).

[33] M. West, A.T. Ellis, P.J. Potts, C. Streli, C. Vanhoof, D. Wegrzynek and P. Wobrauschek, "Atomic spectrometry update–X-ray fluorescence spectrometry", J. Anal. At. Spectrom. 25, 1503-1545, 2010

[34] K. Janssens, B. Vekemans, L. Vincze, F. Adams, A. Rindby, "A micro-XRF spectrometer based on a rotating anode generator and capillary optics", Spectrochimica Acta B, 51, 1661-1678, 1996

[35] L. Cheng, X. Ding, Z. Liu, Q. Pan, X. Chu, "Development of a micro-X-ray fluorescence system based on polycapillary X-ray optics for non-destructive analysis of archaeological objects", Spectrochimica Acta Part B, 62, 817-823, 2007

[36] J. Börjesson, M. Isaksson, S. Mattsson, "X-ray fluorescence analysis in medical sciences: a review" ,Acta Diabetol. 40, s39-44, 2003

[37] V. Kontozova-Deutsch, R.H.M. Godoi, A. Worobiec, Z. Spolnik, A. Krata, F. Deutsch, R. Grieken, "Investigation of gaseous and particulate air pollutants at the Basilica Saint-Urbain in Troyes, related to the preservation of the medieval stained glass windows", Microchim. Acta. 162, 425-432, 2008

[38] See for example: Handbook of Practical X-ray Fluorescence Analysis, ed. By Beckhoff, B., Kanngiesser, B., Langhoff, N., Wedell, R., Wolff, H., Springer 2006.

[39] M. Mantler. (2008), "Basic Fundamental Parameter Equations", in Modern Developments in X-ray and Neutron Optics, edited by A. Erko, M. Idir, T. Krist, A.G. Michette, Springer series in Optical Sciences, (Springer-Verlag Berlin Heidelberg) Vol.137, pp. 311-327.

[40] A. G. Karydas, "Self-element secondary fluorescence enhancement in XRF analysis", X-ray Spectrom. 34, 426-431, 2005

[41] N. Kawahara, "Complex Excitation Effects and Light elements" in Handbook of Practical X-ray Fluorescence Analysis, edited by B. Beckhoff, B. Kanngieβer , N. Langhoff, R. Wedell, H. Wolff, (Springer-Verlag Berlin Heidelberg), pp. 379-384 (2006).

[42] T. Shiraiwa and N. Fujino ,"Theoretical Calculation of Fluorescent X-Ray Intensities in Fluorescent X-Ray", Spectrochemical Analysis ,Jpn. J. Appl. Phys. 5 (1966) pp. 886-899

[43] D.K.G. De Boer, "Calculation of x-ray fluorescence intensities from bulk and multilayer samples", X-Ray Spectrometry, Volume 19, Issue 3, pages 145–154, June 1990

[44] T. Arai, “Correction of Matrix Element Effects”. in Handbook of Practical X-ray Fluorescence Analysis, edited by B. Beckhoff, B. Kanngießer , N. Langhoff, R. Wedell, H. Wolff, (Springer-Verlag Berlin Heidelberg), pp.16–19. (2006)

[45] Vié le Sage, “Etude théorique de la fluorescence-X des éléments légers et semi-légers. Correction mathématique des effets interéléments”, Thèse en sciences, Université Paris VII (1976) (In French)

[46] For example in the case of ZnO: P. A. Rodnyi, I. V. Khodyuk, “Optical and luminescence properties of zinc oxide” (Review), Optics and Spectroscopy, Volume 111, Issue 5, pp 776-785 (2011)

[47] A. Rogalev, J. Goulon, “X-Ray Excited Luminescence Spectroscopies”, In Chemical Applications of Synchrotron radiation, Sham, T. K., Ed., World Scientific : River Edge, NJ, 2002 ; Vol.2 ,Chapter 15

[48] A. Jürgensen, A.J. Anderson, T.-K. Sham, “An X-ray excited optical luminescence study of a zoned quartz crystal from an emerald-bearing quartz vein, Hiddenite, North Carolina, USA”, Physics and Chemistry of Minerals, 36, 4, 207-216, 2009.

[49] B. Hecht, B. Sick, U.P. Wild,V. Deckert, R. Zenobi,O.J.F. Martin and D.W. Pohl, “Scanning near-field optical microscopy with aperture probes: Fundamentals and applications”, J. Chem. Phys., 112, 7761, 2000

[50] C. Fauquet, M. Dehlinger, F. Jandard, S. Ferrero, D. Pailharey, S. Larcheri, R. Graziola, J. Purans, A. Bjeoumikhov, A. Erko, I. Zizak, B. Dahmani and D. Tonneau, “Combining scanning probe microscopy and X-ray spectroscopy”, Nanoscale research letters, 2011, 6:308

[51] A.G. Revenko, “Specific Features of X-ray fluorescence analysis techniques using capillary lenses and synchrotron radiation”, Spectrochimica Acta Part B, 62, 567-576, 2007

[52] H. Wiedemann ,“Synchrotron Radiation“, Springer-Verlag Berlin Heidelberg New-York, 2003 (avaible on Google Books)

[53] J. Doucet, J. Baruchel, “Rayonnement synchrotron et applications“, Techniques de l’Ingénieur, 2011 (in french)

[54] http://www.synchrotron-soleil.fr/portal/page/portal/Recherche/Bibliotheque/DocumentationEnLigne (last accessed 18/07/2013)

[55] O. Hemberg, M. Otendal and H.M. Hertz, “Liquid-metal-jet anode electron-impact x-ray source,” Appl. Phys. Lett. 83, 1483-1485. (2003)

[56] M. Otendal, T. Tuohimaa and H.M. Hertz, “Stability and debris in high-brightness liquid-metal-jet-anode microfocus x-ray sources,” J. Appl. Phys. 101, 026102. (2007)

[57] http://www.excillum.com (last accessed 18/07/2013)

[58] http://www.xfel.eu/overview/in_comparison (last accessed 18/07/2013)

[59] G. Grübel, G.B. Stephenson, C. Gutt, H. Sinn, T. Tschentscher ,"XPCS at the European X-ray free electron laser facility", Nucl. Instr. and Meth. in Phys. Res. B 262 (2007) 357–367

[60] H.-J. Foth, "Principles of Lasers", In Lasers in Chemistry Vol. 1: Probing Matter..Principles of Lasers, Edited by Maximilian Lackner 2008 WILEY-VCH Verlag GmbH & Co. KGaA, Weinheim ,Chapter 1

[61] http://www.xfel.eu/overview/how_does_it_work/ (last accessed 18/07/2013)

[62] P. Kirkpatrick and A.V. Baez, "Formation of Optical Images by X-Rays", J. Opt. Soc. Am. 38, 766, 1948

[63] H. Wolter, "Mirror systems with grazing incidence as image-forming optics for X-rays", Ann. Phys. (Leipzig), 10, 94-114, 1952 (original version in german)

[64] M. Montel, "X-ray microscopy with catamegonic roof mirrors, X-ray microscopy and microradiography", Academic Press, New York, 177-185, 1957

[65] A. Erko, "Diffraction Optics – Elements of Diffraction Theory", in Handbook of Practical X-ray Fluorescence Analysis, edited by B. Beckhoff, B. Kanngieβer , N. Langhoff, R. Wedell, H. Wolff, (Springer-Verlag Berlin Heidelberg), pp. 111-115. (2006)

[66] See for example http://www.aps.anl.gov/Beamlines/Directory, Nanoprobe Beamline „Nanoprobe 26-ID-C" (last accessed 18/07/2013)

[67] T. Mori and S. Sasaki, "Improvement of beam divergence in pseudoparaboloidal bending of an x-ray mirror", Rev. Sci. Instrum. 66, 2171, 1995

[68] A. Snigirev, V. Kohn, I. Snigireva and B. Lengeler, "A compound refractive lens for focusing high-energy X-rays", Nature, 384, 49 - 51, 1996

[69] A. Bjeoumikhov, N. Langhoff, R. Wedell, V. Beloglazov, N. Lebed'ev and N. Skibina, "New generation of polycapillary lenses: manufacture and applications", X-Ray Spectrom. 2003; 32: 172–178

[70] A.Snigirev and I.Snigireva. (2008), "Hard X-Ray Microoptics", in Modern Developments in X-ray and Neutron Optics, edited by A. Erko, M. Idir, T. Krist, A.G. Michette, Springer series in Optical Sciences, (Springer-Verlag Berlin Heidelberg) Vol.137, pp. 255-285.

[71] M.A. Kumakhov, F.F. Komarov, "Multiple reflection from surface X-ray optics", Physics Reports (Review Section of Physics Letters) 191, No.5 (1990) 289-350. North-Holland

[72] A. Bjeoumikhov, S. Bjeoumikhova, R. Wedell, "Capillary Optics in X-Ray Analytics", Part. Part. Syst. Charact. 22, 384–390, 2005

[73] A. Bjeoumikhov, S. Bjeoumikhova, "Capillary optics for X-rays", in modern Development in X-ray and Neutron optics, edited by A. Erko, M. Idir, T. Krist, A.G.

Michette, Springer Series in Optical Sciences, (Springer-Verlag Berlin Heidelberg) Vol.137, pp 287-306

[74] M.A. Kumakhov, “Channeling of photons and new X-ray optics”, Nuclear Instruments and Methods in Physics Research B48 (1990), 283-286

[75] V. Arkadiev, and A. Bjeoumikhov, “Mirror Optics”, in Handbook of Practical X-ray Fluorescence Analysis, edited by B. Beckhoff, B. Kanngieβer , N. Langhoff, R. Wedell, H. Wolff, (Springer-Verlag Berlin Heidelberg), pp. 89-111 (2006).

[76] http://www.ifg-adlershof.de/ (last accessed 18/07/2013)

[77] E. Langer, S. Däbritz, W. Hauffre, M. Haschke, “Advances in X-ray excitation of Kossel patterns by a focusing polycapillary lens”, Appl. Surf. Science, 252 (2005), 240-244

.

CHAPTER II: Mapping of X-ray induced luminescence using a SNOM probe

Simultaneous acquisition of sample topography and visible luminescence mapping of a sample under X-ray excitation is possible by luminescence local collection via a sharp optical fibre used as a shear force microscope probe. However, conventional shear force head equipments do not offer access for X-ray illumination. We have thus developed a shear force microscope head that can be easily fitted to a synchrotron beam line or to an X-ray laboratory source. The microscope is controlled by a Nt-Mdt^{TM} SMENA controller. We first describe the instrument and the calibration samples used for concept and equipment validation. Then the results of preliminary tests in synchrotron facility (X-tip European contract, STREP # NMP4-CT-2003-505634) as well as the results of experiments using a laboratory source (LUMIX European contract, EUREKA-EUROSTARS E4383) are discussed.

II.1: Experimental setup

The instrument is designed first to collect the visible luminescence as well as to record the topography of the sample. It uses a sharp optical fibre tip to collect local X-ray Excited Optical Luminescence signal. The visible luminescence is sent to a detector via an optical fibre. The detector can be a simple photodiode for total luminescence collection or a spectrophotometer.

In figure II.1 is shown the scheme of the experiment. In order to maintain the tip-X-ray beam alignment, it was chosen to keep the tip in a fixed position regarding the beam while the sample is moved in a plane perpendicular to the tip holder for sample imaging process. For this reason, the sample is positioned on a commercial x, y, z piezoscanner tube (NT-MDT). The fine motion is operated via this scanner and the maximum scan window (y, z axis) is 120 x 120 µm. The maximum piezo elongation in x-direction (motion controlled by the microscope feedback loop) is about 5µm. The scanner is fixed on a piezo stack (Attocube, ACN150) allowing sample coarse displacement in X_s, Y_s and Z_s axis.

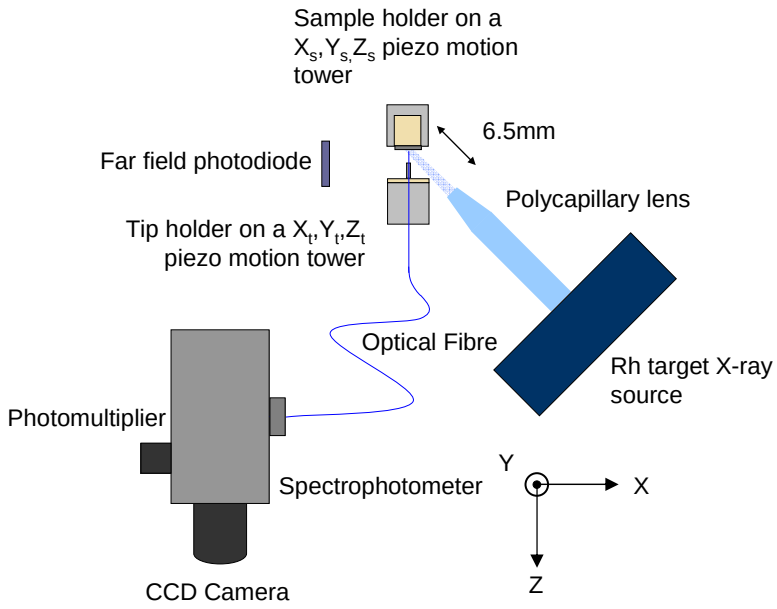

Fig.II.1: Experimental setup of simultaneous luminescence and topography mapping through a SNOM probe tip

The tip is a sharp aluminium coated optical fibre (aperture diameter of 70nm, bandwidth: 400-600nm) glued on a quartz tuning fork oscillating at 32kHz (see figure II.2a)). This system is available on the market. It is welded on an printed circuit board equipped with 3 magnets (figure II.2b) on the right). This latter step is clearly the most critical in the microscope preparation before operation. Both tuning fork contacts are connected via two of the three magnets. The whole device is then placed on the microscope tip-holder, also equipped with three magnets and fixed on another X_t, Y_t, Z_t piezo stack (Attocube ACN150). The tuning fork power supply occurs via the magnets in contact. The tip is perpendicular to the sample surface. A picture of the apparatus is shown in figure II.2c), and a close view of the tip-sample area is visible in figure II.2d). The whole system is fixed on a 20 cm diameter metallic flange fixed on a damping stage system.

a)

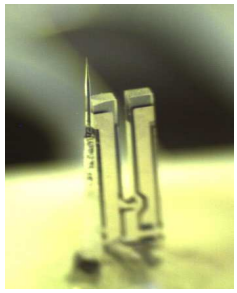

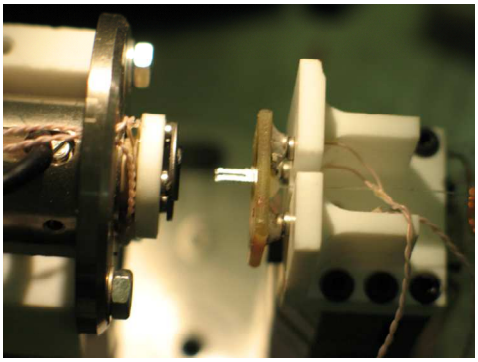

b)

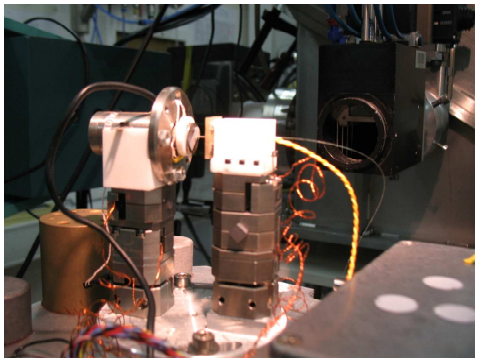

c)

Fig.II.2: *Photographies of the Sharp probe-tip glued on the quartz tuning fork a), Tip-holder (right) and Sample-holder (Left) face to face (Photographies taken at the ESRF) b) and c). The whole system is fixed on a 20 cm diameter flange.*

Before microscope running, the X-ray beam spot must be aligned regarding the tip apex. This operation occurs in three steps of coarse and fine alignments, one step per tip degree of freedom X_t (horizontal in the sample plane), Y_t (vertical in the sample plane) and Z_t (horizontal and perpendicular to the sample plane). To ensure a friendly-use alignment process, a fluorescent screen sheet is stuck on the sample holder just above the sample. A CCD camera + zoom optical system allows to observe the tip apex, the fluorescent spot with a few micrometers accuracy. The sample is approached toward the tip-probe to position it in the X-ray optics focal plane (action on Z_s-axis). This plane is perfectly defined on synchrotron beam lines as well as using a laboratory source. A photodiode detector is positioned laterally (Fig. II.1) to collect in far field the sample luminescence. The primary X-ray source (laboratory or synchrotron source), focused on the screen over a micronscale area, is switched on. The tip apex position is moved regarding the beam spot by action on the coarse X_t motion while both beam and sample remain in a fixed position. Alignment is eyed controlled on the video screen since it is easy to align the apex with the brightest beam spot part (first axis). The tip is then displaced along Y_t-axis while measuring the luminescence signal provided by the lateral photodiode. At the beginning of the scan, the signal is maximum, then it decreases till a

minimum value reached when the tip is centred with the beam centre, due to shadowing effect. Then the signal increases to reach the initial value. The minimum position corresponds to the tip-spot alignment according Y_t axis (second axis). Then the sample is moved according Y_s axis (vertical in-plane motion) to position the primary beam spot on the sample of interest. Finally the tip is approached toward the surface as much as possible avoiding tip-sample contact (Z_t motion eyed-controlled on the video screen) and further engaged on the sample surface in near field interaction with the sample (X_s motion). Fine alignment acting on X_t and Y_t piezo actuators by unit steps by optimization of the signal collected through the optical fibre.

In a preceeding thesis, the equipment was first fitted by Larcheri at al to ID03 beamline (ESRF-Grenoble, France) [1]. The spot diameter was around 20 µm. Then, during my thesis, a Rh-target laboratory microsource was tested. This source operates at 800 µA current under 35 kV acceleration voltage. It is equipped with a polycapillary lens providing a high brightness Gaussian excitation spot of 22 µm radius measured at 1/e. The photon flux within the beam spot is about 10^9 photons.s^{-1}.μm^{-2} (see section III.1.2 for the laboratory source primary beam spot characterization). In comparison, the photon flux in synchrotron environment is 3.10^{10} photons.s^{-1}.μm^{-2} (at the ID03 beamline of ESRF for the 20x15µm spot)

During the topographic mapping, the luminescence signal emitted by the sample through X-ray illumination is collected through the sharp tip optical fibre and is sent either to a photodiode for whole luminescence collection or to a spectrophotometer (Princeton SP2300) for luminescence spectrum acquisition. The spectrophotometer is equipped with 3 gratings of 150, 300 and 600 grooves/mm providing respectively 21.2, 10.5 and 5.12 nm/mm linear dispersions (measured at 435.83 nm) of PM (PhotoMultiplier) aperture, corresponding to the respective full scale wavelengths of 569, 281 and 137 nm. This work is performed with the 150 grooves/mm grating, and with a PM slit of 10 µm. The PM bias is fixed at 8 kV. The PM current is amplified by an I-V converter of high gain (10^7 V/A). The PM signal is sent to the data acquisition board of the SMENA controller which allows to display twin images topography-visible luminescence mapping. Note that the spectrometer is also equipped with a CCD camera in order to obtain directly the luminescence signal spectrum.

We here present the preliminary tests results obtained with our equipment.

II.2: Instrument testing

II.2.1: Results on a synchrotron beamline

The resutlts on a synchrotron beamline were obtained by Larcheri at al. in a preceeding thesis [1]. The apparatus (fig II.1) was first brought at ESRF ID03 line [1; 2]. A $ZnWO_4$ – ZnO thin layer (~400nm) was prepared by co-sputtering Zn and W onto a silicon substrate followed by a 900°C annealing in air in order to check the feasibility of the technique and the performance in terms of lateral resolution.

Twin mapping images of the simultaneous topography and visible luminescence collection were recorded at different X-ray incident energies (fig II.3). Each image contains 1024 x 1024 pixels. The stability of the instrument is excellent since neither mechanical nor thermal drift was observed during the 8 hours experiment needed to record the whole set of images.

The idea is to highlight the different areas containing ZnO and $ZnWO_4$. For that purpose each twin image is recorded at an incident beam energy below and above the Zn-Kα absorption threshold (Fig. II.3a),e) at 9600 eV and II.3b),f) at 9664 eV respectively). Another set is recorded below (Fig. II.3 c),g)) and above (Fig. II.3d), h)) the W-L3 absorption threshold at respectively 10190eV and 10207eV. In Fig. II.3, a) to d) are topographic images, while e) to h) images correspond to the luminescence mapping. Black zones correspond to grains that are not emitting or that emit with a low emission yield or out of the fibre acceptance angle (22°). No direct correlation is visible between the topographic and the luminescence images because the emitting centres are not localized and light can diffuse into the sample.

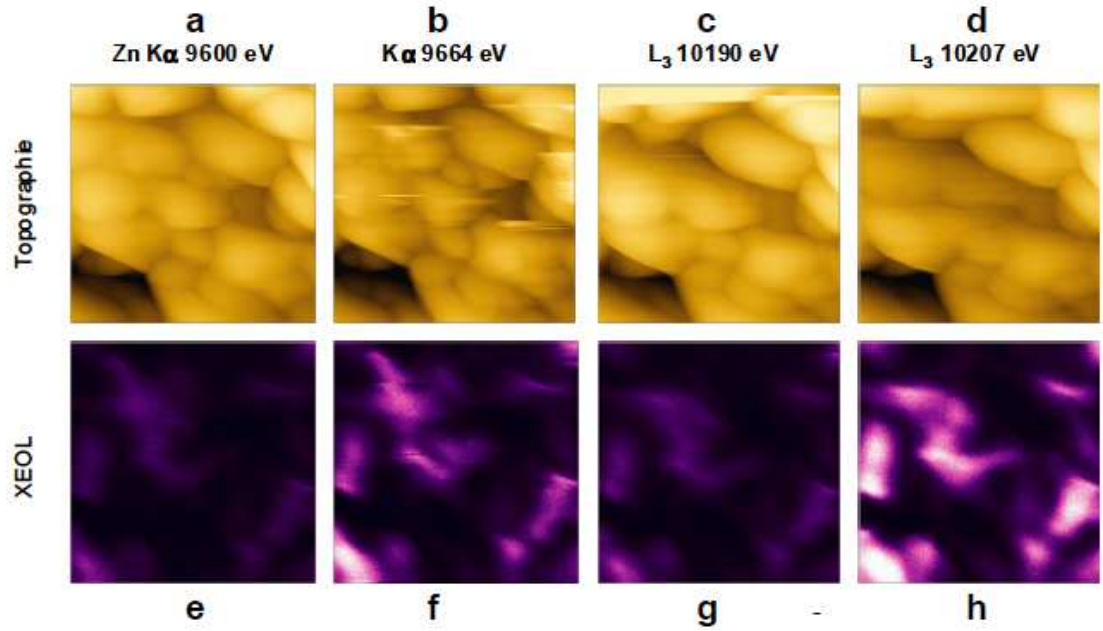

Fig.II.3: *topography (4a to 4d) and visible luminescence map (4e to 4h) simultaneous acquisition of $ZnWO_4$-ZnO thin layers deposited by co-sputtering on silicon wafer. Scan window: 18 x 18 µm²* [1;2].

Post image processing can be carried out on figures II.3e) to II.3h) to define ZnO and $ZnWO_4$ rich areas [2], as shown in figure II.4. The comparison between fig II.3e and II.3f (resp. II.3g and II.3h) highlights Zn-luminescent areas (W-luminescent areas resp.). Then, to enhance the contrast, these two images are further converted in black and white scale. By this way we get two intermediate images, which are then used to obtain a chemical mapping of the layer: the ZnO rich emitting areas can be obtained by difference of these intermediate images (Fig. II.4a), since Zn is present in both materials while W can be found only in $ZnWO_4$ grains. Finally, a logic operation 'AND' is applied between the intermediate images to highlight the distribution of emitting $ZnWO_4$ (figure II.4b) since Zn must be present in both materials. In fact a white pixel in figure II.4b is obtained only if the same pixel appears simultaneously white on both intermediate images. This image processing leads to a two-level (black and white) image which increases significantly the contrast. Since Fig.II4a shows only few features, one can conclude the emitting centres are almost pure $ZnWO_4$, as confirmed by XRD and micro-Raman analysis [1]. Fig. II 4c shows the superposition of both II.4a and II.4b images. This image combination clearly highligths $ZnWO_4$ (blue areas) and ZnO (red areas) emitting centres cartography.

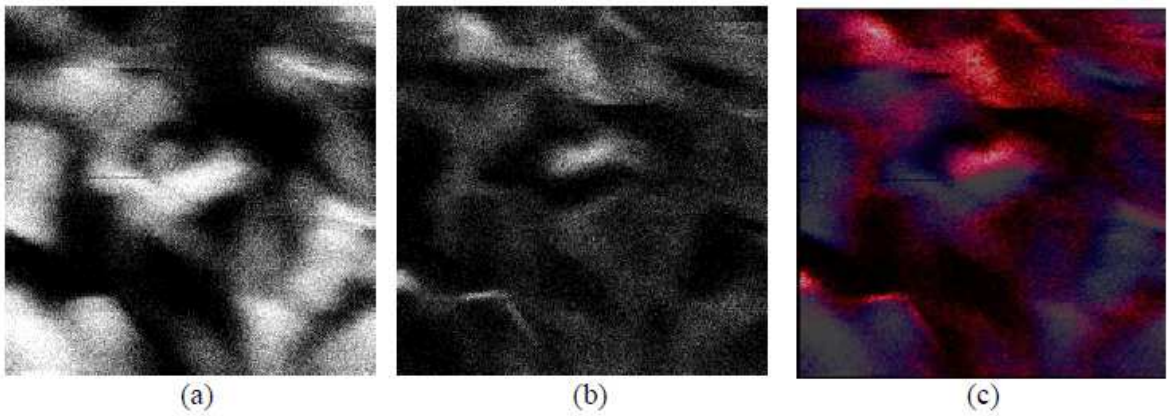

Fig.II.4. *Post-processing of images presented in Fig II.3 (see text). (a) ZnO rich emitting areas highlighting. (b) distribution of emitting $ZnWO_4$ centres. (c) Superposition of (a) and (b) images. ZnO (resp. $ZnWO_4$) rich areas in red (resp. in blue). Scan window 18x18µm².*

By stopping the sample surface scan, it is possible to perform XAS-XEOL acquisition on a peculiar area of the sample surface. This experiment is performed on ZnO layers (~400nm), prepared by Zn sputtering followed by a 900°C annealing in air. This sample is first characterized in conventional XAFS-XEOL spectroscopy, at the ESRF ID03 line. The spectrum (fig II.5a).bottom) is compared with that of a commercial stoichiometric ZnO powder sample used as reference (fig. II.5a).top). The threshold localized at 9.6586 keV, is characteristic of visible light emitted by Zn atoms after X-ray absorption. The very good agreement both in term of peak positions and relative magnitudes measured with respect to the average signal above threshold indicates that the ZnO sputtered layer is stoichiometric. The XAFS-XEOL spectrum presented in fig II.5b) is recorded by the apparatus on the same sample and is in very good agreement with those shown in fig II.5a). It is obvious that the light emitted within the fibre aperture (~50nm) exhibits in this case a luminescence spectrum close to that of a stoichiometric ZnO sample.

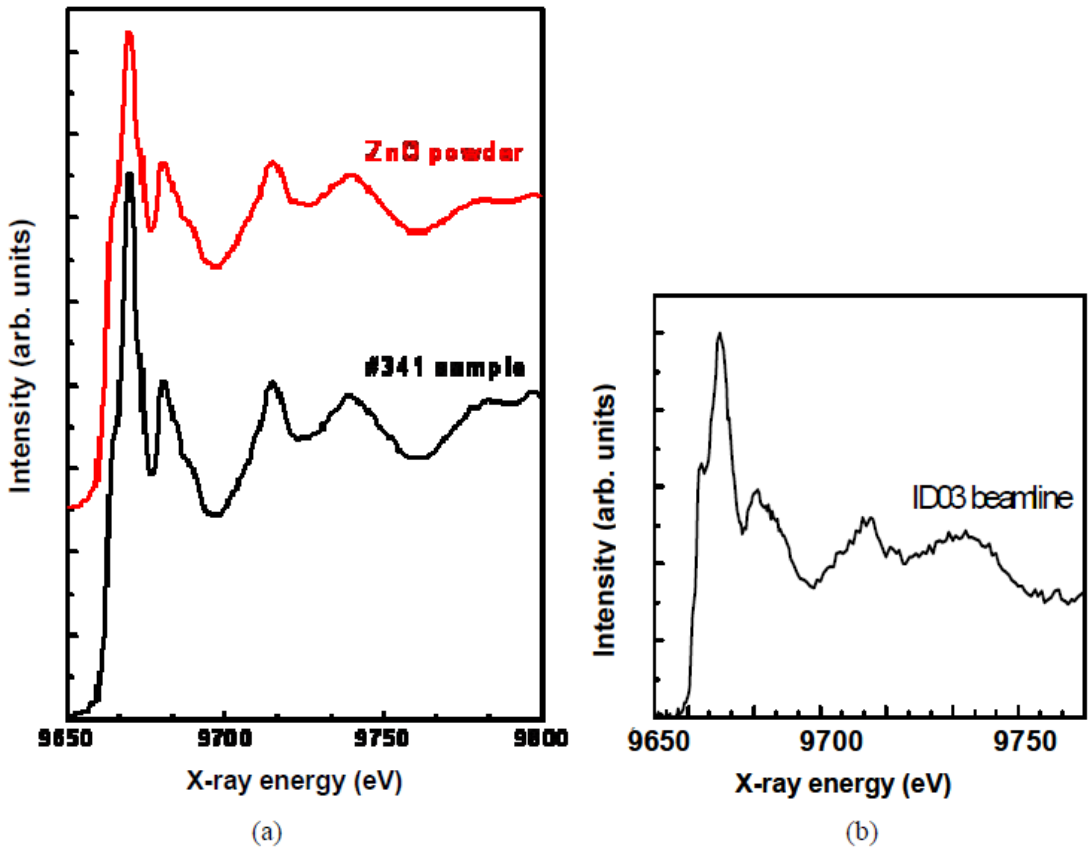

Fig II.5: *XAS-XEOL spectra of (a) commercial stoichiometric ZnO powder (top); ZnO layer (bottom); (b) spectrum of the ZnO layer obtained with the instrument* [1; 2]

II.2.2 Results with a laser excitation source

In this experiment the apparatus is equipped with a cw He-Cd laser (λ=325nm, power 15mW, flux of 2.10^{13} photons.s^{-1}.μm^{-2}) as excitation source [3] and works in a classical SNOM configuration.

Fig. II.6 shows a twin image topography-visible luminescence map obtained on ZnO stoichiometric clusters spread from a solution of commercial ZnO powder in ethanol and deposited on a silicon nitride grating. The topographic image (Fig. II.6a)) clearly exhibits both the silicon nitride grating and individual ZnO grains. In fig II.6b, only the ZnO grains are luminescent because silicon nitride is not at this excitation wavelength. Grain size varies in the 0.5 to 4 µm range. We can notice that some grains are visible on both images while others are visible only in the topographic image. In fact, each grain does not necessarily emit light. Moreover, some grains are partially emitting, or possibly the luminescence is not detected over the whole grain (see for example top left Figure II.6a) and II.6b) top left).

The correlation between both images is high, however grains seem smaller on the luminescence mapping image. It can be understood by focusing on the evanescent wave collection process (from the aggregate surface). It considers the optical fibre apex as diffusive and the aggregate size discrepancy between luminescence and topographic mapping could be attributed to a quenching effect from the aluminium coating to the ZnO emissive sites. Another explanation considers that luminescence is collected in a propagating mode: Simple geometric considerations [3] can explain this discrepancy linked to the convolution phenomenon between the grain shape and the tip geometry for topographic image or tip aperture for luminescence mapping. Fig. II.7 illustrates this effect. Indeed, the light collected by the fibre-tip comes from ZnO emission sites inside a cone with an angle corresponding to the fibre acceptance. The analysis is performed in depth, and the thickness of the probed material is limited by the luminescence wavelength attenuation length in ZnO. When the tip is on top of a ZnO grain, this acceptance volume is localized inside the grain and a strong luminescence signal is detected. When the tip scans the sample, the luminescence signal drastically decreases before the tip reaches the grain border because a great part of the acceptance volume is outside the grain. This effect can be quantified and for a 2 µm radius spheric grain imaged by a 50 nm radius of curvature spherical tip, the apparent grain radius in the luminescence map is 1.86 µm. This corresponds to a 7% variation in grain diameter between topographic and luminescence images, in good agreement with experiment (Fig. II.6).

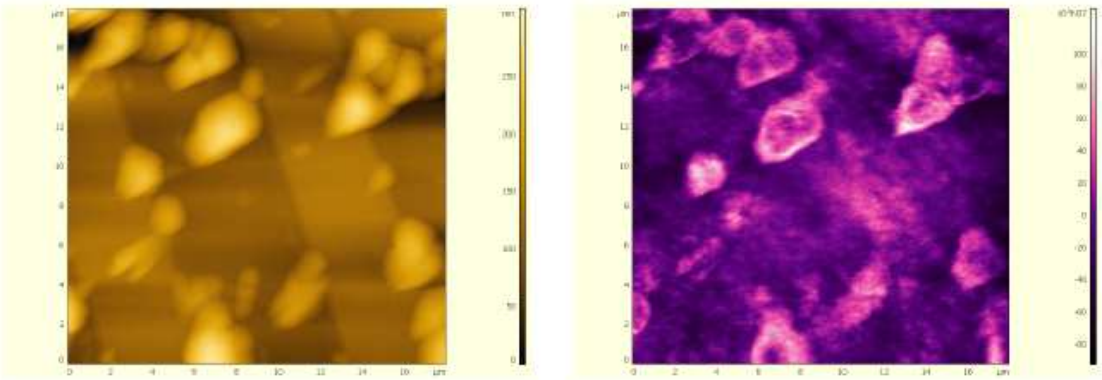

Fig II.6: *17x17 µm² SNOM-Shear Force image of ZnO clusters spread over a silicon nitride grating. a) topography image. b) Luminescence mapping* [3]

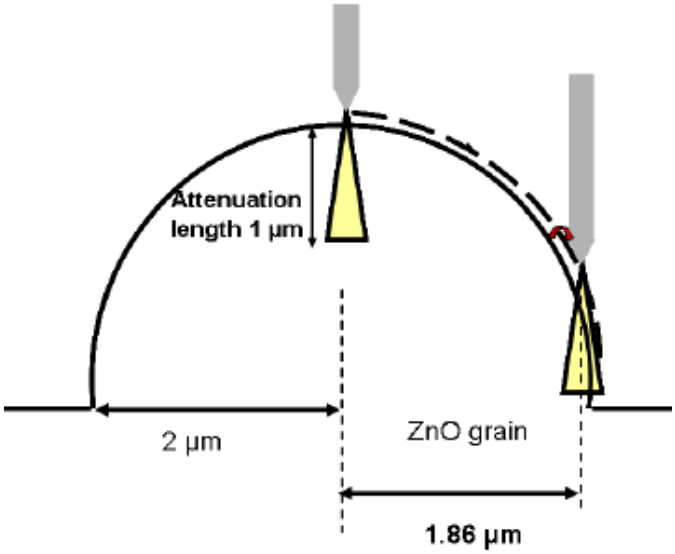

Fig: II.7: *Scheme of a sharp SNOM probe scanning a micronscale ZnO grain* [3]

II.2.3: Results with a laboratory micro-source

Results presented in sections II.2.1. and II.2.2. were obtained using high brightness sources. We wanted to know if it was possible to obtain a significant signal/noise ratio using a laboratory microfocused X-Ray source. For this purpose, two types of samples were used to evaluate the apparatus performance. Both are known for their strong luminescence under X-ray illumination:

- Uranyl compounds deposited on paper. It is commonly used as luminescent screen for X-rays.
- Powder mixtures of ZnO and ZnS embedded in PMMA resist, spin-coated on silicon and finally dried at 100°C.

This work is described in [4].

The simultaneous topography and luminescence mapping of the luminescent screen is shown in the figure II.8.

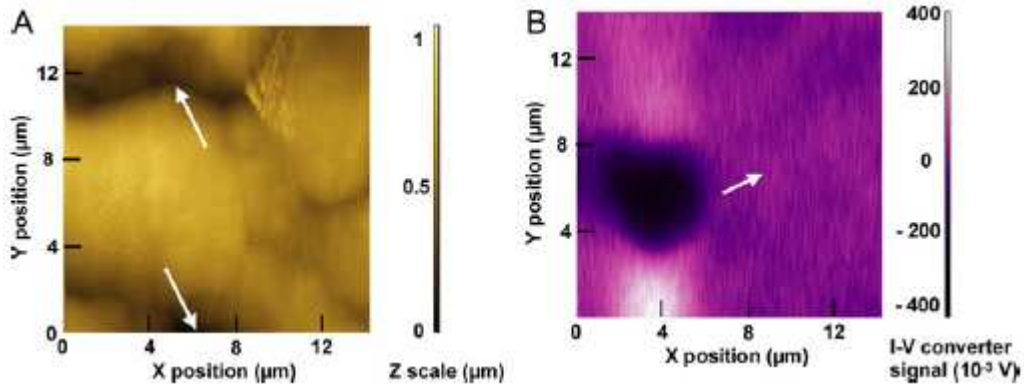

Fig II.8: *Luminescent uranyl screen characterization. Imaging conditions: scanned surface 14 µm×14µm, 1024×1024 pixels, 5 s per scan line. a) Topographic image. The arrows show depressions at the sample surface. b) Luminescence mapping (PM voltage 8 kV). The arrow shows the fixed position where the photoluminescence spectrum presented in Fig. 26 (red line) was recorded.* [4]

In Fig.II.8.a) we show the topography of the luminescent screen. The full vertical scale of the image is 1 µm. The topography clearly shows grains of 2 to 8 µm diameter. The RMS (Root Mean Square) roughness is in the range 150-170 nm. By comparison with the topographic image obtained before opening the X-ray source shutter (not shown here), we believe that this image is not distorted during X-ray irradiation by the Rh-Kα source, although both sample and tip could be heated by illumination and thus could thermally expand. Moreover, electrostatic interactions should occur between tip and sample, due to photoelectron emission under X-ray radiation, modifying tip-sample interaction and thus possibly affecting the topographic image.

Fig. II.8b) presents the luminescence mapping of this sample, simultaneously acquired with the topography at the maximum luminescence intensity (552 nm, Fig. II.9). Black (respectively white) zones correspond to non-emitting (respectively maximum emitting) areas. In the topographic image (Fig. II.8a) bottom center or top-left corner), we observe hollows, from which emission is observed on the luminescence map (Fig. II.8b)). However, on the wide grain on the left hand side of Fig.II.8a), a non emitting zone is observed on the luminescence map. Note that both images are simultaneously recorded so both topographic and luminescence images exactly overlap. Shadowing effects by the tip must be excluded because the tip remains in a fixed position regarding to the excitation beam, otherwise the image should appear completely dark. Grain curvature could explain luminescence intensity decrease in case the luminescence is emitted out of the fibre apex acceptance. However, the

topographic image tends to show that this phenomenon does not occur here. Finally, the tip-sample distance is controlled by a feedback loop operating on the vertical sample motion to keep the tip-sample near field interaction constant. This control provides the topographic image and does not operate on the luminescence signal. The screen is made of a highly luminescent material and even in the hollows observed on topographic images, luminescence coming probably from the material underneath is collected. No luminescence contrast was expected but experience probably highlights a damaged area in the screen. This could not be deduced from the topographic image.

During illumination, the sample scan was stopped at a fixed position under the SNOM tip. A photoluminescence spectrum was then recorded on a grain, while the feedback loop of the microscope remained activated to maintain the tip-sample distance constant (Fig. II.9 red line). This spectrum has good signal to noise ratio and we observe peaks positioned at 385, 420, 441, 461, 494, 547, 552, 591, 595, 625 nm (respectively 25974, 23809, 22675, 21692, 20242, 18280, 18115, 16920, 16806, 16000 cm^{-1}). Uranyl groups UO_2^{2+} luminescence spectrum exhibits characteristic peaks at 491, 511, 535, 561 and 587 nm [5, 6]. Eu^{3+} ions provide two main luminescence peak centered at 592 and 613 nm [7]. A peak shift (in the range of 3 to 12 nm) is clearly observed in our experience regarding literature. It can be explained by the fact that the spectrum varies with the chemical environment of the emitting complex [5, 6]. Finally our spectrum presents characteristics of europium uranyl compounds which are currently used for commercial fluorescent screens.

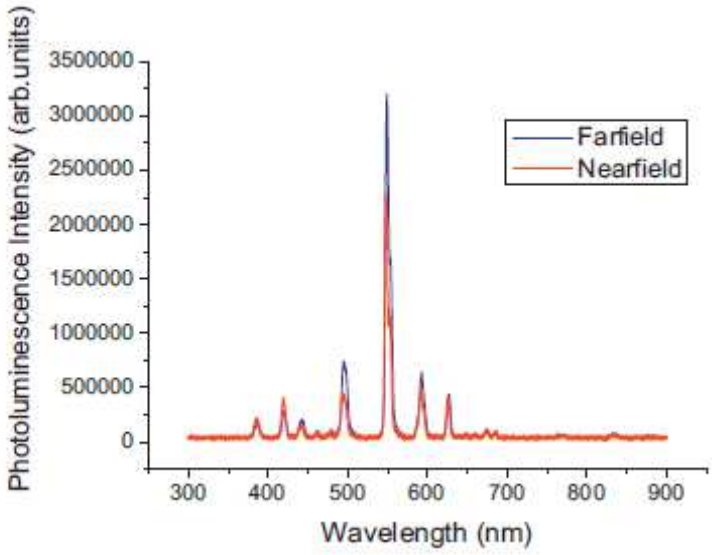

Fig II.9: *Photoluminescence spectrum of the fluorescent screen: in near-field configuration (red line) at the fixed position shown by the arrow in Fig. II.8b), and in far-field configuration (blue line) with a wide core fibre, for comparison. The slit aperture at the PM input was adjusted to reach about the same signal magnitude in the far- and in the near-field modes. PM voltage: 8 kV.* [4]

When the sharp optical fibre is removed and replaced by a 400 µm core diameter commercial optical fibre, placed at about 10 mm (in the far field acquisition conditions) from the surface and connected to the spectrometer, the recorded spectrum exhibits similar peaks, as shown by the blue line in Fig.II.9. Note that the spectrometer input slit aperture was adjusted to reach similar signal magnitude in near and far field acquisition modes. The peaks obtained in both cases, far and near field modes of acquisition, are centred at the same values. However, the peak intensity ratios depend on the acquisition mode. Several hypothesis can explain this phenomenon. First, acquisition in the far-field mode leads to an average spectrum of the whole emitting surface. In the near-field conditions, light collection is local and the sample chemistry may vary with the tip position on the surface. Second, the sample natural roughness may affect the light collection due to SNOM tip axis-sample angle variations. In future, we must take address these issues for spectra comparison with literature data.

Then a second type of sample was used, a ZnO/ZnS powder mixture embedded into PMMA resist and spread over a silicon sample. An optical observation of the sample is

presented in the figure II.10 (field of view: 820µmx650µm). In this figure, a grain size distribution in the range of 2.5 to 35 µm is observed.

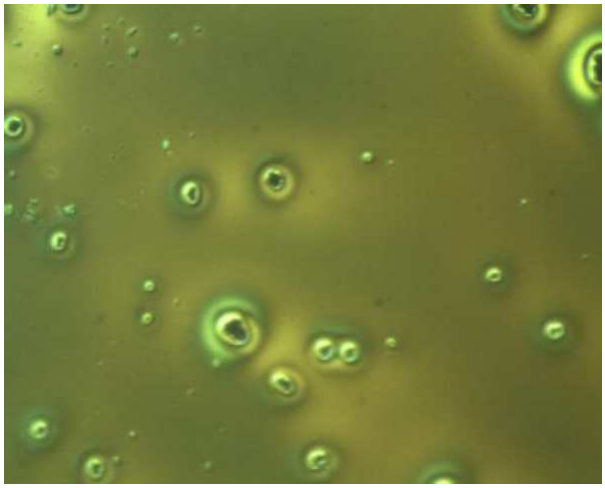

Fig II.10: *Optical bright field micrograph of ZnO and ZnS grains embedded in PMMA resist spread on a silicon wafer and then dried. Field of view: 820µm×650µm.* [4]

The sample is also observed by SEM (Scanning Electron Microscopy) and analysed by in-situ EDX (Energy Dispersive X-ray). Two types of grains were observed (see Fig.II.11).

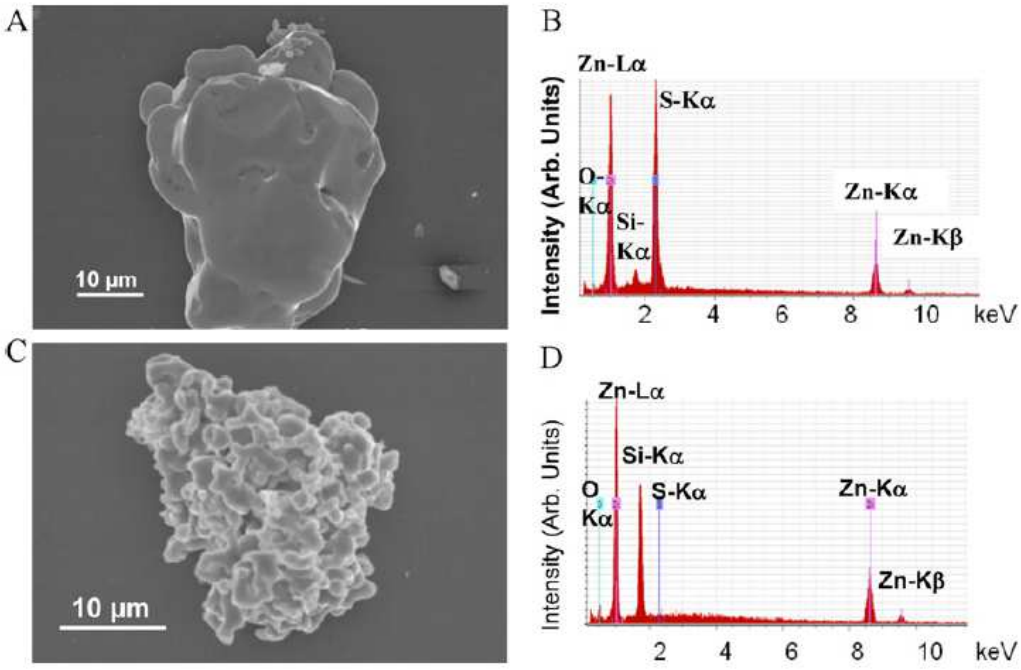

Fig II.11: *(a) and (c) SEM images of the ZnS and ZnO grains embedded in PMMA spread on a silicon wafer. (b) and (d) EDX analysis of the grain shown in (a), (c) respectively. Energy of the primary beam: 15 keV.* [4]

The grains may have two morphologies (fig II.11a) and II.11c)), indicating that they are aggregates probably made of two different materials. The EDX spectrum of the grain shown in fig II.11a) exhibits characteristic peaks of Zn-Kα, -Kβ and –Lα and S-Kα at respectively 8.6keV, 9.6keV, 1keV and 2.3keV [8]. These peaks are consistent with a 48% Zn and 48% S stoichiometry, in good agreement with stoichiometric ZnS. Concerning the other morphology, characteristic peaks of Zn-Kα, -Kβ, L-α and a small O-Kα can be noticed on the EDX spectra Fig II.11d). (the O-Kα peak is located at 524eV). The Zn-Kα has a strong intensity (at 8.6keV) while the Zn-Kβ and L-α have a lower one (at respectively 9.6keV and 1keV) [8]. The stoichiometry estimation for this spectrum is 84%Zn and 16%O. The disproportion between this ratio and the 1:1 expected stoichiometry of ZnO is due to the strong absorption probability of the O-Kα line by ZnO before to escape. Indeed, the attenuation length of O-Kα ray in ZnO is ~0.3 µm compared to that of S-Kα in ZnS which is ~2µm [9]. We can deduce that the S fluorescence comes from volume while O fluorescence mainly comes from the surface grain. The silicon substrate appears in both EDX spectra with the Si-Kα peak at 1.74 keV.

Finally we can conclude that the sample is composed of 2.5-35µm wide isolated grains made of either mainly ZnS or ZnO with different morphologies, embedded in PMMA and deposited on silicon.

A photoluminescence spectrum of the sample was then recorded in far-field mode with a 400µm core diameter optical fibre at about 10mm from the sample (The 150 grooves/mm grating is used in the spectrophotometer with a 10µm PM slit). This spectrum is shown fig.II.12.

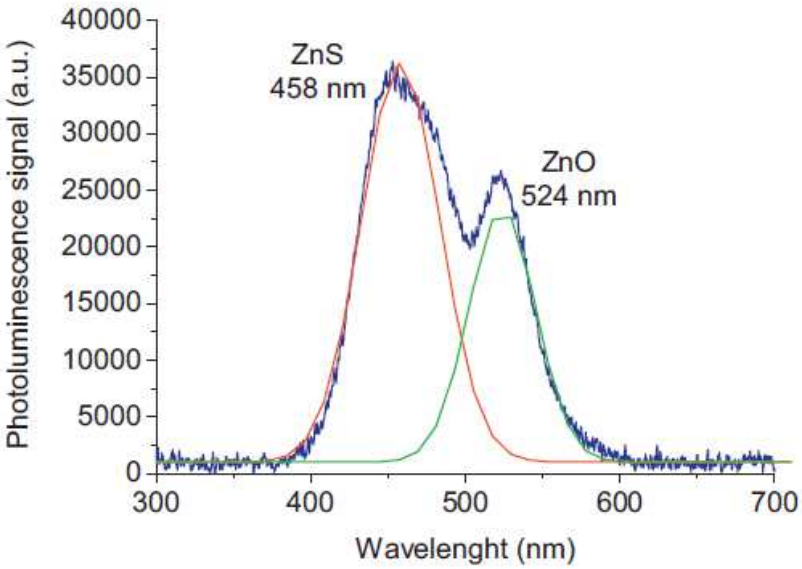

Fig II.12: *Luminescence spectrum of ZnO/ZnS clusters on Si sample. The acquisition is carried out in the far field mode using a wide core (400 µm) optical fibre.* [4]

The spectrum can be fitted by two Gaussian curves centered at 458 and 524nm, corresponding to the defect peaks of ZnS [10] and ZnO [11, 12] respectively. The excitonic peaks of ZnS (at around 323-353nm) [13] and ZnO (380nm) [14] are out of the fibre bandwidth and cannot be detected.

Topographic and simultaneous luminescence collection were then recorded with our SNOM microscope under X-ray illumination with the Rh-target X-ray source. Images are shown in Fig.II.13.

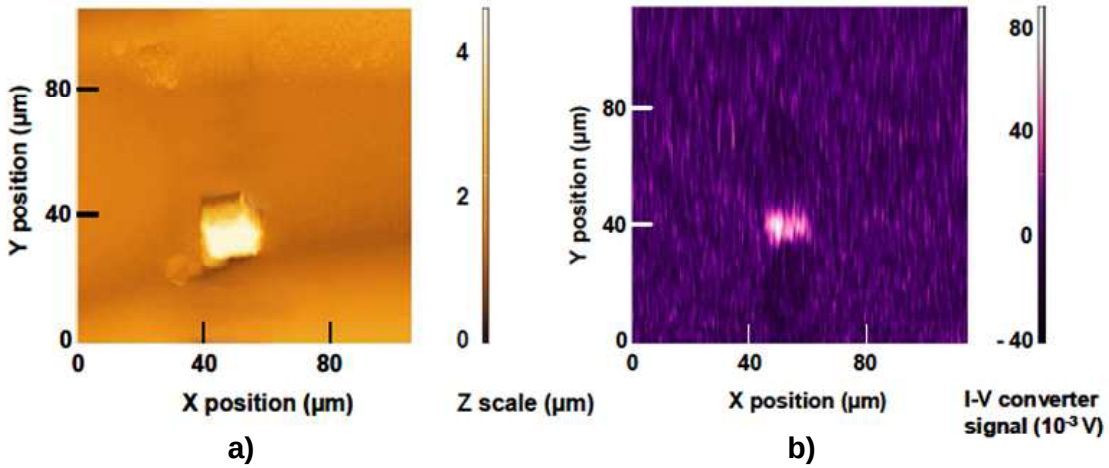

Fig II.13: *ZnS/ZnO sample imaging using our Shear Force Microscope head. Scan window 115µm×115µm. (a) Topographic image (b) and simultaneous luminescence mapping. The spectrometer was centred at 524 nm, wavelength corresponding to the defect peak of ZnO.* [4]

The image is 115µm x 115µm. The topographic image (fig II.13a)) exhibits an about 20µm diameter grain in the middle of the figure which has a height in the range of the maximum Z-piezo elongation. This explains the saturation phenomenon in the colour level over the grain.

Concerning the luminescence map (fig II.11b)), the spectrophotometer is centred at 524nm (ZnO defect peak wavelength). This mapping is recorded simultaneously to the topography. We can see that the luminescence comes mainly from the aggregate centre. Moreover, no significant luminescence signal centred at 458 nm and characteristic of ZnS defects could be recorded on the same scanned area (not shown here). This indicates that mainly ZnO emitting centers are responsible for luminescence in this scanned area, and that the wide grain shown in Fig.II.13a) is mainly composed of ZnO in the first microns of the surface [11, 12].

The grain looks smaller in the luminescence map than in the topographic image. It can be explained by a luminescence emission out of the optical fibre apex acceptance as highlightened in section II.2.2 (see fig. II.7).

II.3: Conclusion

A shear-force head was developed to acquire simultaneously the sample topography and the luminescence mapping of a sample at high lateral resolution. In a preceeding thesis this equipment was first fitted to a synchrotron beamline (ID03@ESRF) within the framework of a European project. Luminescence mapping of a ZnO-$ZnWO_4$ sample was performed. Post-acquisition image processing allowed to get a map of ZnO and $ZnWO_4$ grains at the sample surface.

Keeping the Shear Force Microscope in a fixed position and in near field interaction with the surface, local XAS-XEOL analysis was possible on a ZnO sample. The spectra exhibits EXAFS oscillations over the ZnO absorption edge with a periodicity in perfect agreement with spectra recorded in conventional far field acquisition mode. Lateral resolution of 70nm is achieved for topography and luminescence in synchrotron environment.

During my thesis, we have then fitted a laboratory Rh-target X-ray microsource equipped with a polycapilalry lens providing a high photon flux over a spot of 22 µm radius measured at 1/e. The apparatus was tested on Uranyl fluorescent screen, particularly friendly-use sample due to its high luminescence under X-ray illumination. A spectrum was first recorded as a reference using a conventional cleaved wide core optical fibre to collect the

luminescence. Then keeping the microscope tip in a fixed position another spectrum was recorded. Both far-field and near-field spectra are in good agreement. The slight difference between their peak height can be explain by the fact that in far field collection the signal is averaged on a wide surface while concerning the near-field the tip is positioned above a single specific grain that is analysed. A simultaneous topography and luminescence mapping acquisition validated the concept.

ZnO / ZnS powder mixture embedded in PMMA resist was then spin coated on a silicon sample. These samples present grains of ZnO , ZnS or aggregates of both materials. The sample was characterized by SEM-EDX and using our apparatus. It was possible to select a micro grain on the surface and to define its chemical composition.

References

[1] S. Larcheri, “Joint use of x-ray synchrotron radiation microbeams and tip-assisted photon detection for nano-scale XAFS spectroscopy and chemically sensitive surface mapping”, Università Degli Studi di Trento, Italia, 2007, thesis

[2] C. Fauquet, M. Dehlinger, F. Jandard, S. Ferrero, D. Pailharey, S. Larcheri, R. Graziola, J. Purans, A. Bjeoumikhov, A. Erko, I. Zizak, B. Dahmani and D. Tonneau, “Combining scanning probe microscopy and X-ray spectroscopy”, Nanoscale research letters, 6, 308, 2011

[3] M. Dehlinger, C. Dorczynski, C. Fauquet, F. Jandard and D. Tonneau, “Feasibility of simultaneous surface topography and XRF mapping using Shear Force Microscopy”, Int. J. Nanotechnol. Vol 9, Nos. 3-7, 460- 470, 2012

[4] F. Jandard, C. Fauquet, M. Dehlinger, A. Ranguis, A. Bjeoumikhov, S. Ferrero, D. Pailharey, B. Dahmani and D. Tonneau, “Mapping of X-ray induced luminescence using a SNOM probe”, Applied Surface Science 267, 81-85, 2013

[5] Z. Hnatejko, S. Lis, Z. Stryla, “Preparation and characterization of uranyl complexes with phosphonate ligands”, J. Therm. Anal. Calorim. 100, 253–260, 2010

[6] V.V. Syt’ko, N.A. Aleshkevich, E.L. Tikhova, D.S. Umreiko, I.A. Khartonik, “Electron spectra of $Me_7Eu_2UO_2(PO_4)^5$ crystals”, J. Appl. Spectrosc. 66, 94–99, 1999

[7] L.R. Wilson, B.Sc., “Luminescent Solar Concentrators: A Study of Optical Properties, Re-absorption and Device Optimisation”, Ph.D. Thesis, Department of Mechanical Engineering, School of Engineering and mechanical Sciences, Heriot-Watt University, Edinburgh, United Kingdom, May 2010.

[8] See for example: X-Ray Data Booklet, Center for X-ray Optics and Advanced Light Source, Lawrence Berkeley National Laboratory, 2009, http://xdb.lbl.gov/ (last accessed 18/07/2013).

[9] See for example http://henke.lbl.gov/optical_constants/atten2.html , (last accessed 18/07/2013).

[10] J.C. Lee, D.H. Park, “Self-defects properties of ZnS with sintering temperature”, Mater. Lett. 57, 2872–2878, 2003

[11] X.L. Wu, G.G. Siu, C.L. Fu, H.C. Ong, “Photoluminescence and cathodoluminescence studies of stoichiometric and oxygen-deficient ZnO films”, Appl. Phys. Lett. 78, 2285–2287, 2001

[12] K. Vanheusden, W.L. Warren, C.H. Seager, D.R. Tallant, J.A. Voigt, B.E. Gnade, “Mechanisms behind green photoluminescence in ZnO phosphor powders”, J. Appl. Phys. 79, 7983–7989, 1996

[13] M.Y. Nadeem, W. Ahmed, “Optical properties of ZnS thin films”, Turk. J. Phys. 24, 651–659, 2000

[14] U. Ozgür, Ya.I. Alivov, C. Liu, A. Teke, M.A. Reshchikov, S. Dogan, V. Avrutin, S.-J. Cho, H. Morkoc, “A comprehensive review of ZnO materials and devices”, J. Appl. Phys. 98, 041301, 2005

CHAPTER III Toward X-Ray Fluorescence spectroscopy and mapping with a sub-micrometer resolution using a laboratory source

Chemical analysis by XEOL or by luminescence spectroscopy is mainly limited to semiconducting materials. To extend X-ray characterization to a wider variety of materials, XRF analysis is a powerful technique. Indeed it allows a high sensitivity and non destructive elemental in-depth analysis. Moreover, the technique is not sensitive to sample carbon contamination due to ambient exposure because the attenuation length x_C of X-rays in carbon is very high (x_C = 15 and 2066 µm at respectively 2 and 10 keV). The lateral resolution of the technique is limited by the primary beam probe diameter. At synchrotron beamlines, the beam probe area is currently a few µm². To increase the lateral resolution of the technique the trend is to decrease the beam probe diameter down to some tens of nanometers, as can be delivered for example by APS [1].

Recent breakthroughs in X-ray focusing optics allow now to obtain a high brightness X-spot using a laboratory source. As a consequence, we currently find on the market XRF analysers offering lateral resolution down to 5 µm [2].

Two ways are possible to improve the resolution. First the beam size probe can be decreased using for example Fresnel zone plates or Kirk-Patrick Baez mirror systems. However, these technologies are very expensive. Furthermore, because of the high flux lost through X-ray focusing optics it is necessary to increase as much as possible the detector aperture to keep a significant signal to noise ratio. This is the general trend in the XRF community. However, it remains impossible to align the sample regarding the primary beam spot to analyze a peculiar zone of the surface or a peculiar nano-object.

The second solution is to keep a micronscale excitation beam probe and simultaneously to shrink down as much as possible the detector aperture, using for example a pinhole. In this case, the detector must be approached as much as possible from the sample to maintain a significant fluorescence signal to noise ratio because the measured signal varies as the reciprocal square detector-sample distance. However, the detector steric hindrance impedes to approach at the vicinity of the surface because of primary beam shadowing effects. Cylindrical X-ray capillaries can be used almost as X-ray guides (see Chapter I section I.4.1). Our first idea was thus to equip the detector with a thin cylindrical monocapillary that could be approached at sub-millimetre distance from the sample surface avoiding thus primary

beam shadowing. In this case, the X-ray fluorescence emitted by the sample can be collected by the capillary aperture and transmitted by multiple reflections at grazing angle to the detector. Of course the brighter is the excitation source, the more the capillary aperture can be shrunken, keeping a significant XRF signal to noise ratio. The remaining issue is the estimation of the lateral resolution that could be reached using a focused laboratory X-ray sources for excitation. We have thus developed a test-bed based on capillary optics on both primary illumination and XRF detection optical paths, as presented in the following. With this experimental setup we have then studied the influence of capillary diameter and working distance on the collected signal magnitude. Finally, we have used this test-bed to highlight the convolution problem inherent to all probing systems.

III.1. Experimental test-bed

III.1.1: Experimental Setup

The experimental setup is shown in Fig.III.1. An X-ray beam provided by a low power Rh-target source operating at 35 kV and 800 µA is focused on a sample using a 7 mm focal distance polycapillary lens [3, 4]. The beam incidence angle is 30°.

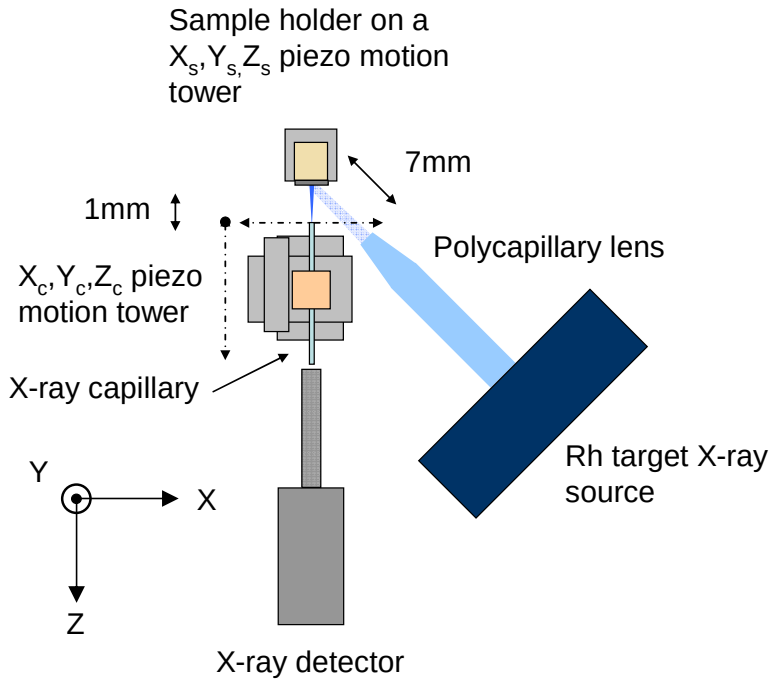

Fig. III.1: *Experimental test-bed. The sample is placed in the focal plane of the polycapillary lens (7 mm). The distance between the sample and the cylindrical capillary extremity is 1 mm.*

The source spectrum (figure III.2) exhibits a wide Bremsstrahlung radiation, narrow Rh-Kα, Rh-Kβı and Rh-$K\beta_2$ lines at 20.216, 22.074 and 22.724 keV respectively and X-rays from the L shell excitation at 2.697 ($L\alpha_1$), 2.692 ($L\alpha_2$), 2.834($L\beta_1$), 3.001($L\beta_2$) and 3.144 keV ($L\gamma_1$). Bremsstrahlung, Kα, Kβ and sum of X-ray radiation from the L-edge are respectively 56.23, 2.67, 0.62 and 40.48% of the total photon flux at 35 kV electron acceleration voltage using a rhodium target [5]. The source spectra on fig III.2 were acquired at 35 kV, 100 µA (in green) and 35 kV, 800 µA (in red) by shrinking the detector input using a 5 µm diameter lead pinhole in order to avoid detector saturation.

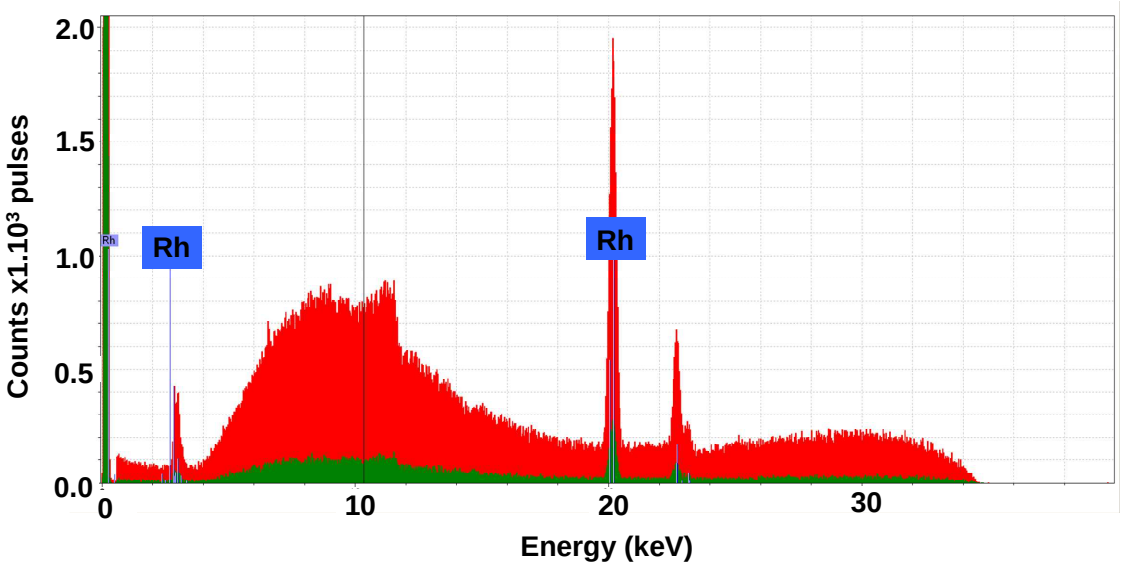

Fig III.2: *Spectra of a Rh target microsource at 35 kV x 100 µA (green) and 35kV x 800µA (red). Courtesy S. Bjeoumikhova (IFG-GmbH). Acquisition time: 100s*

The sample fluorescence is analysed by a SDD (Silicon Drift Detector, Brüker GmbH, surface 10mm²) EDX (Energy Dispersive X-ray) detector through a 50 mm long and 1 mm outer diameter cylindrical X-ray capillary. Capillaries with 5, 10, 25 or 50 µm inner radii were tested. The cylindrical capillary is placed on X_c, Y_c, Z_c piezo-stages allowing displacements with 30 nm step size while the detector remains in a fixed position. The capillary extremity to sample distance (i.e. the working distance WD) is fixed at 1 mm for all experiments. This parameter is kept constant during capillary replacement procedure. 1 mm is a high enough WD to avoid primary beam shadowing effects by the capillary extremity. The choice of this WD is justified later in section III.2.2. The WD value is controlled by placing the capillary in contact with the surface and by withdrawing using the Z_c-motion. A cobalt sample, exhibiting a significant X-ray fluorescence yield under the Rh source excitation, is used to measure the

fluorescence signal magnitude collected through the various cylindrical capillaries. It is positioned on a X_s, Y_s, Z_s piezo-stages.

III.1.2: Primary beam spot characterization

The primary beam spot has been characterized. First, a pindiode detector is positioned perpendicularly to the X-ray propagation direction at a distance of 5 cm behind the polycapillary lens focal plane. Figure III.3 shows the primary beam intensity detected by the pin diode as a function of the source current. The photon flux is clearly proportional to the current within the range investigated.

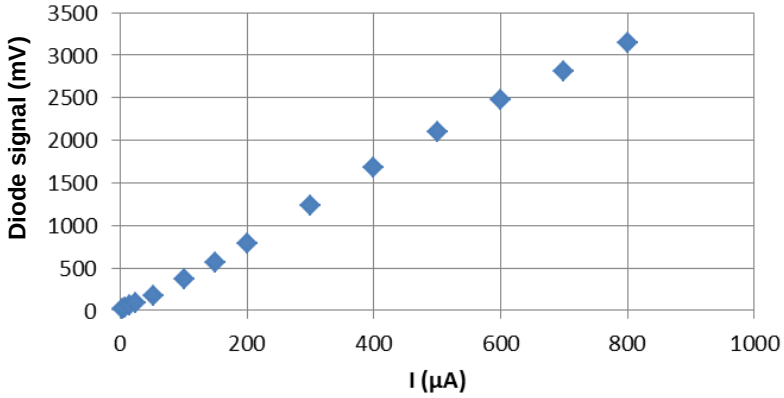

Fig III.3: Pin d*iode signal (proportional to the X-ray photon flux) variation as a function of the source current. The acceleration voltage is 35 kV.*

We have then also characterized the primary beam lateral profile. For that purpose, the detector is positioned in direct view of the primary beam. The detector entry is shrunk down using a 5µm diameter lead pinhole placed on the X_c, Y_c, Z_c piezo stages. The pinhole plane is positioned in the polycapillary lens focal plane and is displaced by steps of 2.6µm (=100 piezo motion steps) along the beam spot diameter (see fig III.4). For each pinhole position, a primary beam spectrum is acquired. To perform these measurements the source current has been decreased down to **1** µA to avoid detector saturation and damage. We have divided each spectrum into sections of 2keV range. The signal magnitude within each section has been reported to a new graph as a function of the pinhole centre position (Fig III.5).

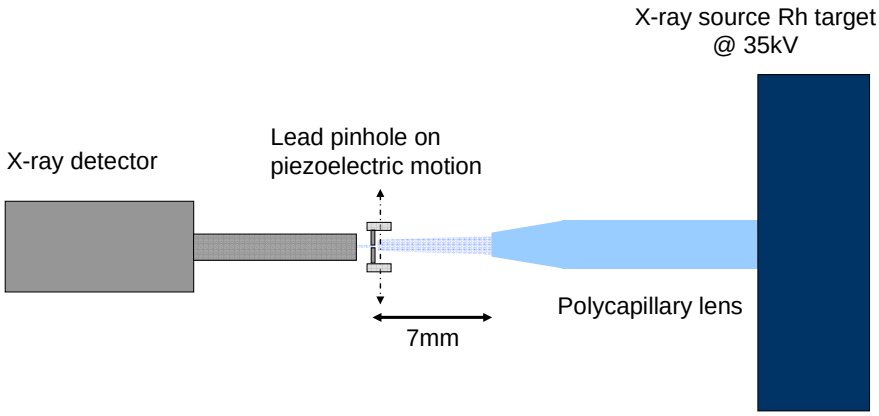

Fig.III.4 : *Experimental setup configuration for X-ray primary spot characterization.*

Fig.III.5 shows the X-ray photon flux variations with the pinhole centre position at the various incident energy ranges provided by the source. Because of the linearity of the photon flux with current (as shown in Fig III.3), the scale is multiplied by a factor 800 to remain consistent with the usual experimental conditions (35kV, 800µA).

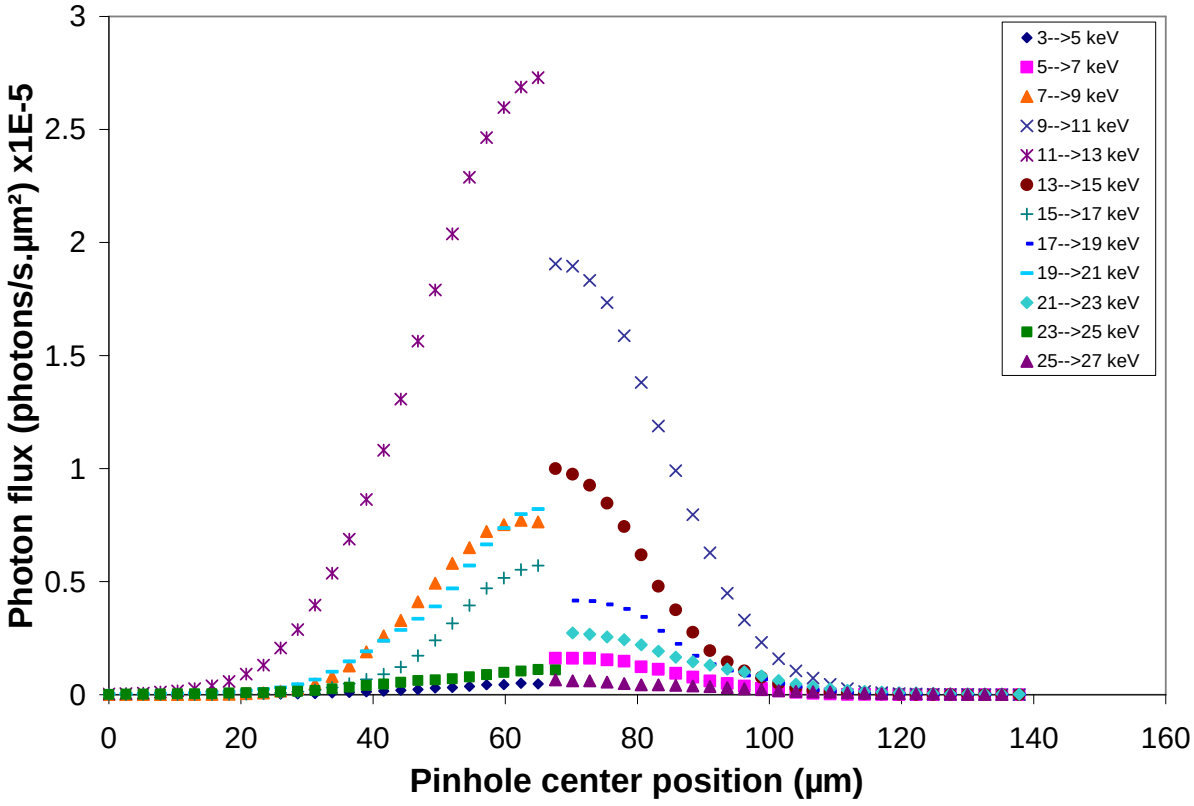

Fig.III.5: *X-ray primary beam lateral profile within the polycapillary lens focal plane. For the measurements, the source was tuned at 35 keV, 1 µA. The photon flux axis is rescaled to fit with nominal working conditions used in the following (35 keV, 800 µA).*

As can be seen in figure III.5, the incident spot lateral profile has a Gaussian shape and the FWHM as well as the maximum flux depends on the photon energy. The lens providing the spot consists in a monolithic system made of a great number of thin monocapillary micrometric glass tubes bent together [6]. The total external reflection critical angle of glass varies with the source energy E in agreement with the following equation:

$$\theta_c(rad) = \frac{0.02\sqrt{\rho(g.cm)^{-3}}}{E(keV)} \qquad \text{Eq (III.1) [7]}$$

where ρ is the glass capillary density and E the photon energy. Because X-rays are guided by total external reflections on the capillary wall, it does exist a slight beam divergence at each channel exit depending on θ_c. Because the Rh low power source is not monochromatized, the radius of the spot delivered by the polycapillary lens depends on the photon energy range as can be seen in Fig. III.5. From these experimental data, the average half-width measured at 1/e is 22 µm and the photon flux within this spot area is about $1.7.10^9$ photons.s^{-1}.μm^{-2}. This flux is obtained by adding all photon flux presented in fig. III.5.

III. 2 : XRF spectroscopy using the experimental test-bed

III.2.1: Lateral profile of the fluorescence emitting volume

III.2.1.1 Alignment procedure

The geometry of the fluorescence emitting volume in the cobalt sample was defined using the XRF configuration shown in Fig.III.1 by scanning the cylindrical capillary used for detection across the X-ray fluorescence emitting zone of the cobalt sample. First it was necessary to align the capillary extremity with the incident focused spot centre. For this step, a luminescent screen is stuck on the sample holder, just below the cobalt sample. The X-ray spot position on the fluorescent screen and the capillary extremity can be observed on a video monitor, using a zoom-CCD camera system. It is then possible to perform the coarse alignment between the capillary aperture and the X-ray beam spot centre with a few micrometers accuracy. Then, the capillary is positioned at 1 mm WD using the Z_c motion. The sample is moved vertically using the Y_s motion actuator to position the primary spot on the

cobalt sample. Fine alignment between spot centre and capillary aperture is finally performed using the EDX detector to search for the maximum CoK_α signal when the capillary is slightly displaced in a plane parallel to the sample surface. This alignment step must be repeated every time we change the capillary used for detection. After alignment, the capillary is displaced across the fluorescence spot zone, parallel to the surface plane acting on X_c axis.

III.2.1.2: XRF volume profile - Evidence of capillary aperture-XRF volume convolution effects

At each cylindrical capillary position across the fluorescence area diameter, an X-ray spectrum is acquired that exhibits the two characteristic Co-K_α and Co-K_β lines at 6.9 and 7.6 keV respectively (figure III.6).

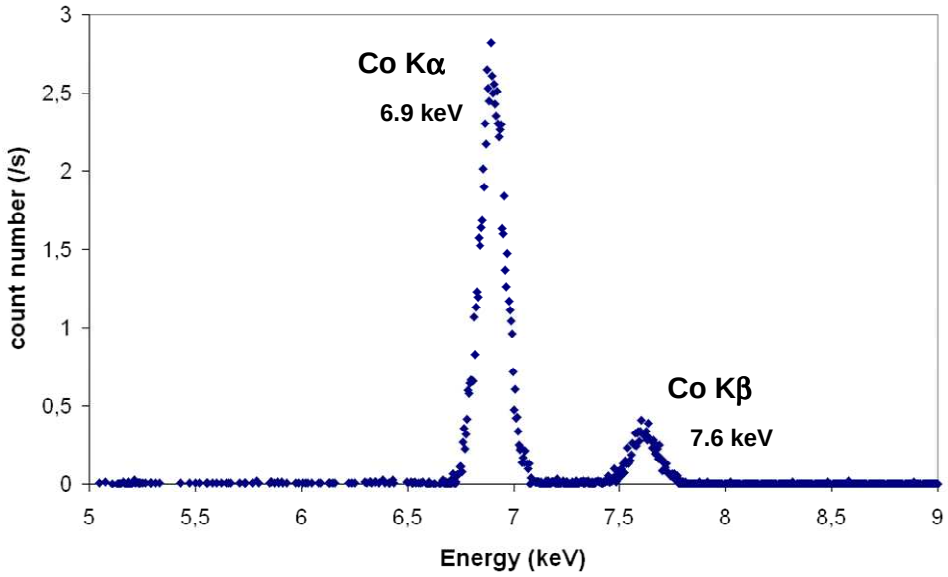

Fig. III.6: *Typical XRF spectrum recorded across the fluorescence emitting zone. The cylindrical capillary diameter is 20µm.*

Energies and ratios between K_α and K_β peaks are in good agreement with literature data [8]. We then reported in Fig. III.7 the Kα peak area measured for each capillary position using various capillary radii from 5 to 50 µm. All the curves exhibit identical shape which is not expected to be Gaussian. Indeed the primary Gaussian beam is not sent perpendicular to

the sample but with an incident angle of 30°. Furthermore, the lateral profile diameter is from far different from the primary X-ray spot diameter and depends on the capillary radius.

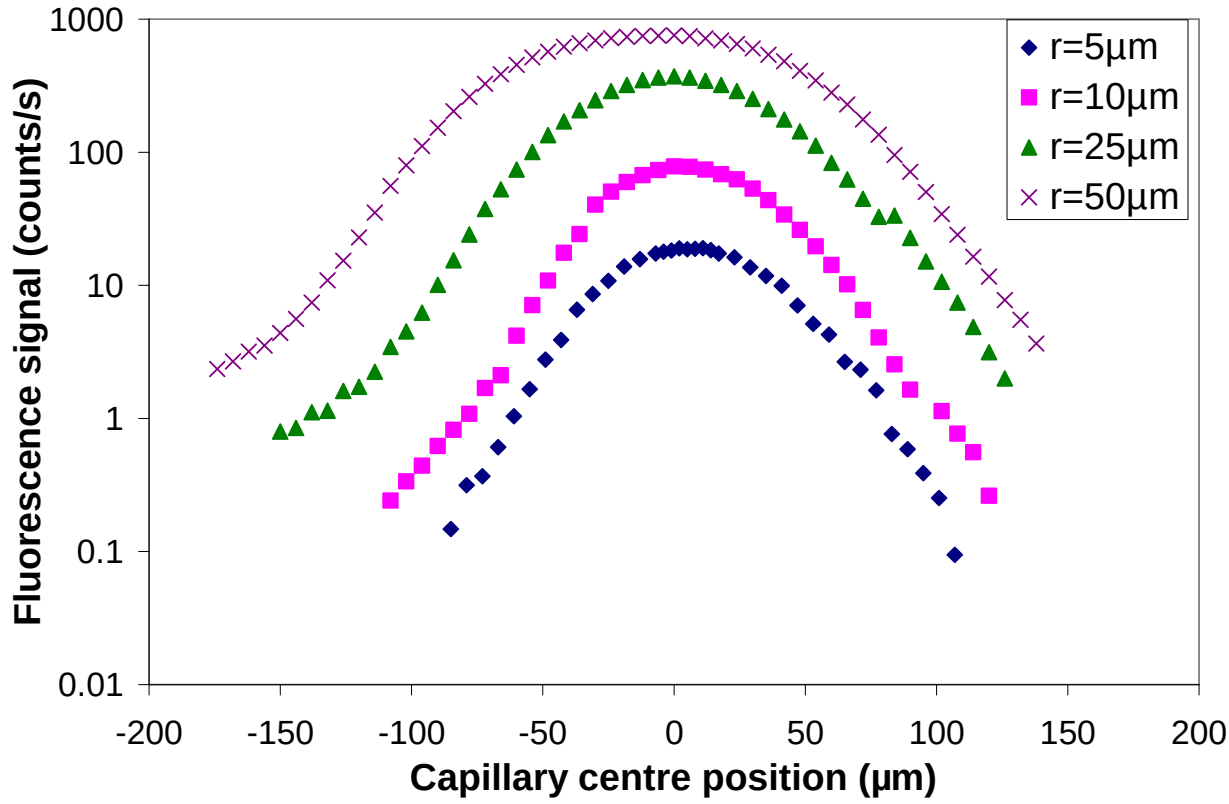

Fig.III.7: *Cobalt fluorescence zone lateral profile represented by the Kα peak area as a function of the detection capillary position. The capillary radii are 5, 10, 25µm and 50 µm.*

The primary beam penetrates inside the sample with an attenuation length $x_{Rh\text{-}K\alpha/Co}$ = 43 µm [9], inducing X-ray fluorescence, itself reabsorbed and leading to secondary emission. However, the fluorescence emitted within this deep volume cannot be entirely detected since the attenuation length of Co-K_α rays in Co ($x_{Co\text{-}K\alpha/Co}$ = 18 µm [9]) is shorter than the penetration depth of Rh-K_α rays in Co. This means that the collected fluorescence comes from a deep excited volume schematically shown in Fig.III.8. From simple geometrical considerations and neglecting the secondary emission, we expect to detect a signal over a capillary travel Φ_a given by:

$$\Phi a = 2\ WD\ \tan(\theta_c) + 2\ r_{spot} / \sin(30°) + x_{Co\text{-}K\alpha/Co} \cot(30°) + 2\ r_{cap} \qquad \text{Eq (III.2)}$$

where r_{spot} is the primary spot half width measured at 1/e, r_{cap} the capillary radius and WD the detection capillary working distance. However, as can be seen in Fig. III.8, the fluorescence magnitude collected from point A, located at the cobalt sample surface, is obviously different from that collected from in-depth point B. This is due to the absorption of the primary beam before reaching B point and to strong cobalt X-ray fluorescence reabsorption in the path through the sample. Thus, in order to compare the theoretical and experimental values of Φ_a, we must consider this discrepancy. Taking into account the actual value of the primary beam flux F_{max}/e at r_{spot} from the spot centre (see Fig. III.7), the fluorescence maximum flux F(B) escaping from the sample emitted at a depth of $x_{Co\text{-}K\alpha/Co}$ = 18 µm (point B), should be given by:

$$F(B) = F_{max}\, \tau / e^2 \exp(-d / x_{Rh\text{-}K\alpha/Co}) \qquad \text{Eq (III.3)}$$

Where d is the path length of the primary beam in Co till a depth of $x_{Co\text{-}K\alpha/Co}$ and τ is the excitation factor of Cobalt. With the value of $\tau = 0.33$ taken from Ref [9] the value of F(B) is expected to be about 0.02 Fmax. From this, we arbitrary choose the significant fluorescence flux above 0.02 F_{max} to define the capillary travel Φa along which fluorescence was detected from the sample surface. Point A' must thus be chosen instead of point A, to fit with this condition:

$$F(A') = F_{max} \exp-(r_{A'}{}^2 / r_{spot}{}^2)\, \tau = 0.02\, F_{max} \qquad \text{Eq (III.4)}$$

Consequently point A' in Fig.III.8 is positioned at a distance $r_{A'} = 1.7\, r_{spot}$ from the beam centre. To compare the expected and measured values of Φ_a, we have thus replaced 2 r_{spot} in equation (III.2) by distance A'B = 1.7 r_{spot} + r_{spot}. With these considerations, Φ_a values of 258, 208, 178 and 168 µm are expected for a capillary radius of 50, 25, 10 and 5 µm respectively. These values are in good agreement with the experimental values of Φ_a = 240, 205, 172 and 168 µm.

In this model, we set the photon energy at 20.2 keV (Rh Kα). Nonetheless, we should mention that with our micro-source, the main photon flux comes from the wide Bremsstrahlung spectrum (see section III.1.2). We have also seen in the same section that the incident beam diameter provided by the lens in the focal plane is maximum at high energy. The goal of the present section was to estimate the maximum lateral extension of the fluorescence volume in the cobalt sample. That is the reason why we have selected the widest

incident beam with a significant photon flux for our calculations i.e. the Rh-Kα line at 20.2 keV.

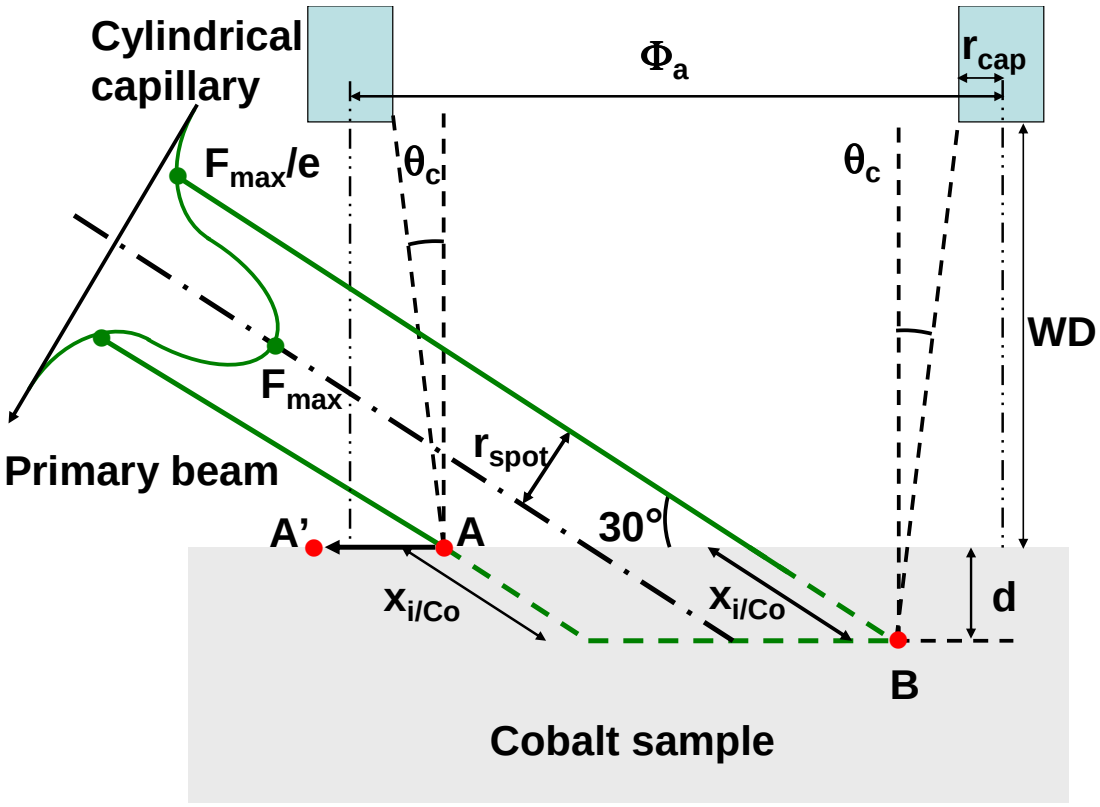

Fig.III.8: *Sample excited volume geometry and ϕ_a estimation procedure.*

III.2.2 Maximum flux detected with the experimental test-bed

We have then reported in Fig. III.9 the maximum flux collected at the centre of the fluorescent zone as a function of capillary radius for a constant WD of 1 mm. The data dealing with 5, 10, 25 and 50 µm radius capillaries correspond to the maxima measured in fig.III.6. The maximum collected flux increases as $r_{cap}^{1.8}$.

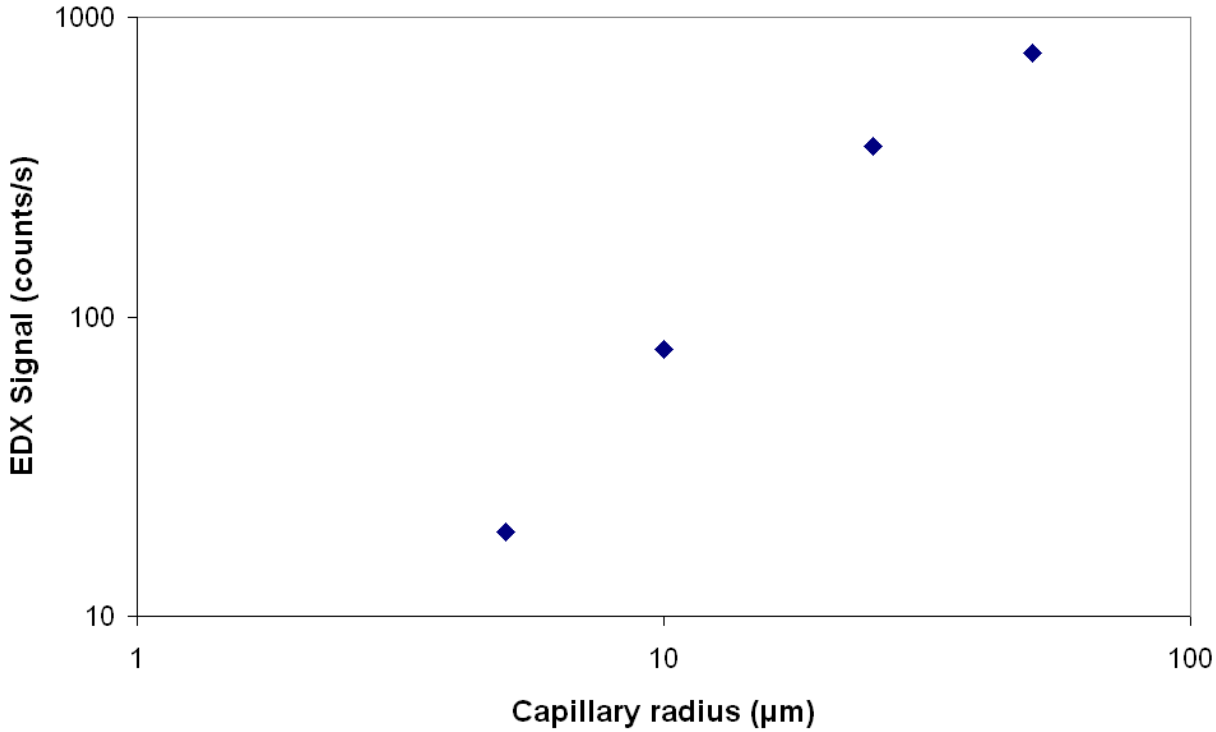

Fig.III.9: *Dependence of the maximum fluorescence flux collected during capillary scan as a function of the capillary radius.*

This variation has to be compared to the ideal case of fluorescence collection from a point source using a thin capillary of length L placed at a working distance WD from the emitter. Fig. III.10 clearly shows that the collected signal level should remain constant if the capillary radius is reduced, providing the WD is reduced by the same factor by increasing the capillary length and assuming an ideal transmission coefficient of 100%. Obviously, in our case, the capillary only collects a part of fluorescence, nearly proportional to its section. The observed variations of the signal magnitude with the capillary radius are due to the fact that the fluorescent zone has dimensions higher or of the same order of magnitude than the capillary radius. Assuming a uniform lateral profile extended primary beam, the signal should vary as r_{cap}^2 at low capillary radius. This variation is in good agreement with the $r_{cap}^{1.8}$ variation calculated from Fig. III.9. The slight discrepancy is due to the profile that is not squared but Gaussian.

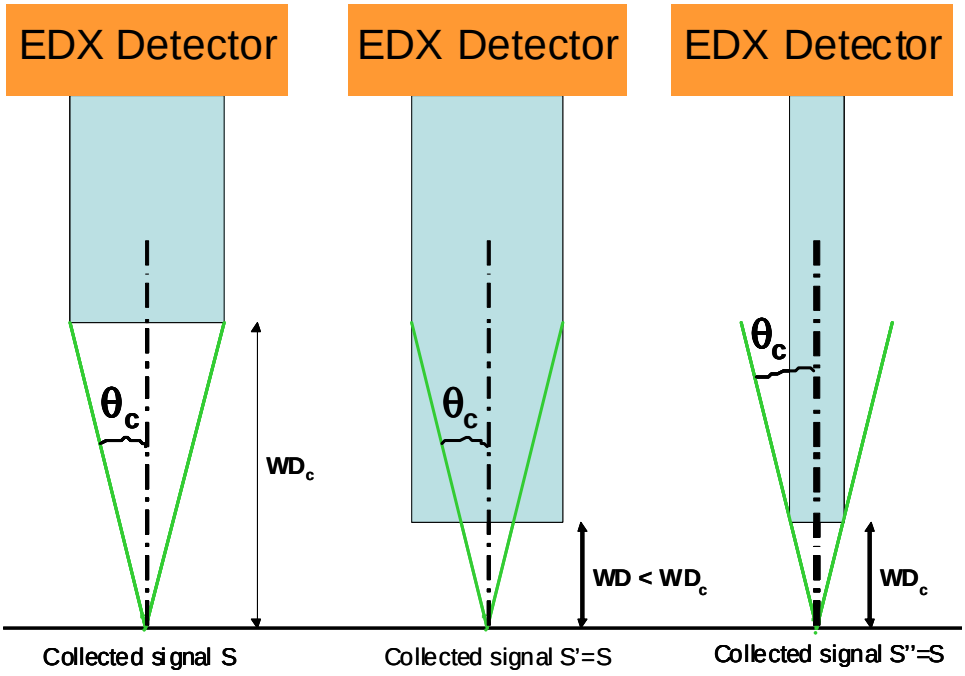

Fig.III.10: *fluorescence signal collection through a capillary. The signal collected is independent of the capillary diameter providing the working distance WD is shorter or equal to the critical one WD_c.*

Would it be possible to increase this signal by decreasing WD?

It is well known that cylindrical capillaries allow to significantly increase the collected signal by comparison with a pinhole with the same radius placed at the detector entry and positioned at the same $WD+L_{cap}$ distance. This is illustrated in (Fig.III.11a) and III.11b)) in the case of a punctual source [6]. At high WD, the capillary aperture is seen under a solid angle $\theta_1 < \theta_c$ from the point source (Fig. III.11 b)). Thus all X-rays emitted by the point source within this solid angle will be transmitted through the capillary, assuming a total reflection of X-rays below the critical angle. The capillary gain G regarding a pinhole of the same radius is given by the equation:

$$G \approx [\ \theta_1 (WD + L_{cap}) / r_{cap}\ ]^2 \qquad \text{Eq (III.5) [6]}$$

If WD decreases, keeping $WD + L_{cap}$ constant, the collected signal magnitude first increases since the collection solid angle increases until it reaches $\theta_2 = \theta_c$ value. At this point (Fig.III.10 c)) WD reaches a WD_c value given by:

$$WD_c = r_{cap} / \tan(\theta_c) \approx r_{cap} / \theta_c \qquad \text{Eq (III.6)}$$

In this case, the capillary gain is given by:

$$G = [\, \theta_c \, (WD_c + L_c) / r_{cap} \,]^2 = [\, 1 + \theta_c \; L_c / r_{cap} \,]^2 \qquad \text{Eq (III.7)}$$

If WD is further decreased, the solid angle θ_3 under which the capillary aperture is seen from the point source is higher than θ_c (Fig.III.10 d)). The collected signal is no more limited by the capillary aperture: the capillary gain as well as the collected signal remains constant because θ_c is the reflection limit angle of glass. Because the WD_c value depends on the capillary radius and that from Eq (III.6) the smallest value of WD_c is 1 mm for the capillaries tested in this work, this optimum value was chosen and taken constant in all these experiments.

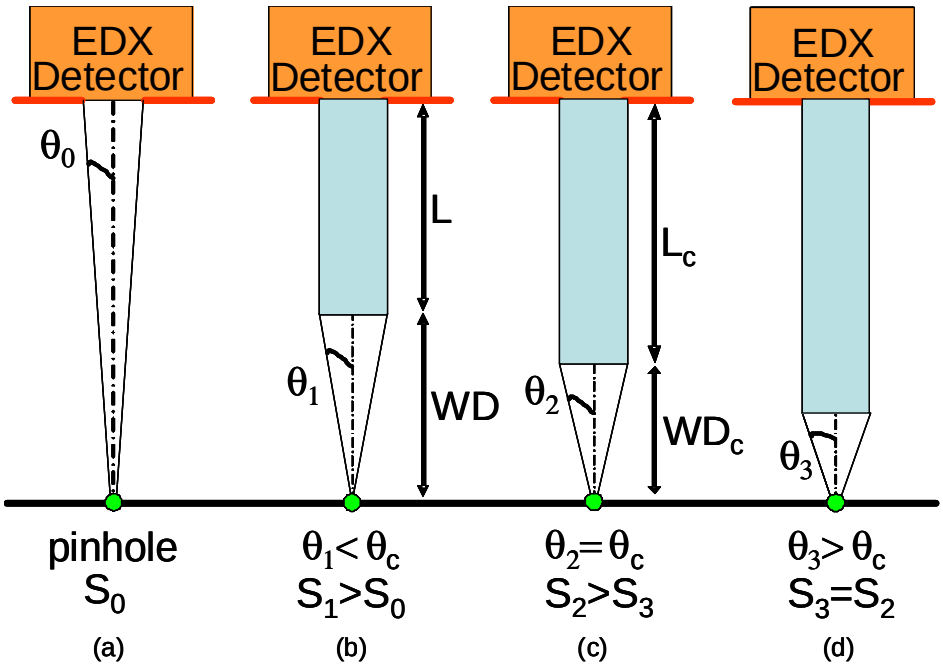

Fig. III.11: *scheme qualitatively highlighting the influence of capillary length on the collected signal magnitude in the case of a point source. The detector-sample distance is kept constant.*

The point source model tends to show that the collected XRF signal magnitude does not increase when WD is chosen lower than WD_c. However, we will see in chapter IV that the optimum geometry of XRF spectrometer using capillary optics for detection requires to approach below WD_c.

III.2.3: Micronscale pattern profiling by XRF

In this study, a micronscale test pattern is imaged by X-ray microscopy using the test-bed shown in Fig.III.1. The XRF emitted by the sample is still collected through a cylindrical capillary of radius r_{cap} = 5, 10, 25 or 100 µm positioned at a working distance WD of 1 mm. First the capillary aperture was aligned regarding the primary beam spot. Then the detection capillary as well as the X-ray source is maintained in a fixed position to keep this optimum alignment during pattern imaging process. The scan movement will be operated via the sample (X_s axis motion) within the source lens focal plane.

A first sample consisting in a molybdenum Transmission Electron Microscope (TEM) grid glued on a cobalt sample was studied. The experiment is schematically represented in Fig.III.12. The 25 µm radius capillary was used for these measurements. d_{track} is the molybdenum track width, Φ_{track} is the pattern pitch. At each 10 µm step, we record an XRF spectrum and calculate the Mo Kα (17.4 keV) peak area. We then report each value on a graph as a function of the sample position (Fig. III.13).

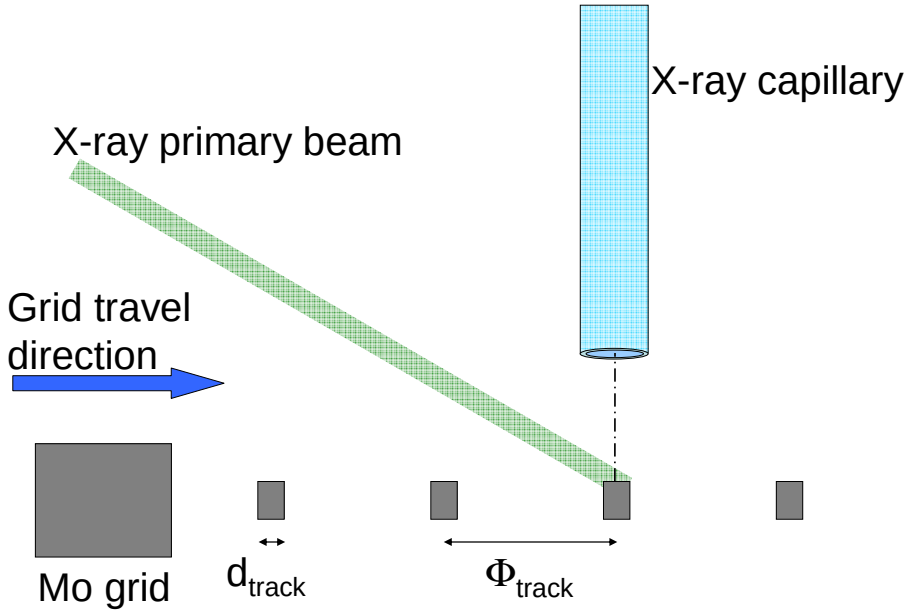

Fig III.12 : *Scheme of the experimental procedure for XRF profiling. The sample is a molybdenum Transmission Electron Micrograph (TEM) grid glued on a cobalt sample. The grid is positioned in the polycapillary lens focal plane and moved perpendicularly to the axis of the capillary used for detection (r_{cap} 25 µm).*

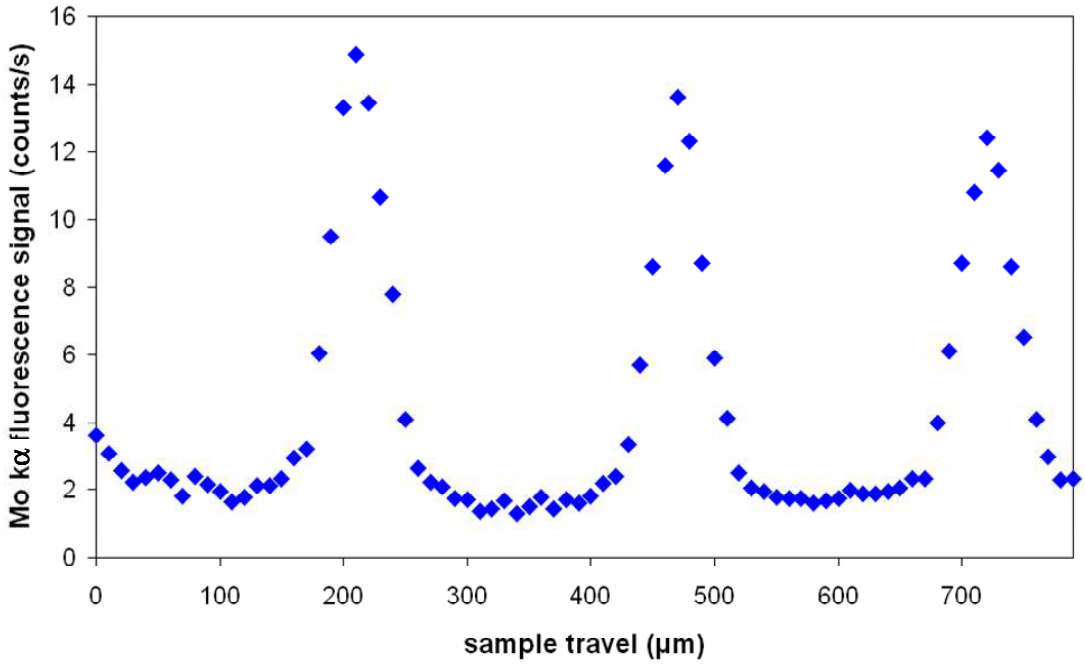

Fig.III.13 *: Mo kα signal variation as a function of sample position. The detection capillary radius is 25 µm.*

As expected, molybdenum Kα peak area variations present some oscillations that follow the grid pattern. We can deduce an average distance Φ_{track} between two consecutive tracks of 255µm in perfect agreement with optical microscope measurements (251 µm). An apparent track width d_{track} of 88 µm is measured to be compared to 36 µm obtained by optical microscopy. In fact, the use of capillaries for XRF detection induces convolution effects as mentioned in III.2.2. section. The illumination spot radius (22µm primary beam radius at 1/e) as well as the capillary diameter are of the same order of magnitude than the track width. Molybdenum collection starts (and ends) even if the capillary position is shifted regarding the track limits (see figure III.14).

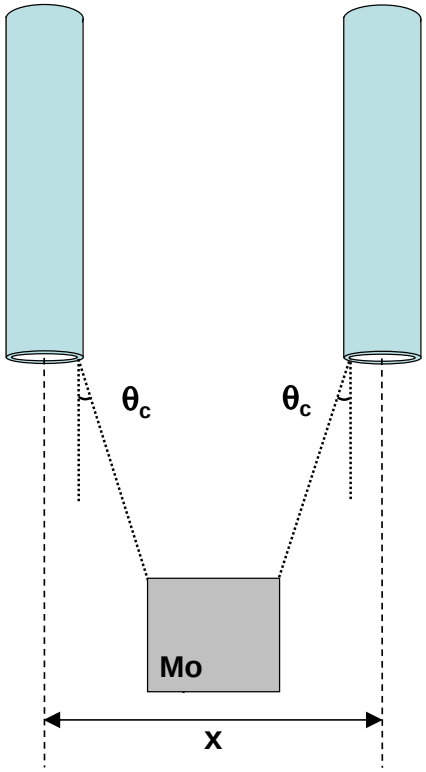

Fig.III.14: *Lateral excursion x of the capillary over which Mo signal is detected* (Eq III.8)

According to these geometric considerations, Mo should be detected over a distance x so that, in a first approximation:

$$x = 2\ rcap + 2\ WD \tan \theta_{cMo} + d_{track} \qquad \text{Eq (III.8)}$$

Where θ_{cMo} is the reflection critical angle of the MoKα line (1,70 mrad). Considering a d_{track} value of 36 µm and WD = 1 mm, a value of x = 89.4 µm is expected, in good agreement with the measurement**.**

During capillary excursion, MoKα signal varies and is maximum when the capillary axis is aligned with the Mo track centre position. Φ_{track} can thus be determined as the travel distance between two successive maxima in Fig. III.13.

In a second experiment, titanium was deposited by magnetron sputtering through the molybdenum Transmission Electron Microscope (TEM) grid. As the grid is removed, a titanium pattern remains on the cobalt sample. The titanium thickness is 600 nm. Fig III.15 shows a Scanning Electron Microscope (SEM) micrograph of the pattern as processed. It consists in wide 230 x 230 µm² titanium pads separated by 35 µm cobalt stripes, values consistent with measurements performed on the grid by optical microscopy and by XRF profiling. Using our test-bed, we followed the variation of the TiKα peak area (at 4.5 keV) as a function of the sample position. Note that the titanium layer is very thin and consequently

cobalt Kα (6,9 keV) is always detected even through a titanium pad. Indeed, the attenuation length of CoKα in Ti is about 7 µm to be compared to the titanium layer thickness (600 nm). Consequently, the variations of the Co Kα peak area are not so large than those of the Ti Kα peak area. That is the reason why we have chosen in the following to work with the Ti Kα peak area variations.

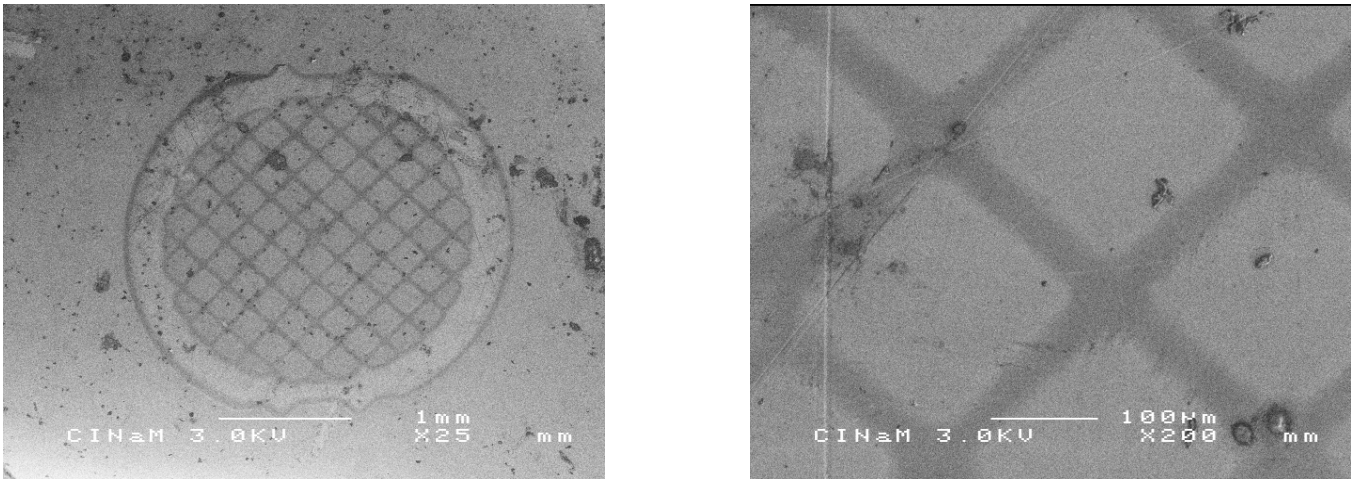

Fig.III.15: *SEM micrograph of the Ti pattern on Co.*

The experiment principle scheme is presented in Fig III.16.

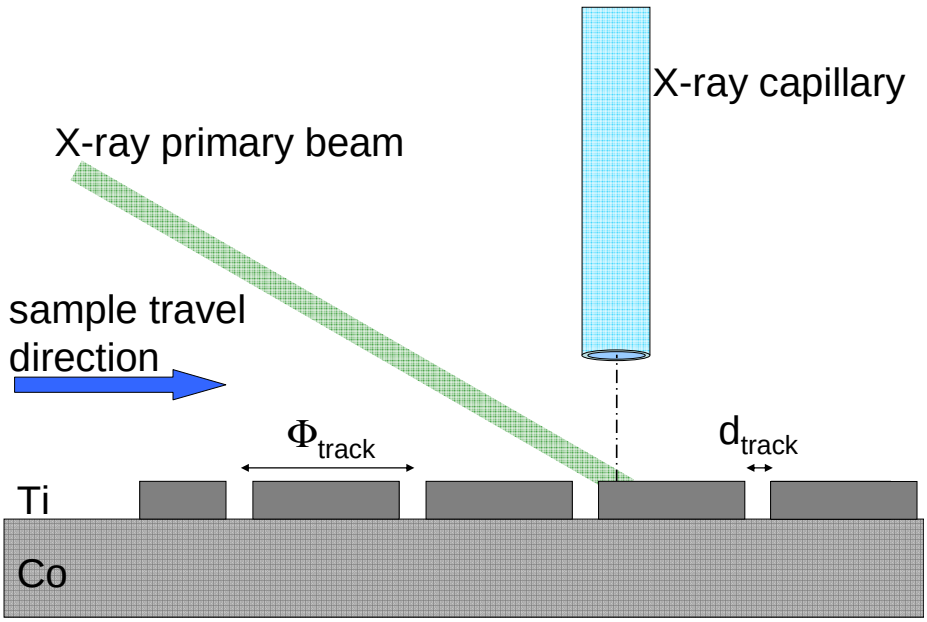

Fig III.16: *Scheme of XRF profiling of the Ti pattern deposited on Co.*

Capillaries of 25, 10 and 5µm radii were used for experiments on this sample. At each sample step (15µm), a spectrum was recorded. The spectra acquisition times are 30, 60 and 100s respectively for 25, 10 and 5µm radii. For each spectrum we reported the Ti Kα signal as a function of the sample position. The results are shown Fig III.17, 18 and 19 (blue dots).

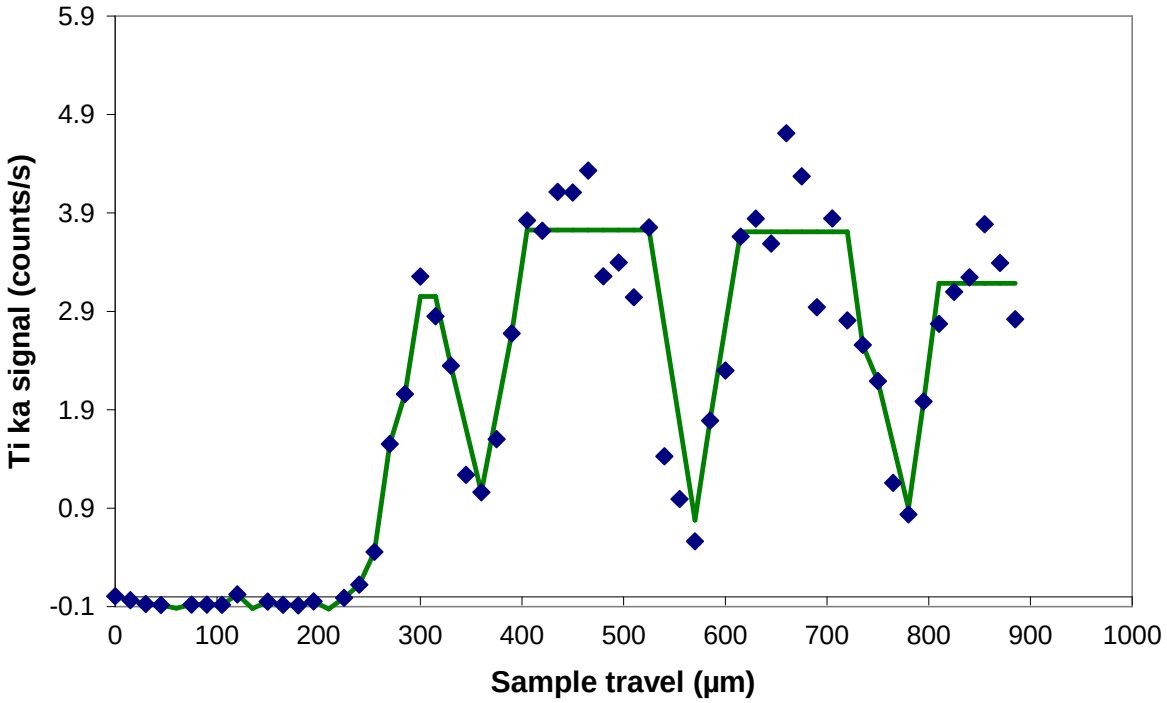

Fig.III.17: *Ti Ka signal as a function of the sample position. Blue dots are the experimental result extracted from raw data , green line is a guide line for the eyes taking into account the convolution phenomenon.* r_{cap} *= 25 µm*

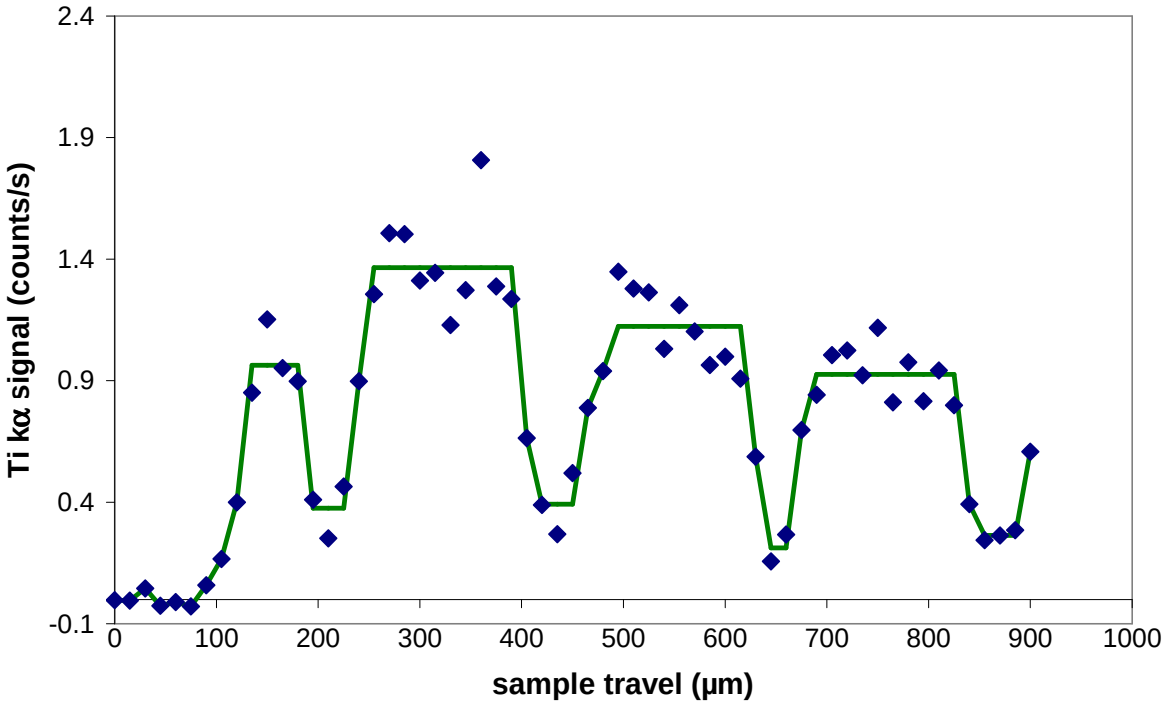

Fig.III.18: *Ti Ka signal as a function of the sample position. Blue dots are the experimental result extracted from raw data , green line is a guide line for the eyes taking into account the convolution phenomenon.* r_{cap} *= 10 µm*

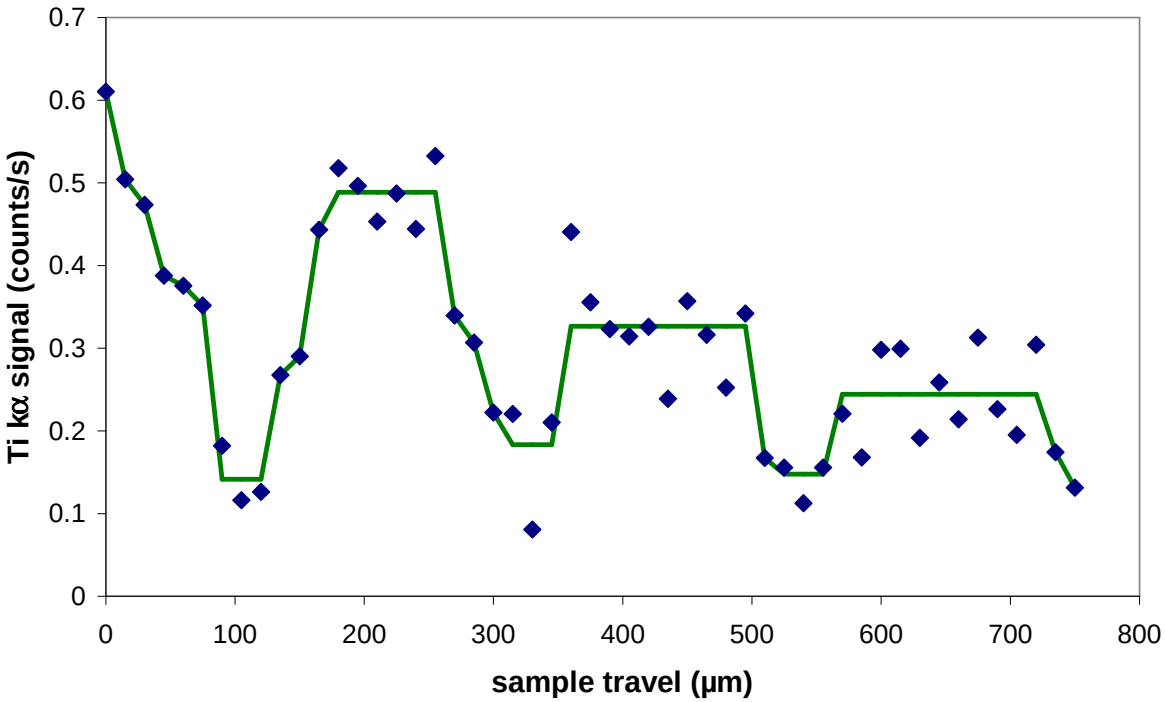

Fig.III.19: *Ti Ka signal as a function of the sample position. Blue dots are the experimental result extracted from raw data, green line is a guide line for the eyes taking into account the convolution phenomenon.* r_{cap} *= 5 µm*

In Figs. III.17-19, dots are experimental values and green lines are guide lines for the eyes taking into account the convolution phenomenon between the capillary aperture and the pattern profile. In fact as pointed out in Fig. III.20 and III.21 the expected profile depends on the capillary radius value regarding the track width. Titanium signal is maximum over a titanium pad. It decreases until the capillary is aligned with the cobalt track centre. However, if $2r_{cap} > d_{track}$ (Fig.III.20), titanium is still detected because the critical angle $\theta_{cTi} = 6.6$ mrad of TiKα in glass (see Eq (III.1)) leads to a field of view larger than the capillary diameter. As the sample scan goes on, the titanium signal increases again. However, if $2r_{cap} < d_{track}$ (Fig.III.21), Ti signal is no longer expected as the capillary is aligned with the cobalt track centre.

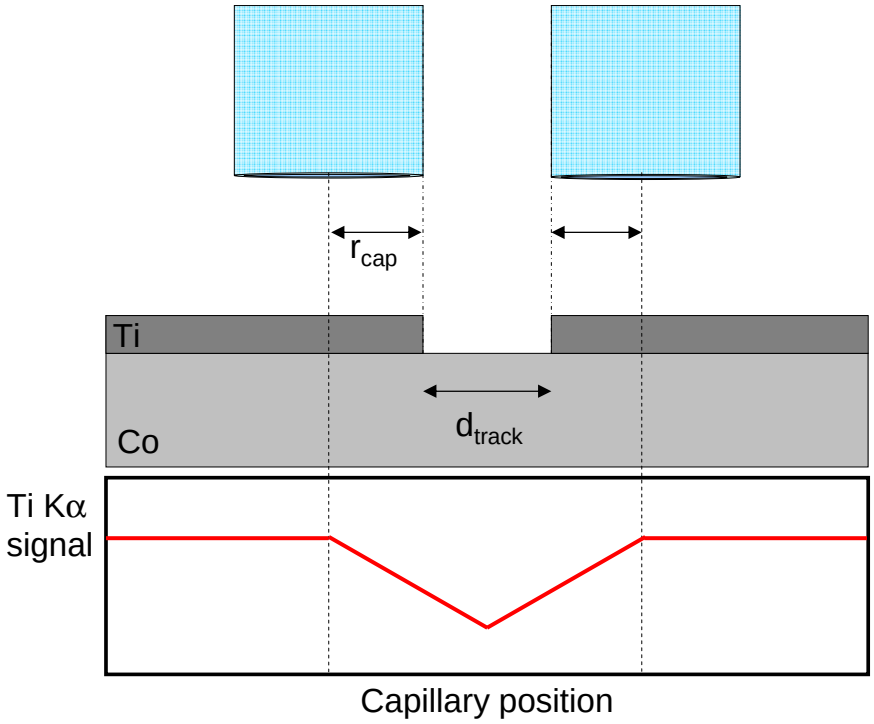

Fig III.20: *Scheme of d_{track} expected profile when $2r_{cap} > d_{track}$*

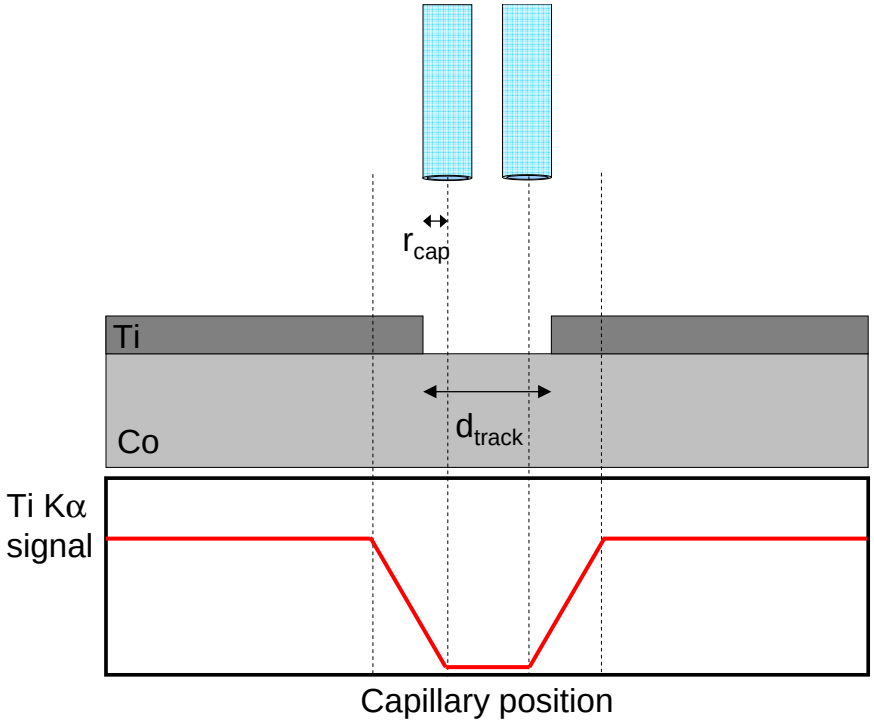

Fig III.21: *Scheme of d_{track} expected profile when 2rcap < d_{track}*

The experimental average distance between tracks Φ_{track} obtained by µXRF is 217µm in good agreement with the 230µm average value deduced from SEM images. According to geometric convolution considerations explained in Fig. III.22, in the case of the 5 µm radius capillary, Ti should NOT be detected over a distance x so that, in a first approximation:

$$x = -2\,rcap - 2\,WD \tan \theta_{cTi} + d_{track} \qquad \text{Eq (III.9)}$$

Because θ_{cTi} = 6.6 mrad and considering a d_{track} value of 36 µm, a value of x = 13 µm is expected. This distance is very close to the step chosen for the profiling (15µm). An accurate measurement of the cobalt track profile is thus not possible from the experimental results and the experiment needs to be refined.

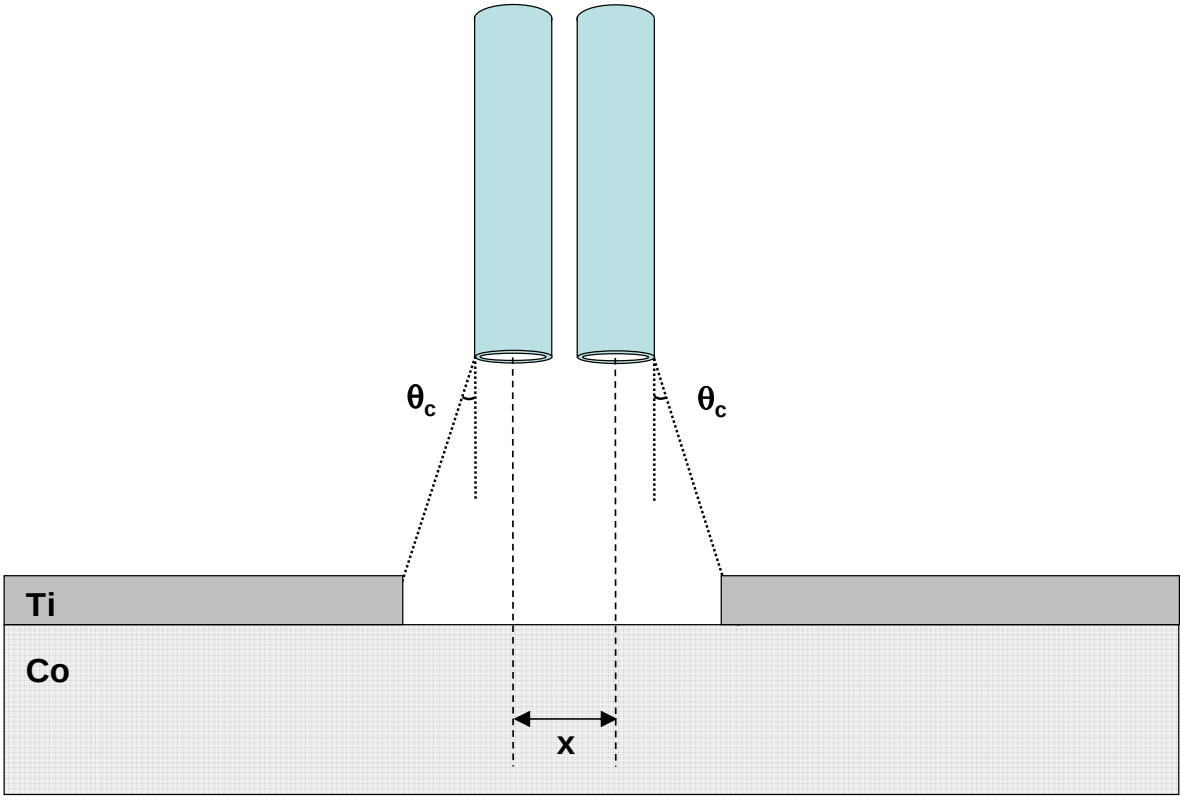

Fig.III.22 : *Capillary excursion over which titanium signal is not detected* (Eq III.9)

We have already mentioned that the Co Kα line is detected all over the capillary excursion because the titanium layer is very thin. However, the CoKα signal varies during the scan due to CoKα line absorption by the titanium layer. The XRF signal collected is maximum (respectively minimum) when the capillary axis is aligned with the Co track centre (respectively with the Ti pad centre). The average ratio between the maximum and the minimum values is 0.88. Taking into account the titanium layer thickness (600 nm) and the CoKα line attenuation length in titanium (7.22 µm) we should expect a maximum to minimum ratio of 0.92. The values are in good agreement.

III.3 Conclusion

We have developed a test-bed for µ-XRF analysis based on capillary optics on both illumination and detection optical paths. It consists in a low power Rh-source focused with a polycapillary lens on the sample and in a 50 mm long and 1 mm outer diameter cylindrical capillary equipping a SDD-EDX detector.

First, we have characterized the primary beam spot within the polycapillary lens focal plane. The X-ray spot lateral profile has a Gaussian shape with a width and magnitude depending on the X-ray energy range. The average half width measured at 1/e is 22 µm and the total X-ray flux is 1.7 10^9 photons.s^{-1}.μm^{-2}. These data are needed for the simulations presented in chapter IV.

The lateral extension of the fluorescence volume emitted by a cobalt test sample was then measured by scanning the detection capillary through the irradiated zone diameter. Significant signal was collected over a distance larger than the irradiated zone. However, simple geometrical considerations could explain the experimental results. We have pointed out here a convolution effect between the capillary aperture and the scanned area. We also studied the influence of the capillary radius on the total signal measured and interpreted the results with a fluorescence point emitter model.

The test-bed was also used to carry out X-ray microscopy using two test pattern. The first, consisted in a molybdenum TEM grid glued on a cobalt sample. The second was a titanium pattern on cobalt sample sputtered through the molybdenum grid. Both Mo- and Ti-Kα XRF profiles could be measured and interpreted considering convolution phenomena between capillary characteristics and pattern geometry.

These results show that it should be possible to collect the fluorescence signal using a thin cylindrical capillary down to 1 µm inner diameter, even with a laboratory microsource. Increasing the acquisition time should then lead to significant signal level enhancement with our EDX-SDD device.

The quantification of this trend needs simulation developments because the X-ray source delivers an extended irradiation on the sample surface. This is the subject of the next chapter.

References

[1] See for example http://www.aps.anl.gov/Beamlines/Directory Nanoprobe Beamline „Nanoprobe 26-ID-C“ (last accessed 18/07/2013)

[2] for example µXRF provided by Horiba Scientific, such as XGT-7200 X-ray Analytical Microscope (http://www.horiba.com/scientific/products/x-ray-fluorescence-analysis/micro-xrf-analyzer/details/xgt-7200-x-ray-analytical-microscope-488/) (last accesed 18/07/2013)

[3] F. Jandard, C. Fauquet, M. Dehlinger, A. Ranguis, A. Bjeoumikhov, S. Ferrero, D. Pailharey, B. Dahmani and D. Tonneau, “Mapping of X-ray induced luminescence using a SNOM probe”, Applied Surface Science 267, 81-85, 2013

[4] C. Fauquet, M. Dehlinger, F. Jandard, S. Ferrero, D. Pailharey, S. Larcheri, R. Graziola, J. Purans, A. Bjeoumikhov, A. Erko, I. Zizak, B. Dahmani and D. Tonneau, “Combining scanning probe microscopy and X-ray spectroscopy”, Nanoscale research letters, 6, 308, 2011

[5] S.P. de Chateaubourg : “La spectrométrie de fluorescence X et l'analyse quantitative de couches minces à l'aide d'échantillons massifs, Application au dosage des aérosols atmosphériques”; 1995. PhD Thesis, Université Paris VII-Paris Diderot. (in French)

[6] A. Bjeoumikhov, S. Bjeoumikhova. (2008), “Capillary Optics for X-Rays”, in Modern Developments in X-ray and Neutron Optics, edited by A. Erko, M. Idir, T. Krist, A.G. Michette, Springer series in Optical Sciences, (Springer-Verlag Berlin Heidelberg) Vol.137, pp. 287-306.

[7] A. Bjeoumikhov, S. Bjeoumikhova, “Capillary optics for X-rays”, in modern Development in X-ray and Neutron optics, edited by A. Erko, M. Idir, T. Krist, A.G. Michette, Springer Series in Optical Sciences, (Springer-Verlag Berlin Heidelberg) Vol.137, pp 287-306

[8] See for example: X-Ray Data Booklet, Center for X-ray Optics and Advanced Light Source, Lawrence Berkeley National Laboratory, 2009, http://xdb.lbl.gov/ (last accessed 18/07/2013).

[9] B.L. Henke, E.M. Gullikson, J.C Davis, “X-ray interactions: photoabsorption, scattering, transmission and reflection at E = 50-30000 eV, Z = 1-92”, Atom Data Nucl Data Tables, 54(2):181–342, 1993

CHAPTER IV: Simulation of XRF signal collection through a cylindrical capillary

In order to estimate the resolution of chemical mapping by XRF using capillary optics both for detection and illumination, we have developed a model to simulate the XRF signal magnitude.

Modelling and numerical calculations have been widely used for X-ray optics design and characterization [1; 2]. Among them, capillary optics are very promising in all characterization tools requiring high brightness X-ray primary irradiation. This is the reason why monocapillary [3, 4] as well as polycapillary lenses [5] are the subject of many simulation works. These simulations are generally carried out within Ray-Tracing™ environment. SHADOW software was developed in the mid 80's on the basis of Ray-Tracing™. This open source program is devoted to the simulation of X-ray optics systems implemented on synchrotron beam lines [6; 7; 8].

Vincze et al. presented for the first time 3D distribution of solid impurities in diamond and of buried fluid inclusions in quartz using a confocal micro-XRF with polycapillary lens for both irradiation and detection [9]. In this case, the analyzed volume is the intersect between the irradiated and the detected volume. Compared to conventional XRF technique, this method offers thus better resolution, depth selectivity, and avoids scatter from other sample regions. They also demonstrated high sensitivity of the technique used with a synchrotron source, down to 50 ppm. The data set was analysed combining the method of Principal component analysis and *K*-means clustering procedure after application of instrument specific routines, presented in the work of Vekemans et al [10].

Smit et al. developed a model to interpret XRF data coming from old artistic paints analyzed at Hazylab synchrotron facility in a confocal geometry [11]. They assumed a spherical interaction volume between the incoming photons and the sample. They took into account for secondary fluorescence induced by hard X-rays and for reabsorption. Their model lead to the profile concentration scan of the paints.

In the same way, Malzer and Kanngieβer developed their own model for 3D-micro XRF in a confocal configuration [12]. They should adapt the fundamental parameter equations to their peculiar experiment geometry. They also took into account self absorption to discuss about in-

depth sensitivity of the technique. After the work of Sokaras et al. [13], Schoonjans et al. took into account secondary fluorescence enhancement in their model, so that they could propose a quantification algorithm for confocal nano-XRF analysis. As an application to their program, they were able to measure inhomogeneous stardust particle sizes of 1.5 µm to 2 µm with an error of 0.25 µm by XRF mapping and could quantify their elemental composition by measuring XRF signal coming from more than 10 elements under synchrotron irradiation [14].

Because the XRF test-bed configuration used in this work is unusual (see chapter III), Ray-Tracing^{TM} environment cannot be friendly-used for such estimations. We have thus developed our own software, inspired on the finite element calculations. Within this model, the collected fluorescence magnitude is numerically calculated as a function of experimental parameters: X-ray source brightness, capillary length and radius and working distance.

IV.1: model

IV.1.1: Simulated system

The simulated system is presented in Fig.IV.1. The X-ray beam incidence is fixed at 45° while the detection capillary is positioned perpendicularly to the sample surface, in agreement with the experimental conditions. The 45° incidence was chosen to simplify flux transfer between adjacent cells. Other incidences would also make more complicated the study of composite materials in further studies.

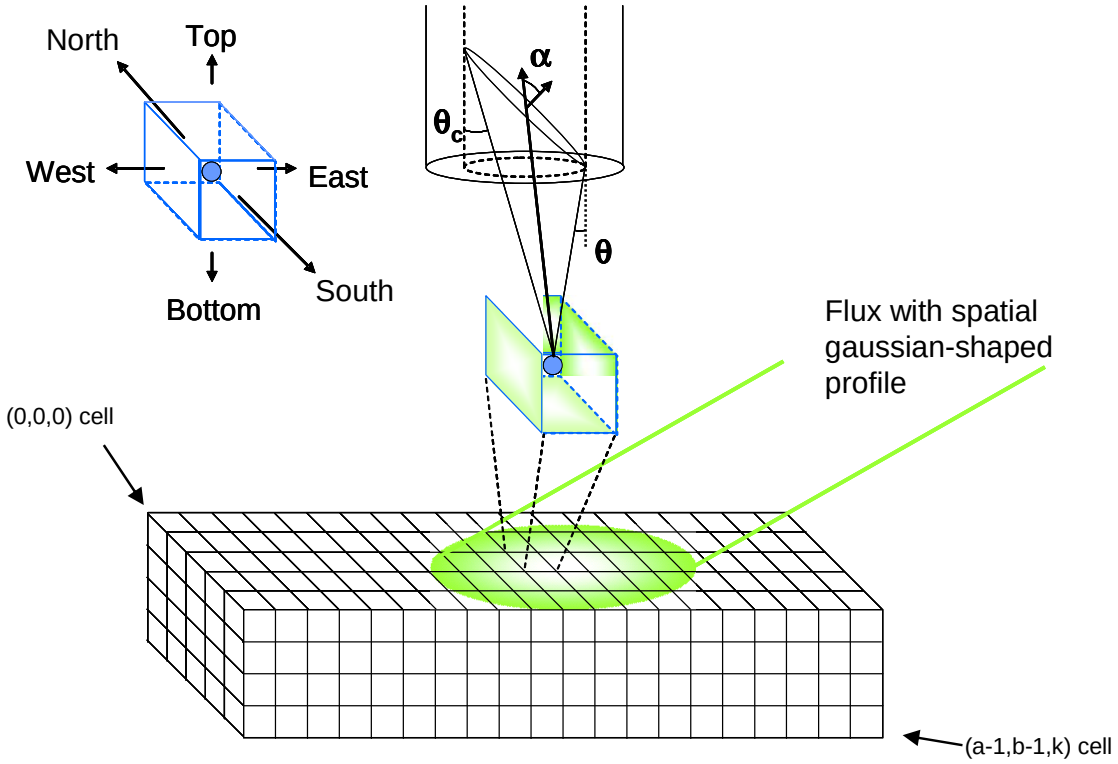

Fig.IV.1: *Simulated system. The sample is divided into cubic unit cells. X-ray fluorescence is emitted from the cell centre. The collected signal is the isotropic fluorescence part emitted within the capillary angle of acceptance.*

The cobalt sample is divided in cubic unit cells (Fig.IV.1) of size L and indexed (i, j, k). There are *a* cells in the **i** and **j** directions and *b* cells in the **k** direction. *a* depends on the sample and cell size. *b* is chosen lower than *a* in order to decrease the computation time by limiting the sample depth to 3 times the attenuation length *x* through the sample at the primary beam energy . According to the primary beam incidence angle of 45°, this corresponds to an optical path of $3x/\cos 45°$ through the sample. A deeper sample is not needed because less than 2% of incident photons reach this depth so that the corresponding collected fluorescence, after reabsorption by the sample matrix, is negligible, because the sample is made of pure Cobalt.

The primary X-ray flux crosses each (i, j, k) cell through its top (Top Input Flux, TIF) and east (East Input Flux, EIF) faces (Fig.IV.1 Insert). Due to the 45° incidence, it exits from the cell centre after absorption via its west (West Output Flux, WOF) and bottom (Bottom Output Flux, BOF) faces to respectively irradiate the (i-1, j, k) and the (i, j, k+1) cells beneath. X-ray fluorescence is assumed to be emitted by the cell centre, considered as a point source. The fluorescence is emitted in 4π directions. The part of the fluorescence emitted within the

detection capillary acceptance is transferred towards the EDX detector. The software takes into account the X-ray fluorescence reabsorption during its travel through the sample before to escape.

The reabsorption phenomenon leads to secondary excitation and thus to secondary emission. An actual finite element calculation should account for this phenomenon. The total collected fluorescence should thus be calculated by successive iterations taking into account the different fluorescence orders, till the signal increase between two successive iterations would become non-significant. However, the secondary fluorescence magnitude is expected in the range of a few percent of the primary one in the case of a pure material. Indeed, the electron binding energy of a given shell is higher than the corresponding fluorescence line energy. For example, binding energy of K1s electrons in Co is 7.709 keV while the corresponding Kα photon transition is 6.930 keV. Thus a Co-Kα photon has not the energy required to induce photo emission of K1s electrons in Co. Consequently, for our approximation, it was not worth to take into account these highest fluorescence orders which would slow down the calculation process. But such iterations could be easily added to the software**.**

IV.1.2:Parameters

The software parameters are:

- Primary X-ray beam characteristics: the primary beam intensity has a Gaussian spatial shape with a cylindrical symmetry around the main axis. The source spectrum is characterized by the Rh X-ray lines superimposed on a broad Brehmsstrahlung spectrum (see sections I.3.2 and III.1.2). For a given energy range, the experimental parameters loaded into the software are: the total number of photons available within this energy range and the beam radius considered at the maximum photons flux/e.
- The unit cubic cell size L
- The sample properties: the attenuation length of the primary beam, the fluorescence yield and the attenuation length of the X-ray fluorescence through the sample before to exit
- The system geometry: the inner detection capillary diameter and length as well as the working distance WD between the detection capillary extremity and the sample surface

- The capillary wall reflectivity at the fluorescence X-ray energy.

IV.1.3: Primary beam absorption along the optical path through the sample

Photons are absorbed through the unit cells following a Beer-Lambert law:

$$I(d) = I(0).e^{-\frac{d}{x}} \qquad \text{Eq (IV.1)}$$

where d is the optical path through a unit cell ($d = \frac{L}{\cos 45°}$), and x the primary beam attenuation length in the cell material. This latter parameter varies with the X-ray energy and the elemental composition of the sample. It is linked to the mass absorption coefficient μ ($cm^2.g^{-1}$) and to the sample density ρ ($g.cm^{-3}$) according to equation 2:

$$x = \frac{1}{\mu\rho} \qquad \text{Eq (IV.2)}$$

Among the different matter - X-ray interactions processes, photoabsorption is the most probable at the primary energy ranges investigated. So we consider that the attenuation length involves only the photoabsorption process.

In the following, the flux designates the number of photons by unit surface and by time unit.

We must consider three kinds of cells to define the different cell input and output fluxes:

- cells at the outermost sample surface (k = 0)
- cells at sample eastern lateral limit (i = a - 1)
- deeper cells (k≠0)

For the topmost surface cells, the incident flux on the top face (TIF (i, j, 0)) is given by the illumination parameters (first boundary condition).

$$TIF(i, j, 0) = \frac{N_0}{\pi.r_{spot}{}^2} \exp\left(-\frac{\left(x.\sin\left(\frac{\pi}{4}\right)\right)^2 + y^2}{r_{spot}{}^2} \right) \qquad \text{Eq (IV.3)}$$

(see figure IV.2)

where (x,y) is the position of cell (i, j, 0) on the surface.

The sample size is wider than the primary X-ray beam diameter. Because of the Gaussian spatial shape beam profile, TIF (a-1, j, 0) is not null but remains weak. On the

contrary, another boundary condition is that the east input flux through the cells located at the sample eastest border is null (EIF(a-1, j, k) = 0) for all j and k values.

The other fluxes are given by the Eq (IV.4a), b) and c))

$$WOF(i,\ j,0) = TIF(i,\ j,0).\exp(-\frac{d}{x_{i,\ j,0}}) \qquad \text{Eq (IV.4a))}$$

$$EIF(i-1,\ j,0) = WOF(i,\ j,0) \text{ providing i > 1} \qquad \text{Eq (IV.4b))}$$

$$BOF(i-1,\ j,0) = EIF(i-1,\ j,0).\exp(-\frac{d}{x_{i-1,\ j,0}}) \qquad \text{Eq (IV.4c))}$$

where $x_{i,j,k}$ is the attenuation length of the (i,j,k) cell material (see figure IV.2)

Then, the TIF and EIF fluxes (see figure IV.2) for the deeper cells are given by:

$$TIF(i-k,\ j,k) = TIF(i,\ j,0).\exp(-\sum_{l=0}^{l=k-1}\sum_{m=l}^{m=l+1}\frac{d}{x_{i-m,\ j,l}}) \qquad \text{Eq (IV.5a))}$$

$$EIF(i-k,\ j,k-1) = TIF(i,\ j,0).\exp\left(-\sum_{l=0}^{l=k-1}(\frac{d}{x_{i-l,\ j,l}}) - \sum_{m=1}^{m=k-1}(\frac{d}{x_{i-m,\ j,m-1}})\right) \qquad \text{Eq (IV.5b))}$$

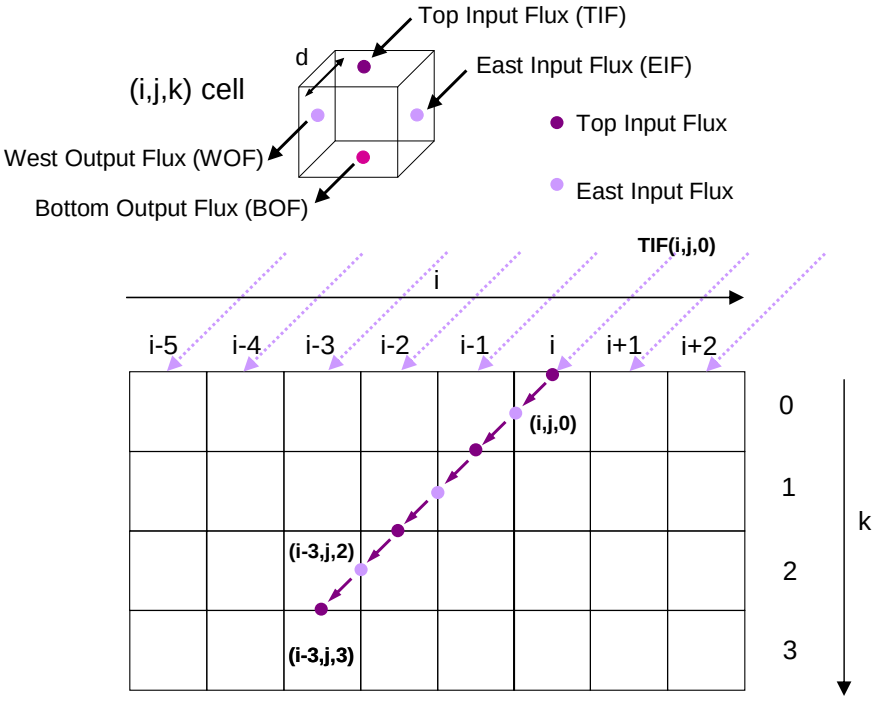

Fig.IV.2: *optical path of a primary X-ray impinging on the top face of the surface cell (i, j, 0). The different input and output fluxes are represented on the top of the figure. On the bottom is shown an illustration concerning the cells index used to establish the Eq (IV.5a) and b)).*

The flux that exits via the south (respectively west) face is of course equal to the flux that enters via the north (respectively east) face of the cell immediately below (respectively beside).

$$WOF(i, j, k) = EIF(i-1, j, k) \qquad \text{Eq (IV.6a))}$$

$$BOF(i, j, k) = TIF(i, j, k+1) \qquad \text{Eq (IV.6b))}$$

Finally, the number of photons absorbed by time unit by the (i, j, k) cell is given by:

$$APF(i, j, k) = L^2.(EIF(i, j, k) - SOF(i, j, k) + TIF(i, j, k) - WOF(i, j, k)) \qquad \text{Eq (IV.7)}$$

where L is the cubic cell size. All these values are then stored in a 3-D matrix.

IV.1.4: Cell fluorescence

The cell fluorescence is the product of the absorbed primary flux (APF) by the excitation factor τ. This factor τ is the product of the K-shell electron ejection probability j_K, of the fluorescence yield ω_K, and of the transition probability $g_{K\alpha}$ to give a Kα transition rather than a Kβ. The parameters for materials considered in this work are gathered in table IV.1:

Element	j_K	ω_K	$g_{K\alpha}$	total Kα yield = $\tau_{K\alpha}$
Ti	0.880	0.213	0.883	0.165
Fe	0.877	0.387	0.882	0.268
Co	0.873	0.381	0.867	0.288
Mo	0.842	0.765	0.838	0.540

Table IV.1: *Fundamental parameters and total Kα yield for the elements used in this study. Data were taken from* [15-19]

IV.1.5: Fluorescence collection

Each cell is now considered as a point source positioned at its centre and emitting in 4π directions. For a given cell, the collected Kα fluorescence flux CF is given by:

$$CF(i,j,k) = APF(i,j,k).j_K.\omega_K.g_{K\alpha}.\frac{\Omega}{4\pi}.\exp(-\Sigma\frac{d_{i',j',k'}}{x_{i',j',k'}}) \qquad \text{Eq (IV.8)}$$

where Ω is the effective collection solid angle, limited by the extreme rays reaching the capillary inner wall under an incidence angle θ lower than the critical total reflectance angle θ_c. θ_c is given by Equation IV.9 [20]:

$$\theta_c = \frac{0.02\sqrt{\rho}}{E} \qquad \text{Eq (IV.9)}$$

where ρ is the density of the reflecting material (in g.cm^{-3}) and E the primary energy (in keV). Because the X-ray capillaries used in the experimental work are made of fused silica, the value of ρ = 2.2 g.cm^{-3} is used here.

The exponential factor in equation IV.8 accounts for X-ray fluorescence reabsorption along the path from the emitting cell centre to the capillary aperture. We assume a constant

optical path $d_{i',j',k'}$ for all the paths within the capillary acceptance, given by the straight line joining the centres of the cell (i, j, k) and of the capillary aperture.

Note that Eq (IV.8) does not account for intensity losses due to multiple reflections on the detection capillary inner wall which leads to drastic intensity losses at low capillary radius. The influence of this latter effect will be discussed at the end of this model description (see Chapter IV section IV.1.5.2).

IV.1.5.1: Effective collection solid angle

The key of the collected fluorescence signal magnitude estimation remains in the calculation of the effective collection solid angle Ω for each unit cell. It strongly varies with the position of the emitting cell centre regarding the capillary axis and with WD, the capillary extremity to sample distance. Ω is limited by the fluorescence X-rays impinging the capillary inner wall under an incidence angle equal or lower than the critical angle θ_c. Note that Ω is equal or lower than the geometrical solid angle under which we see the capillary aperture from the cell centre.

We have considered 3 kinds of cells (Fig.IV.3):

- cells aligned with the cylindrical capillary axis (A-type)
- cells aligned with the aperture but not with the capillary axis (B-type)
- cells not aligned with the capillary aperture (C-type)

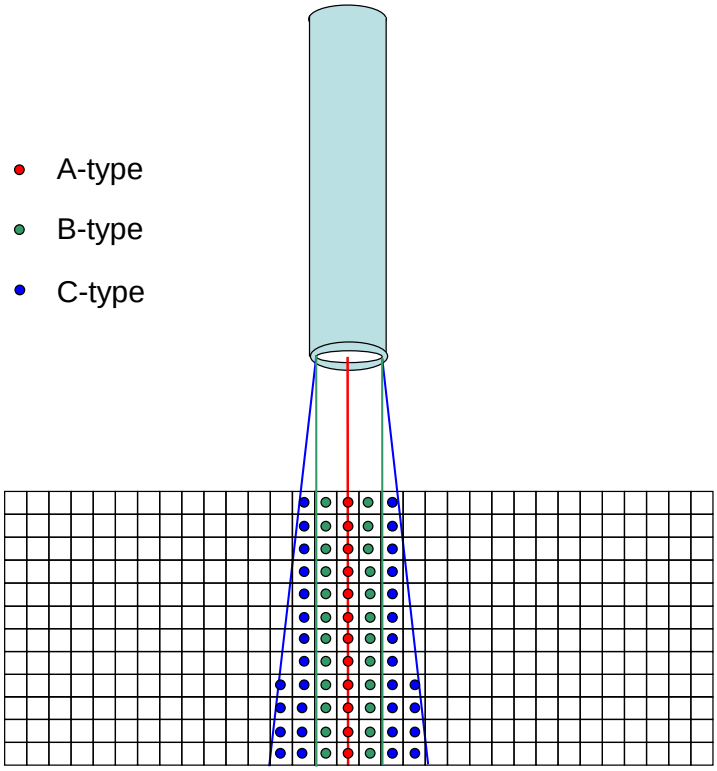

Fig.IV.3: *Illustration of the three different kinds of cells according to their position regarding the capillary axis and aperture.*

Fig.IV.4a), b) and c) presents the system scheme and the relevant geometrical parameters involved in the calculations of effective solid angles for each cell position. For A-type cells (Fig. IV.4a)), the collection solid angle is a conus with a revolution axis aligned with the capillary axis, and limited by the critical angle θ_c. For B-type cells, the conus axis is not aligned with the capillary axis. The capillary acceptance corresponding to these cells is limited by two extreme distinct points A_1 and A_2 situated respectively at distances δ_1 and δ_2 from its extremity (Fig.IV.4b)). For C-type cells, the solid angle is a very tiny portion of the emitting sphere (Fig.IV.4c)). The geometrical capillary acceptance is limited by two extreme rays impinging the capillary edge. These rays impinge the capillary wall under incidences θ_A and θ_B. The capillary effective acceptance depends on the values of these angles compared to θ_c.

The effective solid angle calculations are developed in the annex. The expressions of the effective collection solid angles are gathered in table IV.2a), b) and c). Notations are given in Figs.IV.4(a)-(c) and in the annex.

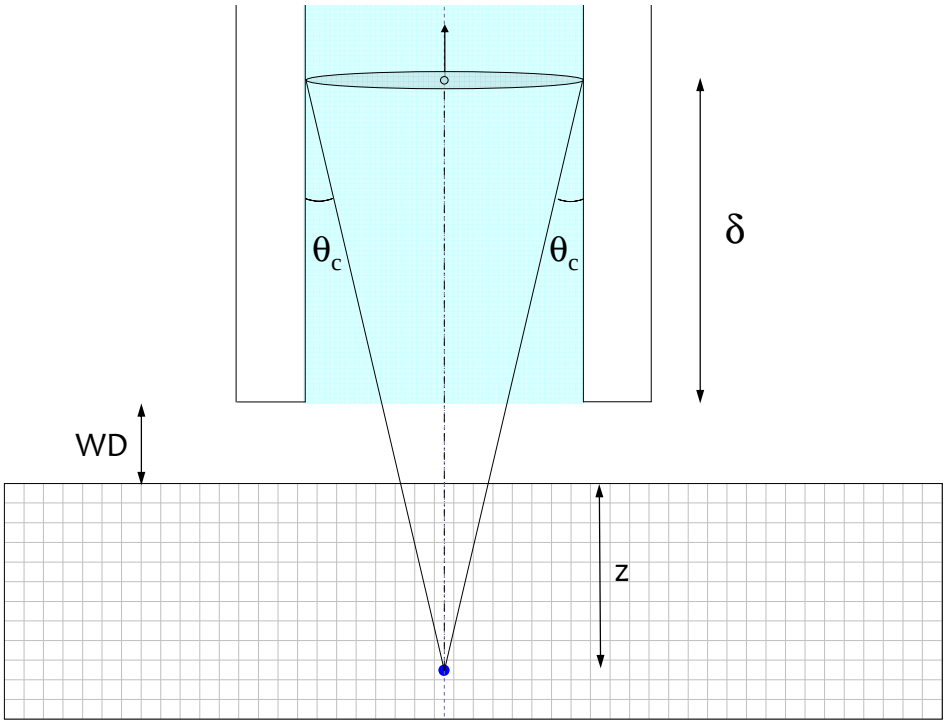

Fig.IV.4a) : *Scheme of the solid angle determination in the case of the A cells*

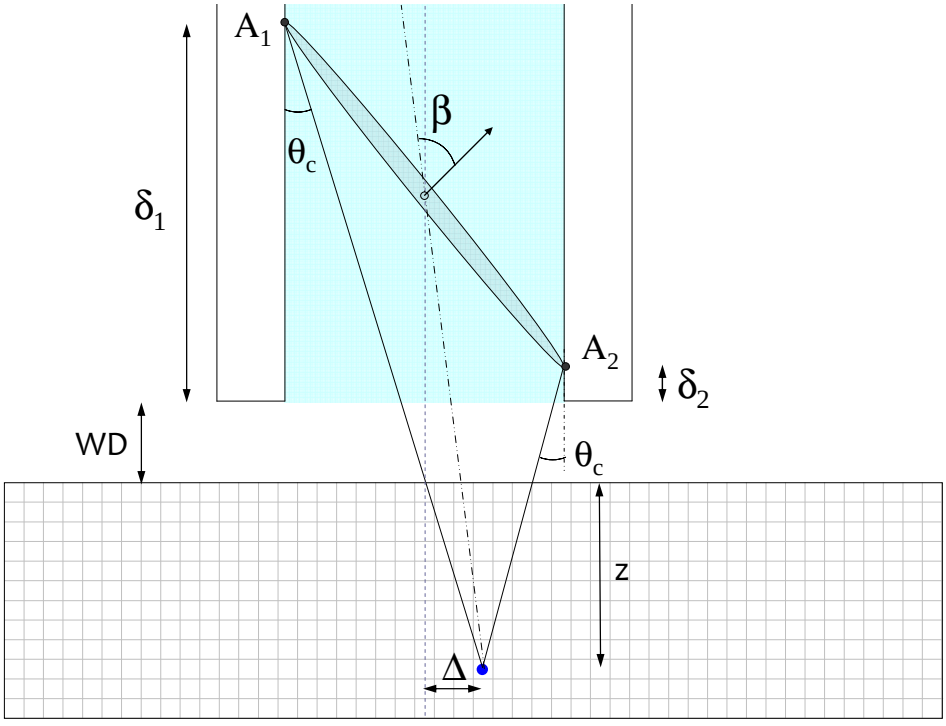

Fig.IV.4b) : *Scheme of the solid angle determination in the case of the B cells*

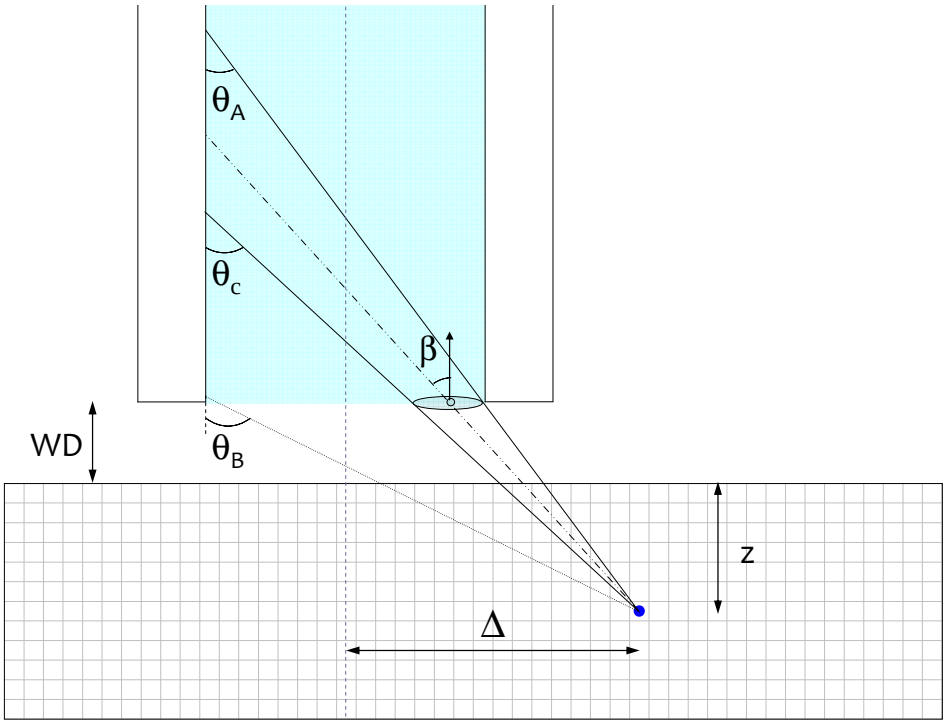

Fig.IV.4c): *Scheme of the solid angle determination in the case of the C cells*

A-type cells (see Fig.IV.4a) for notations)	
Solid angle expression	Condition
$\Omega = \pi.\tan^2(\theta_c)$	0<δ<L
$\Omega = \frac{\pi.r_{cap}^{\ 2}}{(WD+z)^2}$	δ<0
$\Omega = \frac{\pi.r_{cap}^{\ 2}}{(L+WD+z)^2}$	L<δ

Table IV.2a): *Solid angle expression for the A- type cells*

B-type cells (see Fig.IV.4b) for notations)	
Solid angle expression	Condition
$\Omega = \frac{\frac{1}{2}\pi\, r_{cap} \cdot \sqrt{(2.r_{cap})^2 + (\delta_1 - \delta_2)^2}\cos(\beta)}{\Delta^2 + (\frac{\delta_1 + \delta_2}{2} + WD + z)^2}$ With $\beta = \frac{\pi}{2} - Arc\tan(\frac{r_{cap}}{1/2.(\delta_1 - \delta_2)}) + Arc\tan(\frac{\Delta}{WD + z + \frac{\delta_1 + \delta_2}{2}})$	$0<\delta_2<\delta_1<L$
$\Omega = \frac{\frac{1}{2}\pi\, r_{cap} \cdot \sqrt{(2.r_{cap})^2 + \delta_1^{\,2}}\cos(\beta)}{\Delta^2 + (\frac{\delta_1}{2} + WD + z)^2}$ With $\beta = \frac{\pi}{2} - Arc\tan(\frac{r_{cap}}{1/2.\delta_1}) + Arc\tan(\frac{\Delta}{WD + z + \frac{\delta_1}{2}})$	$\delta_2<0<\delta_1<L$
$\Omega = \frac{\pi.r_{cap}^{\,2}.\cos(\tan^{-1}(\frac{\Delta}{WD + z}))}{\Delta^2 + (WD + z)^2}$	$\delta_2<\delta_1<0$
$\Omega = \frac{\frac{1}{2}\pi\, r_{cap} \cdot \sqrt{(2.r_{cap})^2 + (L - \delta_2)^2}\cos(\beta)}{\Delta^2 + (\frac{L_1 + \delta_2}{2} + WD + z)^2}$ With $\beta = \frac{\pi}{2} - Arc\tan(\frac{r_{cap}}{1/2.(L - \delta_2)}) + Arc\tan(\frac{\Delta}{WD + z + \frac{L + \delta_2}{2}})$	$\delta_2<L<\delta_1$
$\Omega = \frac{\pi.r_{cap}^{\,2}.\cos(\tan^{-1}(\frac{\Delta}{WD + z + L}))}{\Delta^2 + (WD + z + L)^2}$	$L<\delta_2<\delta_1$

Table IV.2b): *Solid angle expression for the B - type cells*

C-type cells (see Fig.IV.4c) and Annex for notations)	
Solid angle expression	condition
$\Omega = \frac{\pi.r_{cap}{}^2.\cos(Arc\tan(\frac{\Delta}{WD+z}))}{\Delta^2+(WD+z)^2}$	$\theta_A<\theta_B<\theta_c$
$\Omega = \frac{A.(WD+z)}{[(WD+z)^2+(\frac{\Delta - r_{cap}+(\tan(\theta_c).(WD+z))}{2})^2]^{3/2}}$ With $A_2 = r_{cap}{}^2\alpha + \frac{1}{2}\left\|\overrightarrow{C_1C_2}\right\|[(\frac{1}{2}(\left\|\overrightarrow{C_0'O'}\right\| - h)\pi) + h]$	$\theta_A<\theta_c<\theta_B$ and $S > \frac{\pi.r_{cap}{}^2}{2}$
$\Omega = \frac{A.(WD+z)}{[(WD+z)^2+(\frac{\Delta - r_{cap}+(\tan(\theta_c).(WD+z))}{2})^2]^{3/2}}$ With $A_1 = r_{cap}{}^2\alpha + \frac{1}{2}\left\|\overrightarrow{C_1C_2}\right\|[(\frac{1}{2}(\left\|\overrightarrow{C_0'O'}\right\| - h)\pi) - h]$	$\theta_A<\theta_c<\theta_B$ and $S < \frac{\pi.r_{cap}{}^2}{2}$

Table IV.2c): *Solid angle expression for the C - type cells*

IV.1.5.2: Capillary wall reflectivity

A cylindrical capillary guides X-ray radiation by total external reflection. A beam impinging on the glass surface under the critical angle is reflected one or several times till reaching the detector at the capillary output. The reflection coefficient gives the signal yield transmitted at each reflection. It is given by the Fresnel formula: [20]

$$R(\theta) = \frac{(\theta-\theta_1)^2+\theta_2^2}{(\theta+\theta_1)^2+\theta_2^2} \qquad \text{Eq(IV.10a))[20]}$$

where

$$\theta_1 = \frac{1}{\sqrt{2}}\sqrt{\sqrt{\left((\theta^2-\alpha)^2+\beta^2\right)}+\theta^2-\alpha} \qquad \text{Eq(IV.10b))[20]}$$

$$\theta_2 = \frac{1}{\sqrt{2}}\sqrt{\sqrt{\left((\theta^2-\alpha)^2+\beta^2\right)}-\theta^2+\alpha} \qquad \text{Eq (IV.10c))[20]}$$

In these equations, α and β are the real and imaginary parts of the refraction index as shown in the following equation:

$$n = 1-\frac{\alpha}{2}+i\frac{\beta}{2} \qquad \text{Eq (IV.11)}$$

Note that for X-rays the real part of the refractive index is very close but inferior to one. For example, in the case of Co Kα radiation on fused silica, $\alpha=2.056.10^{-5}$, $\beta=6.230.10^{-7}$. (from [21]).

The reflection coefficient R(θ) is close to one for incident angle equal or lower than θ_c and it rapidly falls to zero when $\theta > \theta_c$ (see Fig IV.5).

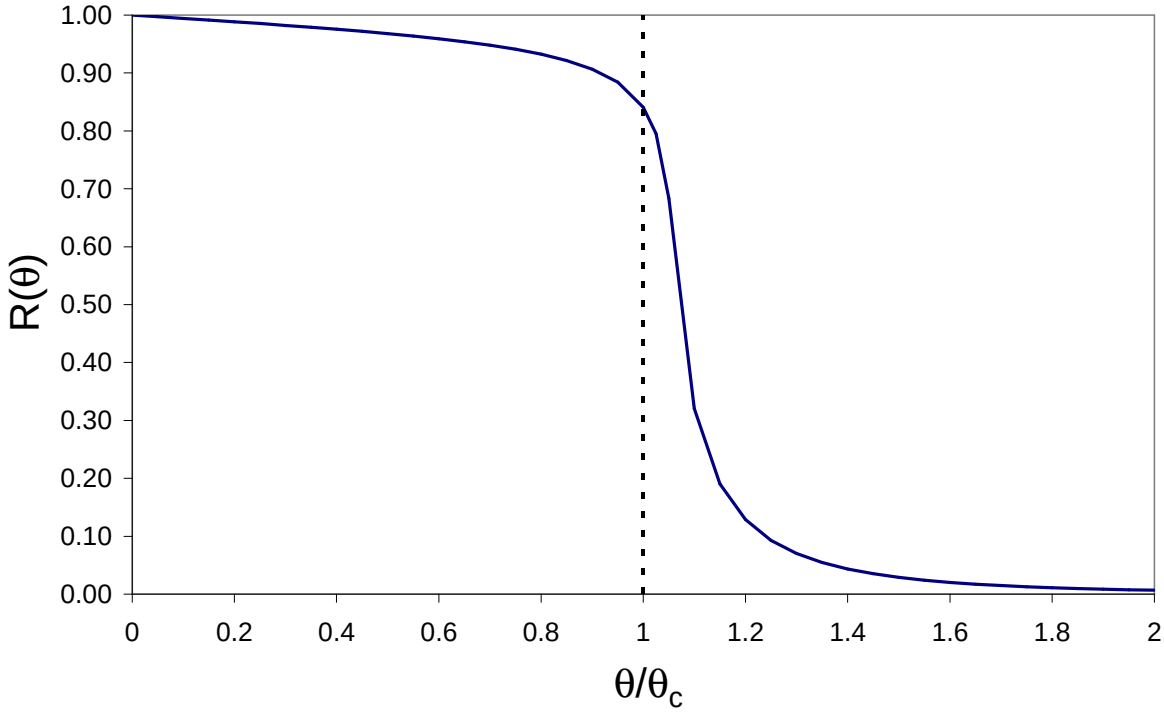

Fig IV.5: *Reflection coefficient R(θ) as a function of θ/θc.*

If $\theta < \theta_c$, we can see that there is nearly no signal loss for a single reflection but in the case of N reflections on the capillary wall we have:

$$R(\theta) = \left(\frac{(\theta - \theta_1)^2 + \theta_2^2}{(\theta + \theta_1)^2 + \theta_2^2} \right)^N \qquad \text{Eq (IV.12)}$$

Because multiple X-ray reflections occur along the capillary inner wall, (from 0 to several hundreds in the case of a 50 mm long and 1µm diameter capillary at the critical angle of reflection) we take into account this coefficient in our calculation.

To do so, we select 20 rays indexed from i = 0 to i = 19, that impinge the capillary inner wall under the capillary acceptance Δθ. There is a slight variation in the processing for each solid angle case. An example is given in Fig. IV.6 for a peculiar B-type cell. Then we calculate the reflection number N on the capillary wall for all these rays, knowing the incidence and the capillary length. The transmission for each of the 21 rays is calculated. Finally, we assume that the capillary transmission is the average of these 21 transmission

values. For example in the case of A-type cells positioned on the capillary axis, (fig.IV.3) we find:

$$R = \frac{1}{20}\sum_{i=0}^{i=19_c}\left(\frac{(\theta_i-\theta_1)^2+\theta_2^2}{(\theta_i+\theta_1)^2+\theta_2^2}\right)^N \qquad \text{Eq (IV.13a))}$$

Where

$$N = \frac{L_{cap}-(\frac{r_{cap}}{\tan(\theta_i)}-WD-z)}{\left(\frac{2.r_{cap}}{\tan(\theta_i)}\right)} \qquad \text{Eq (IV.13b))}$$

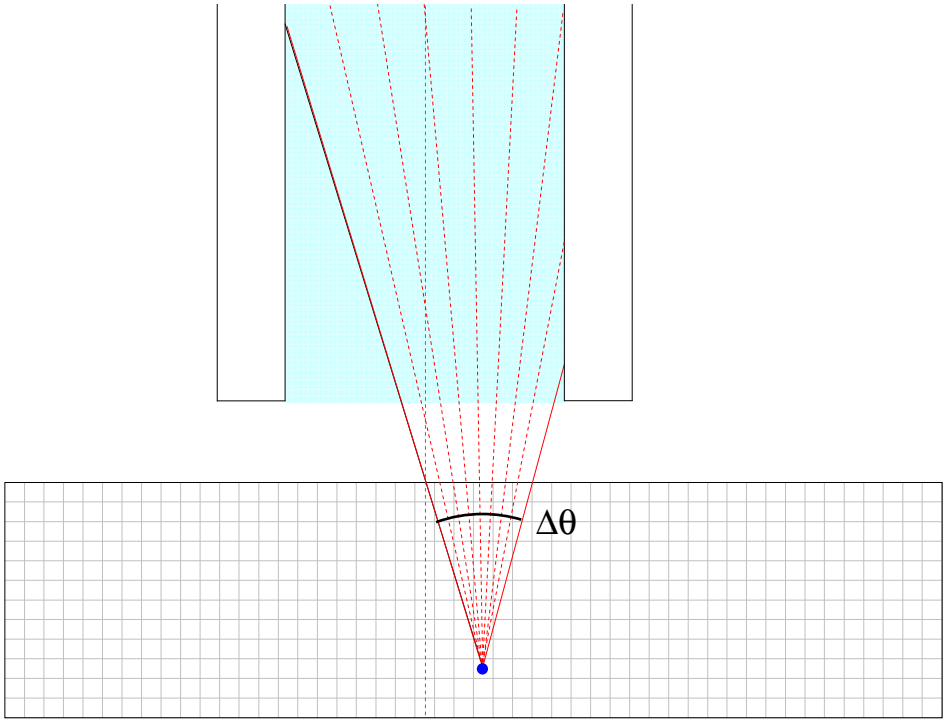

Fig IV.6*: Illustration of the method used for reflection coefficient calculation for a peculiar B-type cells. Among the 20 rays used for calculation, 9 rays within the capillary acceptance are represented.*

In conclusion, for each emitting cell, the program calculates:

- the effective capillary collection solid angle (see section IV.1.5.1)
- Δθ calculation

- Calculation of the incidence angle θ_i of 20 intermediate rays within $\Delta\theta$
- Calculation of the number of reflections of the 20 intermediate rays and the corresponding capillary transmission.
- Capillary transmission is the average of the 20 preceding values

IV.2: Results and discussion

IV.2.1. Summary of primary beam characteristics

Primary beam characteristics of the Rh-Ka source are developed in sections III.1.2. In brief, the source spectrum exhibits narrow Rh-K_α, Rh-$K_{\beta 1}$ and Rh-$K_{\beta 2}$ rays at 20.216, 22.074 and 22.724 keV respectively and X-rays from the L shell excitation at 2.697, 2.692, 2.834, 3.001 and 3.144 keV superimposed on a wide Bremsstrahlung. The beam radius value measured at 1/e and the photon flux in the polycapillary lens focal plane depend on the energy range. A summary is given in table IV.3. The total photon flux within the primary spot is 1.7 10^9 photons.s^{-1}.μm^{-2}.

Energy Range (keV)	Beam radius at 1/e (µm)	Photon flux (photon.s^{-1}.μm^{-2})
3-5	26	$1.08.10^7$
5-7	26	$3.41.10^7$
7-9	19.8	$9.20.10^7$
9-11	28	$4.69.10^8$
11-13	28.6	$7.01.10^8$
13-15	18.2	$1.04.10^8$
15-17	20.8	$7.75.10^7$
17-19	18.2	$4.33.10^7$
19-21	20.8	$1.12.10^8$
21-23	26	$5.79.10^7$
23-25	26	$2.36.10^7$
25-27	27.3	$1.52.10^7$

Table IV.3: *Primary beam radius at 1/e and photon flux in the polycapillary lens focal plane as a function of the energy range.*

We have studied the influence of the system geometry, capillary radius r_{cap} and length L_{cap} as well as capillary tip-sample working distance WD on the detected signal magnitude. In a first series of calculations, the capillary length and the working distance are fixed at 50 mm and 1mm respectively, values chosen in our experiments (see preceding chapter). The case of fluorescence collection from a cobalt sample is compared with experiments for simulation validation. In all calculations, the cell size is chosen smaller than the capillary radius.

IV.2.2 Influence of Capillary radius and working distance on signal magnitude

In figure IV.7 the dependence of capillary radius on the collected signal magnitude for a fixed WD of 1 mm is shown (blue dots). For wide capillary radii, the collected signal magnitude varies as $r_{cap}^{1.8}$. For lower capillary radii however, the expected signal decreases drastically. We have reported on the same figure (green triangles) the experimental data (taken from Fig. III.8), in very good agreement with the simulation. From this result, we can say that the simulation software successfully reflects the experiments. The slight discrepancy between experiments and simulation (20 to 60%) may have several origins. First the primary beam incidence regarding the sample surface in our experiments was 30° while we have chosen 45° in the modelling to simplify the calculations (see above). This induces a systematic error of 30% (= cos 60° / cos 45°). Another factor is the reflection critical angle on the capillary inner wall which might be lower than the theoretical one given by equation IV.9. In fact, this angle strongly depends on the glass composition thus on its density as well as on the inner wall roughness and average curvature.

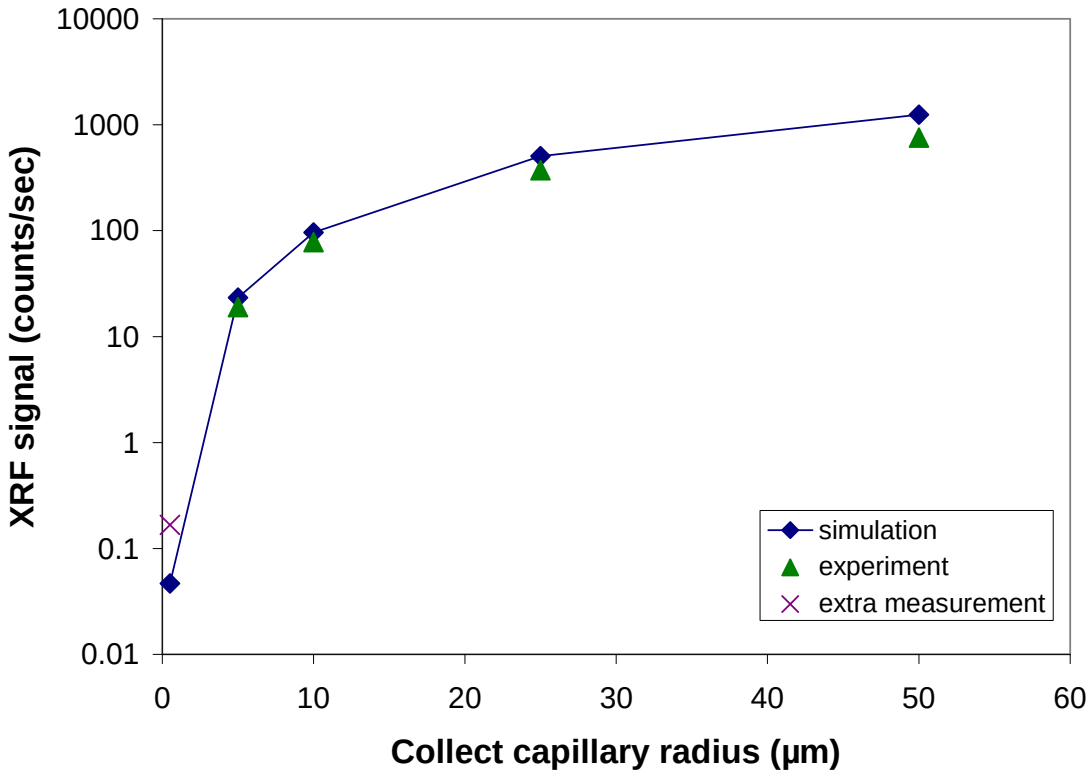

Fig IV.7: *Collected XRF signal magnitude as a function of the capillary radius used for collection. The capillary length is 50 mm and the working distance 1 mm.*

A preliminary measurement was performed with a 0.5 µm radius capillary just after alignment process. For that peculiar point the capillary length was shortened down to 35 mm and the acquisition time was fixed at 250s. Several spectra were acquired with a very low signal/background ratio (3 to 4). The collected fluorescence signal magnitude is about 0.17 counts.s^{-1}.

Although the signal to noise ratio is very low, this extra measurement seems to be in good agreement with simulations (see Fig. IV.7). The slight discrepancy may come from the fact that the 0.5µm radius capillary is shorter than those simulated. In this case, as shown further (Fig IV.12 section IV.2.2.2), a 1.7 signal enhancement is expected.

This preliminary result needs more experiments to be finalized.

IV.2.2.1: Working Distance influence at constant capillary length

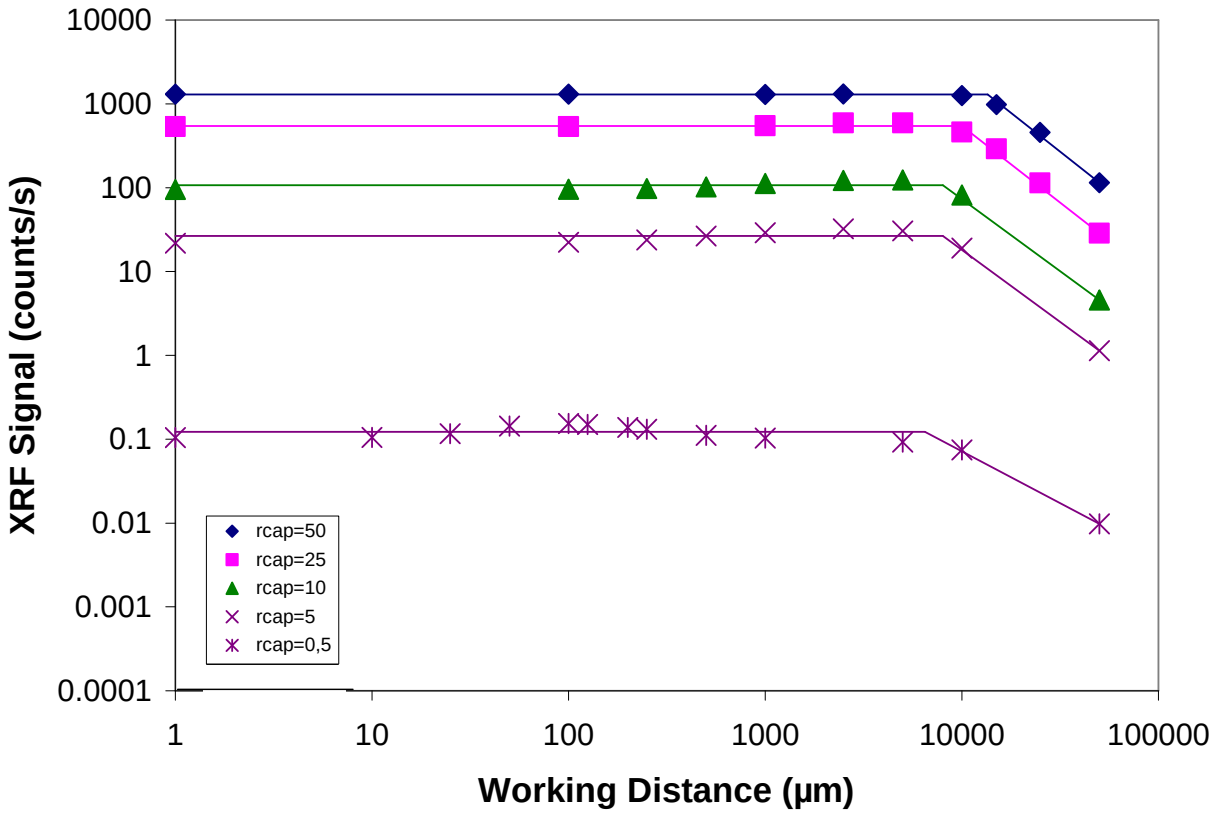

Fig.IV.8 *Simulated XRF signal variation with the working distance. The capillary length is 20 mm. The line is a guide to the eyes.*

Figure IV.8 shows the dependence of the collected signal magnitude on the working distance WD for different capillary radii. The capillary length is fixed at L = 20 mm. Note that in such conditions, the detector to sample surface distance L+WD varies for this study. As it can be seen in the figure IV.8, at short working distance, the collected signal remains constant when WD increases and the signal magnitude depends only on the capillary radius. Then, at large working distances, the collected signal decreases as $WD^{-1.8}$. For the smallest capillary radius (0.5 µm), simulation shows that the signal magnitude should not vary until a WD of 8 mm. These variations should be compared to the ideal case of the signal collection from a point source.

Figure IV.9a) presents a scheme of classical XRF collection from a point source through a pinhole. The collected signal S_0 depends on the pinhole aperture and is given by:

$$S_0 = N \pi r_{pinhole}^2 / 4 \pi d^2 = N r_{pinhole}^2 / 4 d^2 \qquad \text{Eq (IV.14)}$$

where N is the photon flux emitted by the point source and d the pinhole to point source distance. If the detector is equipped with a cylindrical X-ray capillary with the same diameter

as the pinhole's, the collected signal increases because the effective collection solid angle increases (Fig.IV.9b)). This is true until the angle θ_1 under which the capillary aperture is seen from the point source remains smaller than the glass critical angle. In this case, the X-rays entering the capillary are limited by those transmitted by multiple reflections at grazing incidence. The signal magnitude is limited by the capillary aperture dimensions. The signal collected S_1 is now given by:

$$S_1 = N\ 2\ \pi\ (1-\cos(\theta_1))\ /\ 4\ \pi = N\ [1-\cos(\theta_1)]\ /\ 2 \qquad \text{Eq (IV.15)}$$

Because θ_1 is a small angle:

$$S_1 \approx N\ \theta_1^{\,2}\ /\ 4 \qquad \text{Eq (IV.16)}$$

Thus, adding a capillary to the detector input enhances the signal collected by a gain G:

$$G = S_1\ /\ S_0 \approx [\theta_1\ d\ /\ r_{pinhole}]^2 \qquad \text{Eq (IV.17)}$$

Since the angles are small:

$$\tan(\theta_1) = r_{pinhole}\ /\ WD \approx \theta_1 \qquad \text{Eq (IV.18)}$$

Thus:

$$G(L) \approx d^2\ /\ WD^2 \approx [(WD + L)/\ WD]^2 \approx [1 + L/WD]^2 \qquad \text{Eq (IV.19)}$$

Finally, at short WD or long capillary length L:

$$G(L) \approx [L\ /\ WD]^2 = [L\ \theta_1\ /\ r_{cap}]^2 \qquad \text{Eq (IV.20)}$$

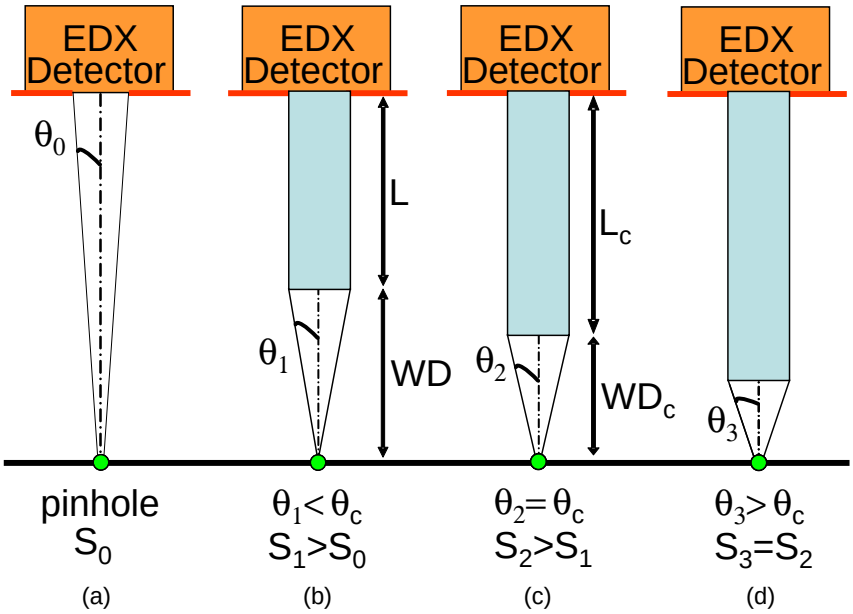

Figure IV.9: *Scheme of the XRF detection from point source at various WD from the capillary extremity. (a) Classical XRF collection from a point source through a pinhole, (b) A capillary with identical radius is added, (c) the working distance is reduced to its critical value WD_c (d) the WD is reduced below WD_c. At the bottom, expected variation of the signal S is reported.*

If the capillary length L is increased, the working distance WD is shrunken and the collected signal S_2 is enhanced. When the capillary length reaches the critical value L_c , the working distance reaches the value WD_c defined by:

$$\tan(\theta_c) = r_{pinhole} / WD_c \approx \theta_c \qquad \text{Eq (IV.21)}$$

In this case the angle under which the capillary aperture is seen from the point source is equal to the critical angle (Fig.IV.9c)). If WD is still shrunken or if L is increased above the L_c value (Fig.IV.9d)), the signal is no more limited by the capillary aperture but only by the critical angle. In fact, among all the X-rays penetrating the capillary, only those impinging on the capillary inner wall under an incidence lower than the critical angle will be transmitted. Then, the collected signal S_3 remains constant (S_3=S_2). The maximum capillary gain G_{max} is thus reached when $WD_c \approx r_{pinhole} / \theta_c$ so that:

$$G_{max} = G(L_c) \approx [1 + L_c \theta_c / r_{cap}]^2 \approx [L_c \theta_c / r_{cap}]^2 \qquad \text{Eq (IV.22)}$$

The 50 µm radius capillary collecting the cobalt X-Ray fluorescence at WD = 1mm from the sample most closely reflects the point source ideal case. For this capillary, the WD_{c50} calculated value from Eq IV.21 is 10 mm (θ_c is 4.3 mrad for Co Kα radiation). The simulation data presented in figure IV.8 exhibit the expected behaviour. For the 5 µm radius capillary, the expected WD_{c5} is 1,17 mm. However, the simulation results indicate a signal decrease above a WD_c value of 6.5 mm. This discrepancy is due to the fact that the source can not be considered as a point source for low diameter capillaries.

To simulate a point source, we have considered the emission coming exclusively from A-type cells, i. e. from cells aligned with the capillary axis**.** In Fig.IV.10 are shown the variations of the collected signal coming only from those cells as a function of WD. For all capillaries the signal remains constant until their corresponding value of WD_c, effectively proportional to capillary radius. The WD_c values of 0.125, 1, 2.5, 5 and 10mm are found for capillary radii of 0.5, 5, 10, 25 and 50 µm respectively in Fig. IV.10. These values are in good agreement with the values of 0.12, 1.17, 2.34, 5.84 and 11.68 mm expected from equation IV.21**.** Moreover, at working distances lower than the critical one, we can observe that the order of magnitude of the plateau level is nearly independent of the capillary radius, except for the 0.5 µm radius capillary.

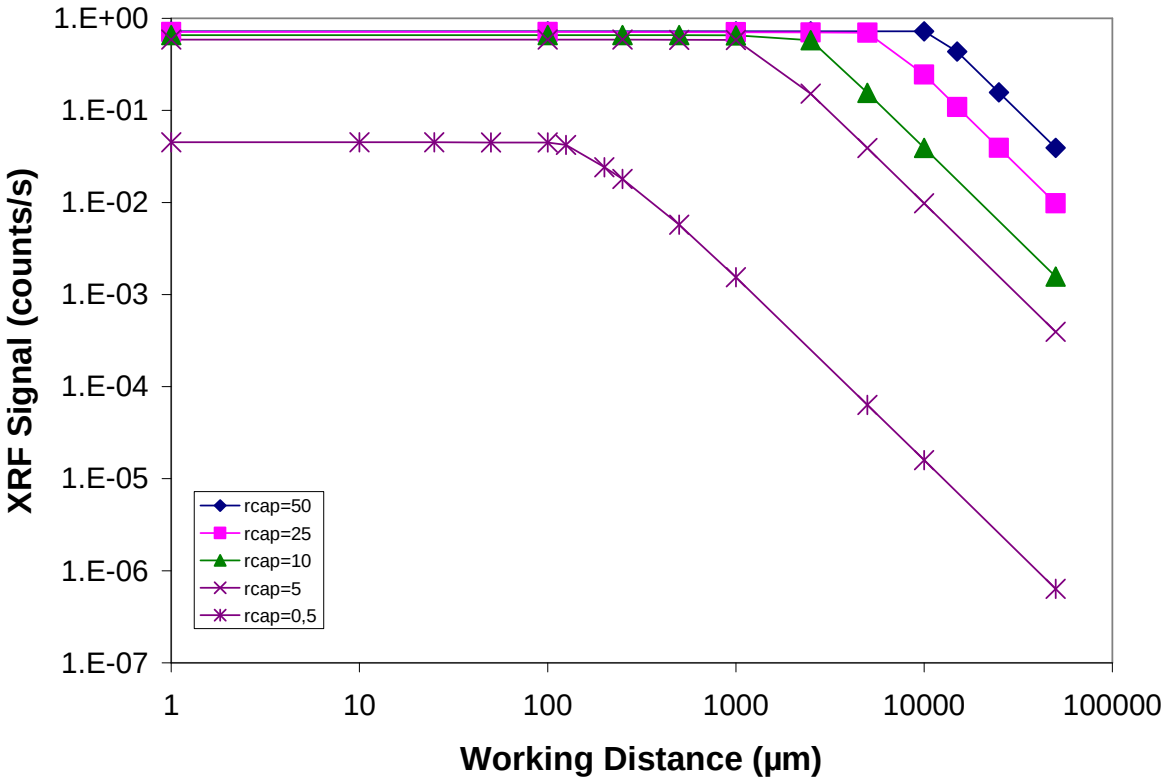

Fig.IV.10 *Variation of the simulated XRF signal from A- type cells (aligned along the capillary axis) with the working distance. The capillary length is 20mm. The line is a guide to the eyes*

In fact, as shown in Fig.IV.11 in the case of a point source, the collected signal is independent of the capillary radius providing the working distance remains smaller than WD_c. WD_c can be calculated for each capillary radius from eq IV.21. Among the WDc values determined for each capillary, the smallest value WD_{cmin}, is 1 mm. This is the reason why we have chosen this WD value in our experiments (see chapter III). Indeed, in this latter case the capillary acceptance is limited by the critical angle θ_c.

The difference between the plateau levels at small WD in Fig. IV.10 has two origins. For the narrowest capillary radius, the cell size had to be decreased in order to remain much smaller than the capillary aperture. This led to a decrease of the absorbing volume of the central cells and thus of the emission level of these A-type cells. Furthermore, the number of X-rays reflections inside a capillary increases as its radius decreases, inducing flux losses increase.

The plateau level difference observed in Fig.IV.8 is due to the fact that the source cannot be considered as punctual for low capillary radii. Indeed, for narrow capillary radii and at low working distances, the X-ray fluorescence zone is partially collected by the detector

through the capillary. Assuming a square lateral profile of the primary beam spot, the plateau magnitude should vary as r_{cap}^{-2}. This dependence is very close from the $r_{cap}^{-1.8}$ actually calculated from Fig. IV.8 variation. The discrepancy is probably due to the Gaussian-shape primary beam lateral profile.

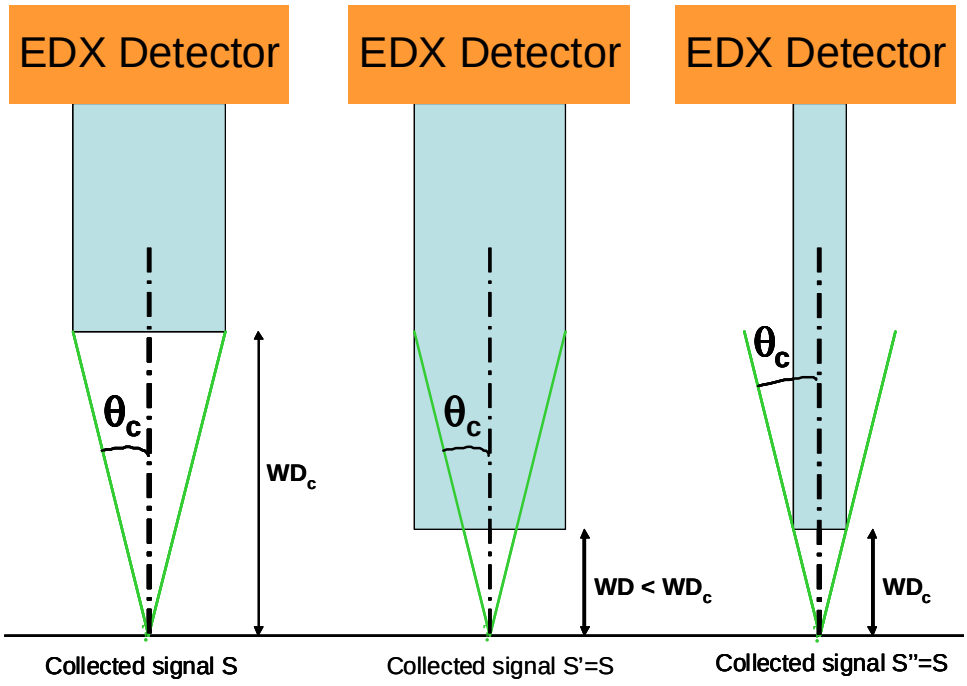

Fig.IV.11 : *fluorescence signal collection through a capillary. The signal collected is independent of the capillary diameter providing the working distance WD is shorter or equal to the critical one* WD_c.

IV.2.2.2: Capillary length influence at constant WD

Figure IV.12 shows the variation of the collected signal with the capillary length for different capillary radii: 0.5, 5, 10, 25 and 50 µm. The working distance is fixed at 1 mm. We can see that the signal transmitted by the capillary decreases as the capillary length increases. This decrease is more drastic at capillary lengths lower than a critical value L_{N1} that depends on capillary radii.

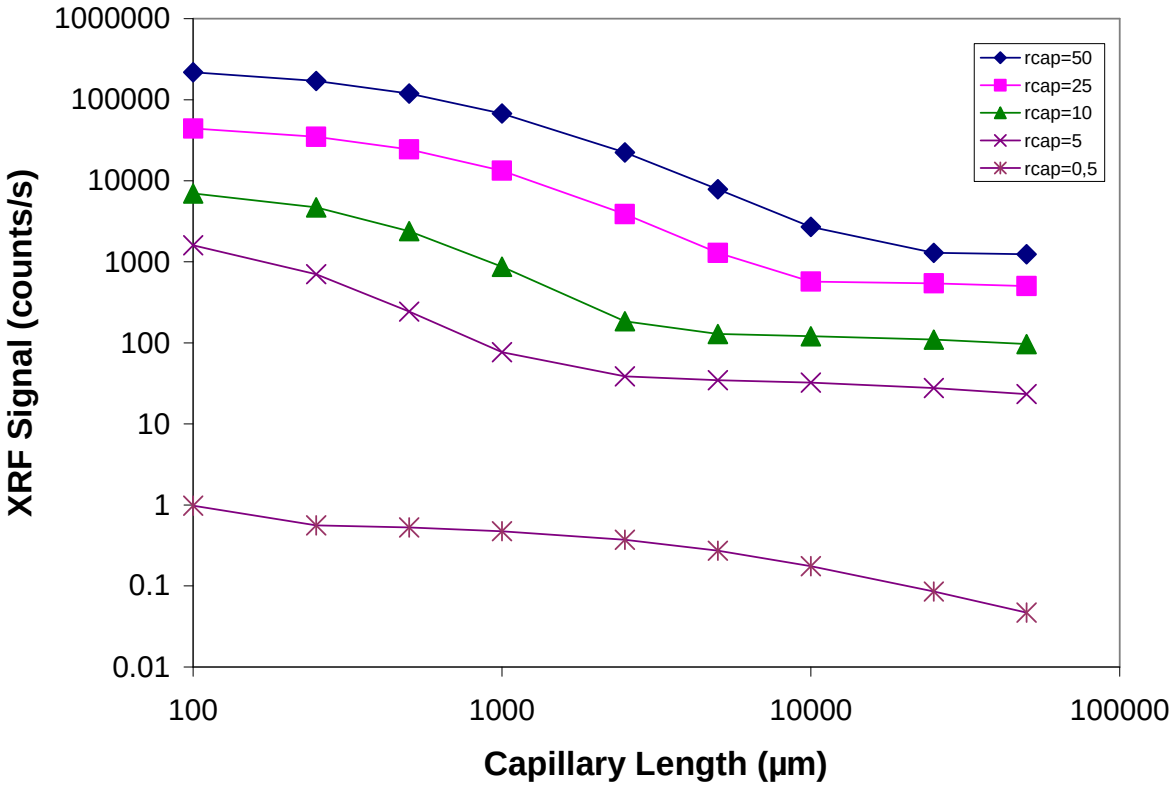

Fig.IV.12: *Calculation of XRF signal level with the capillary length. The working distance is fixed at 1mm. The capillary radius is 0.5, 5, 10, 25 and 50µm. The line is a guide to the eyes*

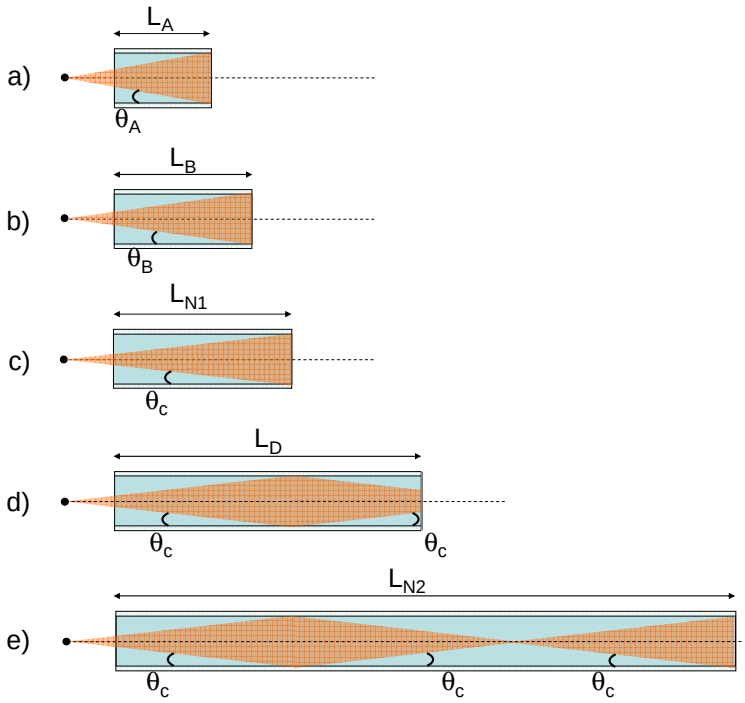

Fig. IV.13: *Scheme of the effective collection solid angle variation with capillary length in the case of X-ray collection from a point emitter.*

Still considering the ideal case of a point source emitter, Fig.IV.13 illustrates the signal dependence on capillary length at constant WD. For very short lengths (L_A, case a) in Fig. IV.13), the incidence angle of X-rays coming from the emitter on the capillary wall is higher than the critical angle θ_c. These rays are not reflected and consequently only the rays that do not impinge on the inner wall are detected: the capillary acts as a simple pinhole. If the capillary length is slightly increased (from L_A to L_B, case b) Fig.IV.13), providing the angle under which the capillary rear aperture is seen from the emitter has a value higher than θ_c, the signal decreases because the detector is moved away from the emitter: the signal is expected to decrease as the reciprocal $(L+WD)^2$.

When the capillary length reaches the value such as:

$$L = L_{N1} = \frac{r_{cap}}{\tan\theta_c} - WD \qquad \text{Eq (IV.23)}$$

the capillary rear aperture is seen from the point emitter exactly under the angle θ_c (Fig. IV.13 case c)), and the signal level is expected to be lower than in Fig. IV.13b). A further capillary increase ($L_D > L_{N1}$, Fig.IV.13d)) should have no influence on the signal magnitude collected, since the effective collection angle remains constant and equal to θ_c. The signal level is thus expected to remain constant for longer capillaries. The values for L_{N1} are 0.2, 1.3, 4.8 and 11.2 mm for 5, 10, 25, 50 µm radii capillary respectively at 1mm WD**.** Those values are in good agreement with those found in Fig. IV.14 where A-type cells fluorescence collected signal variation is presented as a function of capillary length. This is due to the fact that the whole set of those cells almost acts as point source. However, the L_{N1} do not correspond with those found in Fig. IV.12 because in this latter case the emitter is an extended source and B-type as well as C-type cells are taken into account.

According to equation IV.20, the longer is the capillary, the higher is the gain in signal collection. However, the gain is obviously not the relevant parameter because it is a comparison with the signal collection through a pinhole of same diameter. Indeed, we can obviously observe on Fig.IV.12 that the collected signal decreases when the capillary length increases. This can be explained by the loss of signal due to higher number of reflections inside the capillary as its length increases. An illustration of this effect is given in the following example. When the capillary is longer than a value L_{N2} given by (see Fig. IV.13e)):

$$L_{N2} = 3\,L_{N1} + 2WD \qquad \text{Eq (IV.24)}$$

the extreme rays are transmitted to the detector after two reflections on the capillary wall. Due to the signal losses at each extra reflection, the signal is expected to decrease.

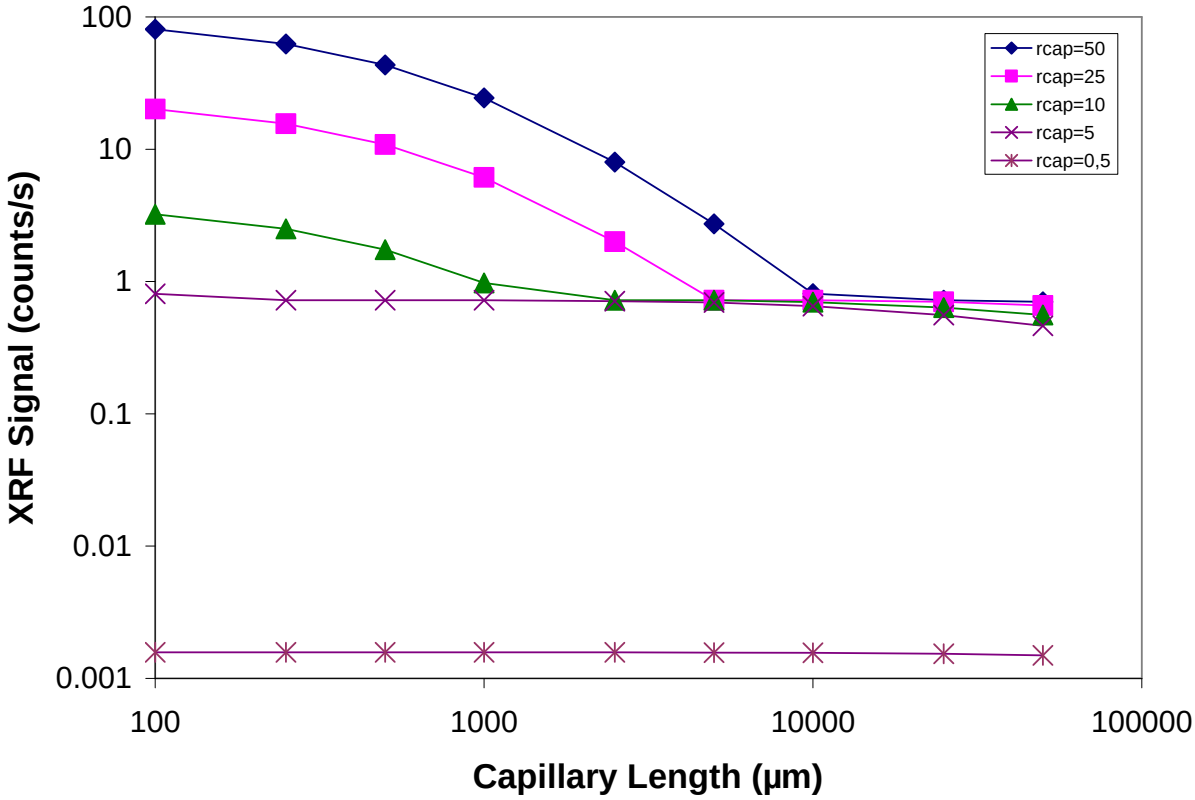

Fig.IV.14: *Variation of the XRF signal collected from A- type cells (aligned along the capillary axis) with the capillary length. The working distance is fixed at 1mm. Each line corresponds to a given capillary radius from 0.5µm to 50µm.*

IV.2.3: Resolution that can be expected in µ-XRF with our test-bed

For a given capillary radius, since the signal does not depend on the WD providing WD < WD_c, it seems more comfortable to position the capillary extremity just at WD_c from the sample surface. However, a part of the signal is collected from areas surrounding the capillary aperture surface projection on the sample due to the critical angle of X-ray reflection on the capillary inner wall. The lateral resolution R of the analysis technique is thus given by:

$$R = 2\,[r_{cap} + WD\,\tan(\theta_c)] \qquad \text{Eq (IV.25)}$$

The lateral resolution of the technique is thus improved as WD is decreased. On the other hand, as we approach the capillary extremity toward the surface, the signal magnitude decreases because the number of detectable emitting unit cells decreases (Fig IV.15a)). As seen in Fig.IV.8, the collected signal increases when the capillary is approached towards the surface until the WD_c value is reached. At this WD value the resolution is 4 r_{cap} (see Eq IV.21 and Fig.IV.15b)). Approaching the capillary has a slight effect on the collected signal level, but it improves the lateral resolution, because less C-type cells are involved in the detected signal (Fig.IV.15c)). We show in Fig.IV.16 the proportion of the fluorescence signal that is

collected from C-type emitting cells alone. The lower is this proportion the better is the lateral resolution. We can thus define an ideal working distance WD_i below which 99% of the collected signal comes from front cells (A- and B-type cells). Table IV.4 shows the values of WD_i and WD_c for the different capillary radii investigated. We can see that the ideal working distance WD_i is significantly smaller than WD_c.

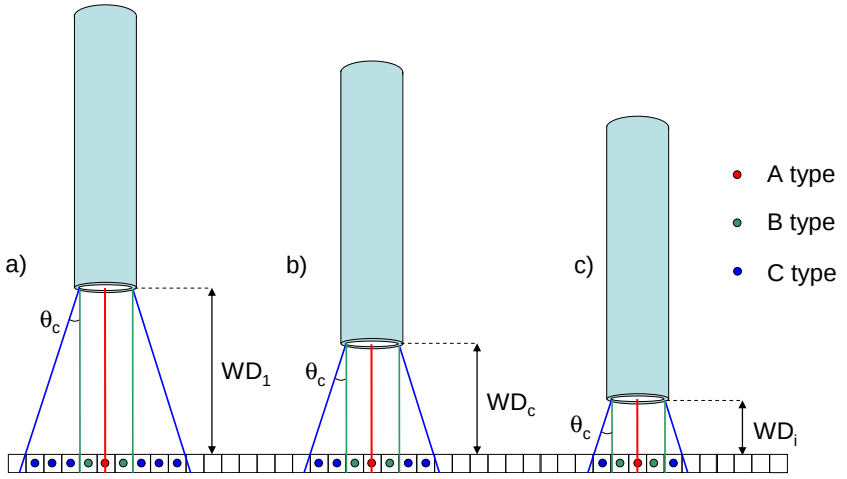

Fig IV.15 : *Scheme of the lateral resolution variation as a function of WD.*

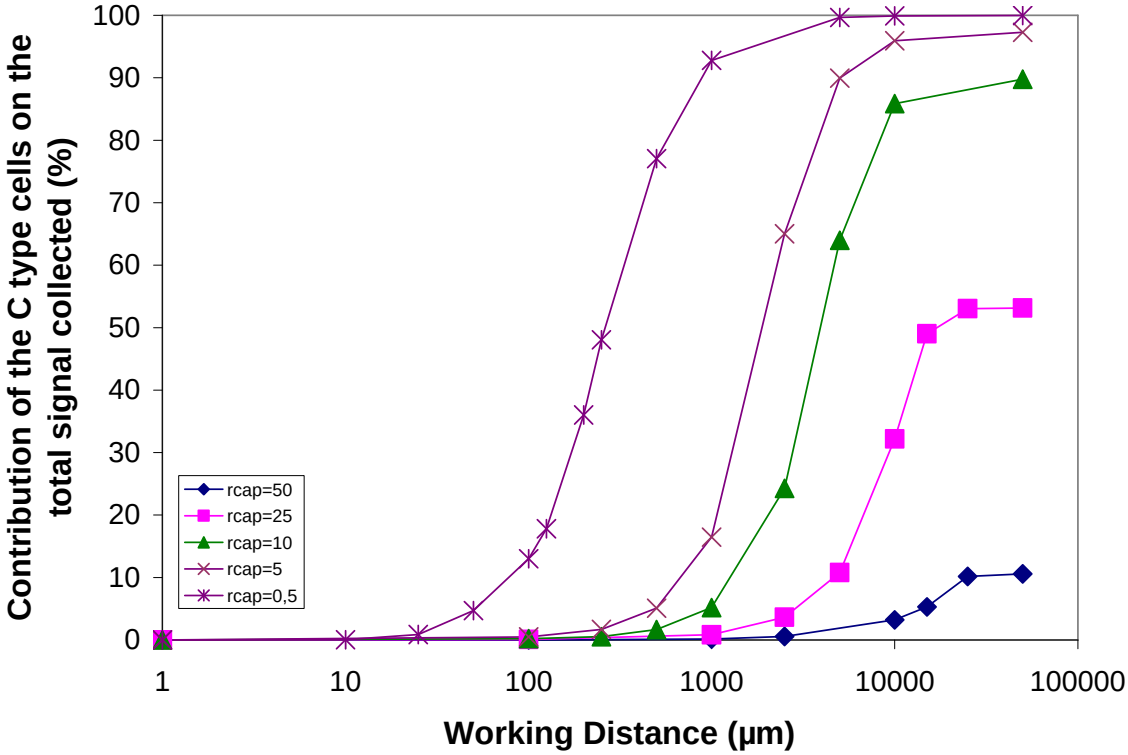

Fig.IV.16*: Contribution of the C-type cells on the total signal collected as a function of the working distance. The capillary radius is 0.5, 5, 10, 25 and 50µm. The line is a guide to the eyes*

Capillary radius (µm)	**0.5**	**5**	**10**	**25**	**50**
WD_c (mm)	0.12	1.17	2.34	5.84	11.68
WD_i (mm)	0.027	0.16	0.35	1.10	3.75

Table IV.4: *WD_c and WD_i values as a function of the capillary radius*

Using a 0.5 µm radius cylindrical capillary, simulations show that the best resolution keeping a significant signal/noise ratio is obtained with the following geometrical characteristics:

- capillary length: 20 mm
- working distance: 27 µm

With this configuration we expect a 1 µm lateral resolution for XRF analysis. From preliminary measurements with the 1µm radius capillary, we have demonstrated that this experiment is realistic.

IV.3 Conclusion

Our µ-XRF equipment using capillary optics both on illumination and detection paths has been modelled. Simulations were developed to define the system geometry on the XRF signal level dependence: capillary length and radius, working distance. The goal of this part is the estimation of the ultimate lateral resolution that can be achieved with such a tool. Since commercially available softwares are not suitable for our unusual configuration, we have developed our own program. It is derived from the finite element method and is based on the fundamental parameters equations for the X-ray fluorescence emission.

For a given capillary radius, the signal increases when the working distance decreases down to a critical value WD_c . Above, the signal remains constant. This phenomenon can be explained assuming the fluorescence zone as a point emitter. The collected signal magnitude decreases when the capillary length is increased. This trend is more obvious for wide capillaries. The collected signal magnitude varies as $rcap^{-1.8}$ in good agreement with the expected $rcap^{-2}$ correlation in the case of an homogeneous primary beam profile.

Experimental results are in good agreement with the simulation data.

Moreover, we have shown that it is necessary to approach the capillary toward the surface to increase the lateral resolution. We have calculated the ideal working distance as a function of capillary radius.

Finally, simulations show that a 1µm lateral resolution can be achieved with a 0.5 µm radius and 20 mm length capillary positioned at a working distance of 25 µm from the surface in the same experimental conditions. Using brighter sources (rotating anode, liquid metal jet anode source, synchrotron) would allow to improve substantially the signal/noise ratio, and thus probably even to work with narrower capillaries.

References

[1] A. Firsov, M. Brzhezinskaya, A Firsov, A. Svintsov and A. Erko, “Dedicated software for diffractive optics design simulation, Journal of Physics”, Conference Series 425 (2013) 162004

[2] D. M. Tennant, F. Klemens, A. Taylor, C. Jacobsen, P. L. Gammel, H. Huggins, S. Ustin, G. Bogart and L. Ocola, “Single-element elliptical hard x-ray micro-optics”, Optics Express, vol.11, n°8, 2003

[3] L. Vincze, Janssens. K, Adams. F, “Detailed ray-tracing code for capillary optics”, X-ray spectrometry, vol. 24, 27-37, 1995

[4] A. Liu, “Simulation of X-ray propagation in a straight capillary”, Mathematics and Computers in Simulation 65, 251, 2004

[5] D. Hampai, S. B. Dagabov, G. Cappuccio, G. Cibin, “X-ray propagation through polycapillary optics studied through a ray-tracing approach”, Spectrochimica Acta Part B 62, 608, 2007

[6] B. Lai, F. Cerrina, SHADOW : A synchrotron radiation ray tracing program, Nuclear Instruments and methods in physics research A246 (1986) 337-341

[7]M. Sànchez del rio, New challenges in ray tracing simulations of X-ray optics, Journal of physics: Conference Series 425 (2013) 162003,

[8] F.Cerrina, C.Welnak, G.J. Chen, and M. Sanchez del Rio, Center for X-ray Lithography, University of Wisconsin SHADOW Primer 2.0 CXrL May 19, 1994 Center for X-ray Lithography, University of Wisconsin, available at http://www.esrf.eu/computing/scientific/raytracing/PDF/primer.pdf (last accessed 18/07/2013)

[9]L. Vincze, B. Vekemans, F.E. Brenker, G. Falkenberg, K. Rickers, A. Somogyi, M. Kersten and F. Adams in: “Three-dimensional trace element analysis by confocal X-ray microfluorescence imaging”, Anal. Chem., 76, 6786–6791, 2004

[10] B. Vekemans, L. Vincze, F. Brenker and F. Adams, “Processing of three-dimensional microscopic X-ray fluorescence data”, J. Anal. At.Spectrom., 19, 1302–1308, 2004

[11] Z. Smit, K. Janssens, K. Proost and I. Langus, “Confocal µ-XRF depth analysis of paint layers”, Nucl. Instrum. Methods Phys. Res., B Beam Interact. Mater. Atoms, 219–220, 35–40, 2004.

[12] W. Malzer, B. Kanngieβer, “A model for the confocal volume of 3D micro X-ray fluorescence spectrometer”, Spectrochimica Acta Part B: Atomic Spectroscopy, 60, 9–10, 1334–1341, 2005

[13] D. Sokaras and A.-G. Karydas, “Secondary Fluorescence Enhancement in Confocal X-ray Microscopy Analysis”, Anal. Chem., 81, 4946–4954, 2009 Dimosthenis Sokaras* and Andreas-Germanos Karydas

[14] T. Schoonjans, G. Silversmit, B. Vekemans, S. Schmitz, M. Burghammer, C. Riekel, F.E. Brenker, L. Vincze, “Fundamental parameter based quantification algorithm for confocal nano-X-ray fluorescence analysis”, Spectrochimica Acta Part B, 67, 32, 2012

[15] Baltej Singh Sidhu, A. S. Dhaliwal, K. S. Mann, K. S. Kahlon, “Measurement of K-shell absorption edge jump factors and jump ratios of some medium Z elements using EDXRF technique”, Radiation Physics and Chemistry 80 (2011) 28–32

[16] W. Bambinek, B. Crasemann, R.W. Fink, H.-U. Freund, H. Mark, C.D. Swift, R.E. Price, P.V. Rao, “X-Ray Fluorescence Yields, Auger, and Coster-Kronig Transition Probabilities”, Reviews of Modern Physics, vol.44, 4, 1972

[17] R.W. Fink, R.C. Jopson, H. Mark, C.D. Swift, “Atomic Fluorescence Yields”, Reviews of Modern Physics, 38, 3, 1966

[18] See for example: X-Ray Data Booklet, Center for X-ray Optics and Advanced Light Source, Lawrence Berkeley National Laboratory, 2009, http://xdb.lbl.gov/ (last accessed 18/07/2013).

[19] V. Thomsen, “Basic Fundamental Parameters in X-Ray Fluorescence”, 46 Spectroscopy 22(5), 2007, available at www.spectroscopyonline.com (last accessed 18/07/2013)

[20] A. Bjeoumikhov, S. Bjeoumikhova. (2008), “Capillary Optics for X-Rays”, in Modern Developments in X-ray and Neutron Optics, edited by A. Erko, M. Idir, T. Krist, A.G. Michette, Springer series in Optical Sciences, (Springer-Verlag Berlin Heidelberg) Vol.137, pp. 287-306

[21] http://henke.lbl.gov/optical_constants/ (last accessed 18/07/2013)

Conclusion and Perspectives

1: Main results achieved in photon detection

In this work, we have demonstrated that coupling SPM with X-ray spectroscopies could lead to obtain simultaneous sample topography and luminescence mapping or local spectroscopy of a sample. The experiments were successfully performed with various source types: synchrotron radiation (from a preceding PhD thesis [1]), a He-Cd laser and even a low power micro focused source. The lateral resolution technique is mainly given by the fibre aperture for luminescence (70 nm in our case), and by the fibre apex curvature (100 nm) for topography. These works were supported by two European contracts ('X-Tip' and 'LUMIX', EUREKA # E4383).

Nonetheless, luminescence spectroscopy and mapping limit the chemical analysis to semiconductors. The acquisition of the sample local X-ray fluorescence instead of visible luminescence would significantly enlarge the variety of materials which could be analysed by our instrument. However, we had first to estimate the feasibility of this concept in terms of signal magnitude collected.

We have thus developed a test-bed using the low power microfocused source and a cylindrical capillary equipping a SDD EDX detector. Both optics are positioned in a confocal-like configuration. After source characterization, the capillary used for detection was then scanned across the sample fluorescence emitting volume. The influence of capillary radius on fluorescence signal magnitude collected was studied using capillaries from 50 down to 5 µm radii. X-ray profiling of metallic test patterns were then performed with the setup. These series of experiments demonstrate that local collection of X-ray fluorescence is possible in laboratory with a significant signal/noise ratio. The lateral resolution of the technique depends on the collect capillary radius and on its distance to the sample.

The key issue is the estimation of the ultimate lateral resolution which could be achieved using such a configuration. To answer this question, we developed a simulation program in order to determine the XRF signal magnitude collected through narrower capillaries. The program is derived from the finite element method and is based on the fundamental parameter equations. It was fitted with the experimental test-bed characteristics

(geometry, primary beam characteristics, XRF collection through a cylindrical capillary). The simulation data on a homogeneous sample are in good agreement with the experimental results and the resolution of the technique was discussed. However, is it possible to go further? The simulation program allowed to ensure that 1 µm lateral resolution could be achieved using the low power X-ray micro focused source and an EDX detector equipped with a 0.5 µm inner radius cylindrical capillary, providing it would be 20 mm long and positioned at an ideal working distance below 27 µm. By using a brighter primary source such as a rotating anode or a liquid-metal jet anode electron-impact X-ray source [2], a significantly higher signal can be expected (up to 100 times). Moreover, replacing the cylindrical by an elliptical capillary at the entry of the detector, would lead to an extra gain of 20 on the signal magnitude [3, 4]. Thus sub-micro resolution XRF would be effectively possible with an in-lab excitation source. Of course, working with a synchrotron source would lead to higher signal magnitude which could allow to shrink further the capillary radius and a sub-100 nm lateral resolution could probably be reached.

2: Perspectives

This work opens the way toward the coupling between local XRF analysis and Shear Force Microscopy. The idea is to replace the sharp optical fibre of the home built SNOM head by an X-ray capillary. However, in this case, it should be approached in mechanical near-field interaction with the sample. A 100nm working distance should be possible by adding a polymer apex at the capillary extremity. Indeed, the topography could be performed by this apex while X-rays could be easily collected because polymer is nearly transparent to X-rays (see Fig.C.1).

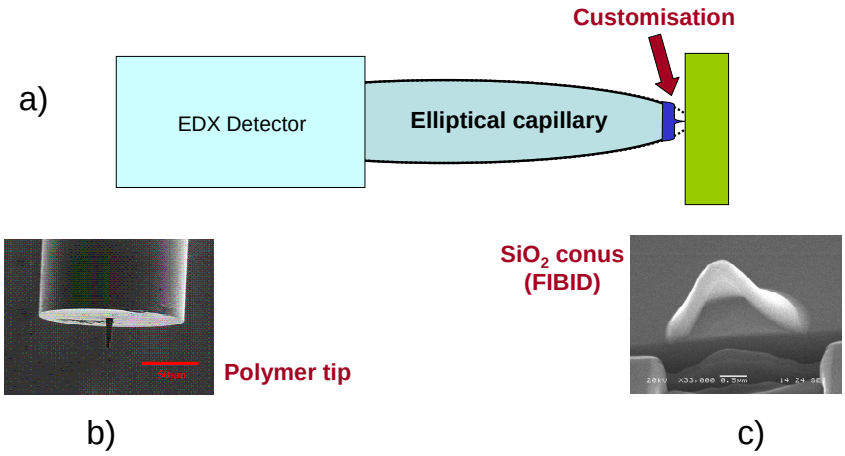

Fig C.1: *(a)The XRF collection is operated through an elliptical capillary customized with a polymer apex used as near-field microscope probe; (b) Example of polymer apex added to a*

photonic optical fibre (courtesy to LovaLite SA); (c) SiO_2 conus grown by Focused Ion Beam Induced Deposition (courtesy to H. Dallaporta, CINaM laboratory) .

Another configuration would consist in using the capillary to excite the sample while X-ray fluorescence would be collected in a classical configuration. The capillary will then provide both primary illumination and SPM measurements (Fig C.2). The capillary needs customization as explained above.

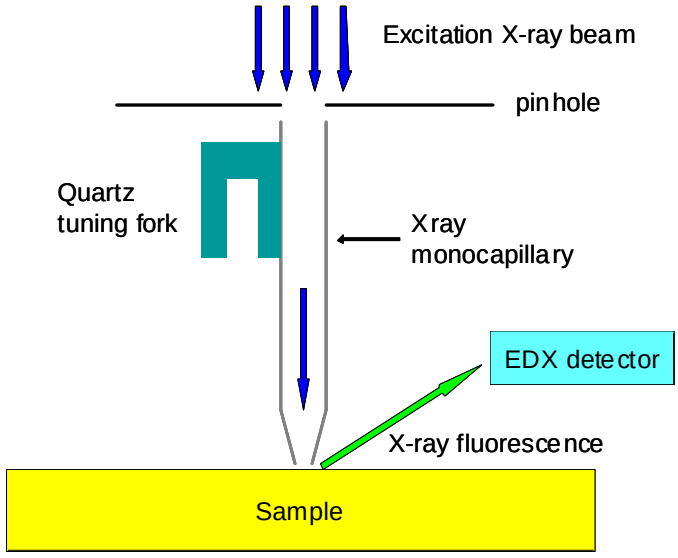

Fig C.2: *Other possible configuration of the instrument. In this case, the sample is locally excited through an X-ray mono-capillary acting both as primary beam focusing and as proximal probe SPM tip. The XRF signal emitted by the sample is collected in classical configuration. To fit with SFM requirements the capillary extremity must be functionalized.*

The ideal test-bed geometry defined by numerical calculations must be tested to define the experimental conditions allowing to achieve 1 µm resolution with the low power micro-focused source. Experiences could also be performed on a synchrotron beamline to determine the ultimate lateral resolution of the technique. Then, the home-made SNOM head should be adapted to fit with XRF signal acquisition with an elliptical capillary and the ultimate resolution might be evaluated. All these measurements might be compared to numerical calculations.

The software is also suitable for multi-element sample analysis. Extra calculations must be launched to define the technique sensitivity with sample characteristics (matrix, inclusions, depth, …).

References

[1] S. Larcheri, “Joint use of x-ray synchrotron radiation microbeams and tip-assisted photon detection for nano-scale XAFS spectroscopy and chemically sensitive surface mapping”, Università Degli Studi di Trento, Italia, 2007, thesis

[2] O. Hemberg, M. Otendal and H.M. Hertz, “Liquid-metal-jet anode electron-impact X-ray source”, Appl Phys Lett, 83, 7, 1483, 2003

[3] A. Bjeoumikhov, S. Bjeoumikhova, R. Wedell, “Capillary optics in X-ray Analytics”, Part Part Syst Char, 22, 384–390, 2006

[4] A. Bjeoumikhov, N. Langhoff, S. Bjeoumikhova, R. Wedell, “Capillary optics for micro x-ray fluorescence analysis”, Rev Sci Instrum, 76, 063115-1–063115-7, 2005

ANNEX

The key of the collected fluorescence signal magnitude estimation remains in the calculation of the effective collection solid angle Ω under which each unit cell emits within the capillary acceptance. It is limited by the fluorescence X-rays impinging the capillary inner wall under an incidence lower than the critical angle θ_c or by the capillary aperture. Moreover, it strongly varies with the position of the emitting cell centre regarding the capillary axis and with WD, the capillary extremity to sample distance.

In the following:

r_{cap} is the capillary radius

WD is the working distance

L is the capillary length

θ_c is the glass critical angle

We must consider three types of cells: A-type cells aligned with the capillary axis, B-type cells inside the cylinder defined by the capillary and other cells called C-type cells.

A-type cells

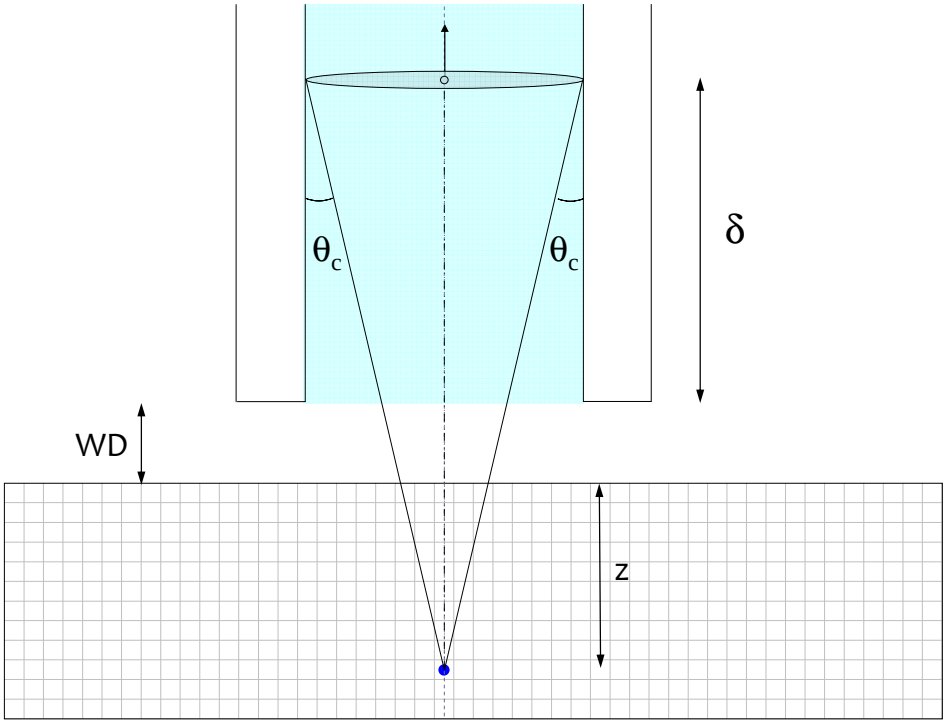

Fig. A1: *System cross section presenting the case of fluorescence collection from A-type cells. Here the collection angle is limited by* θ_c.

Concerning the cells aligned with the capillary axis (A-type cells), for small WD values, the capillary partially transmits the input X-ray beam flux (see Fig. A1). The effective solid angle is limited by glass critical angle θ_c. The capillary section is $S = \pi.r_{cap}^2$, and for those cells the effective solid angle Ω is:

$$\Omega = \frac{\pi.r_{cap}^{\,2}}{\left(\frac{r_{cap}^{\,2}}{\tan^2(\theta_c)}\right)} = 2\,\pi\,(1-\cos\theta_c) \approx \pi\,\theta_c^{\,2} \qquad \text{Eq (A.1)}$$

For values of WD + z so that $\frac{r_{cap}}{WD+z} < \tan(\theta c)$ then,

$$\Omega = \frac{\pi.r_{cap}^{\,2}}{(WD+z)^2} = 2\,\pi\,(1-\cos\theta) \approx \pi\,\theta^2 \approx \pi\tan^2\theta \qquad \text{Eq (A.3)}$$

Where θ is the half angle under which the capillary aperture is seen from the cell and z is the cell depth.

If the capillary length is very short (L < δ with $\delta = \frac{r_{cap}}{\tan(\theta_c)} - WD - z$), the effective surface collection is the output surface of the capillary. In this extreme case, only the rays which reach directly the detector without reflections are detected. The capillary is thus equivalent to a simple pinhole. In this case:

$$\Omega = \frac{\pi.r_{cap}^{\,2}}{(L+WD+z)^2} \qquad \text{Eq (A.4)}$$

The software must account for such case. However, so tiny capillaries have no experimental interest.

B-type cells

For B-type cells (Fig. A.2), Ω defines a slanted conus whose base surface S is tilted with an angle β from the conus axis direction (Fig.A.2).

The effective collection solid angle is given by:

$$\Omega = \frac{S.\cos(\beta)}{r^2} \qquad \text{Eq (A.5)}$$

where r is the distance between the centre of the cell and that of the conus base area.

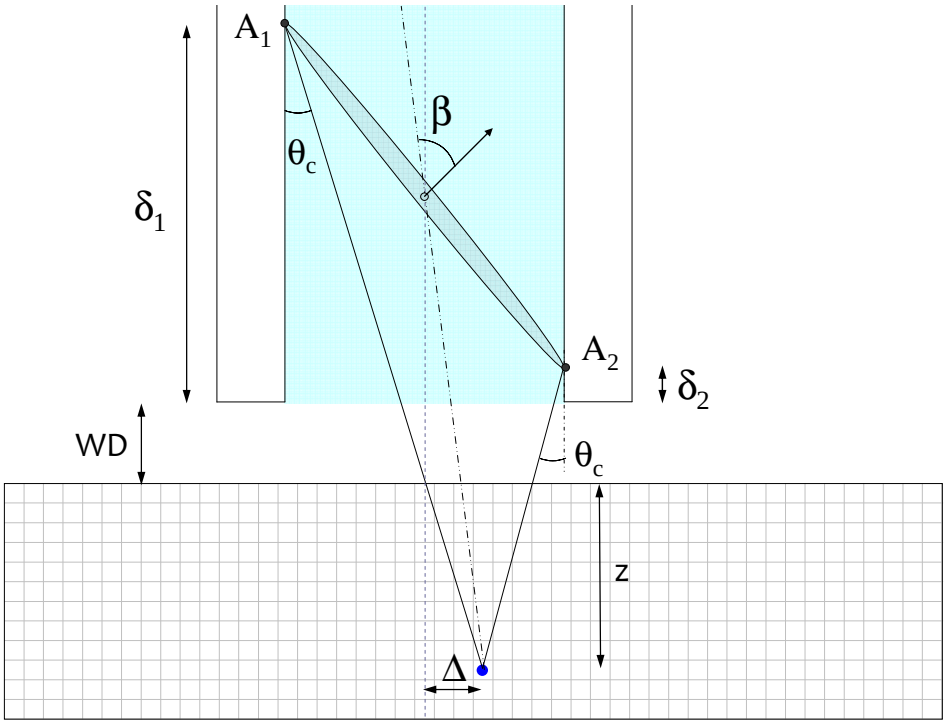

Fig. A2: *System cross section presenting the case of fluorescence collection from B-type cells. Here the collection is not limited by the capillary edge (standard conditions).*

When the capillary acceptance is not limited by the capillary geometrical aperture (standard B-type cells, case presented in Fig. A2), the extreme rays transmitted to the detector have an incidence θ_c all around the inner wall. They impinge the wall at points describing the perimeter of an elliptical conus base, as shown in fig. A.2. A_1 and A_2 correspond to the highest and lowest points. These points are positioned at distances δ_1 and δ_2 from the capillary extremity:

$$\delta_1 = \frac{r_{cap} + \Delta}{\tan(\theta_c)} - WD - z \qquad \text{Eq (A.6)}$$

$$\text{And } \delta_2 = \frac{r_{cap} - \Delta}{\tan(\theta_c)} - WD - z \qquad \text{Eq (A.7)}$$

Where Δ is the distance between the emitted cell centre and the capillary axis.

Ω is calculated from Eq. (A.5). Here S is the surface of the ellipse limited by the points A_1 and A_2, r is the distance between the centre of the emitting cell and the centre of the ellipse, β is the angle between the ellipse normal and the conus axis.

The distance r is easily calculated:

$$r = \sqrt{\Delta^2 + (\frac{\delta_1 + \delta_2}{2} + WD + z)^2} \qquad \text{Eq (A.8a))}$$

The ellipse semi-minor and -major axis are respectively r_{cap} and $\frac{1}{2}\sqrt{(2.r_{cap})^2 + (\delta_1 - \delta_2)^2}$. Thus the elliptic surface area S is given by:

$$S = \frac{1}{2}\pi.r_{cap}.\sqrt{(2.r_{cap})^2 + (\delta_1 - \delta_2)^2} \qquad \text{Eq (A.8b))}$$

The β angle is given by:

$$\beta = \frac{\pi}{2} - Arc\tan(\frac{r_{cap}}{1/2.(\delta_1 - \delta_2)}) + Arc\tan(\frac{\Delta}{WD + z + \frac{\delta_1 + \delta_2}{2}}) \qquad \text{Eq (A.8c))}$$

Finally, the collection solid angle for cells slightly shifted towards the capillary axis (B-type cells) is given by:

$$\Omega = \frac{\frac{1}{2}\pi\ r_{cap}\ .\sqrt{(2.r_{cap})^2 + (\delta_1 - \delta_2)^2}\cos(\beta)}{\Delta^2 + (\frac{\delta_1 + \delta_2}{2} + WD + z)^2} \qquad \text{Eq (A.8d))}$$

Note that A-type cells could be also considered as B type cells with $\Delta = 0$ ie $\delta_1 = \delta_2 = \delta$.

Depending on the capillary length and on the working distance WD, the effective collection angle might be limited by the capillary edge. For example, if WD is increased, δ_2 becomes negative. It means that the signal collection by the right hand side of the capillary (Fig. A.2) is not any more limited by θ_c angle, but by the capillary edge. From a mathematical/numerical point of view, A_2 is located between the capillary entrance and the sample. In this case, we fix $\delta_2 = 0$ in Eq A.8. If WD is still increased, δ_1 becomes also negative ($0 > \delta_1 > \delta_2$). In this other boundary case, we must fix $\delta_1 = \delta_2 = 0$. The collection solid angle is completely limited by the capillary edge:

$$\Omega = \frac{\pi.r_{cap}^{\ 2}.\cos(\beta)}{r^2} \qquad \text{Eq (A.9a))}$$

Where:

$$\beta = \tan^{-1}(\frac{\Delta}{WD + z}) \qquad \text{Eq (A.9b))}$$

And

$$r = \sqrt{\Delta^2 + (WD + z)^2} \qquad \text{Eq (A.9c))}$$

For a fixed WD, If the capillary length L is shrunken so that $\delta_2 < L < \delta_1$, A_1 is not positioned within the capillary length (see Fig. A.3b)), but beyond the capillary rear aperture. In this case we have simply to replace δ_1 by L in the Eq A.8d). If L is still shrunken so that $L < \delta_2 < \delta_1$, the solid angle is now limited by the capillary rear aperture and the value of Ω is given by Eq.A.9a) in which (z + WD) is replaced by (z + WD + L). The capillary length influence on effective collection solid angle is illustrated in Fig A.3.

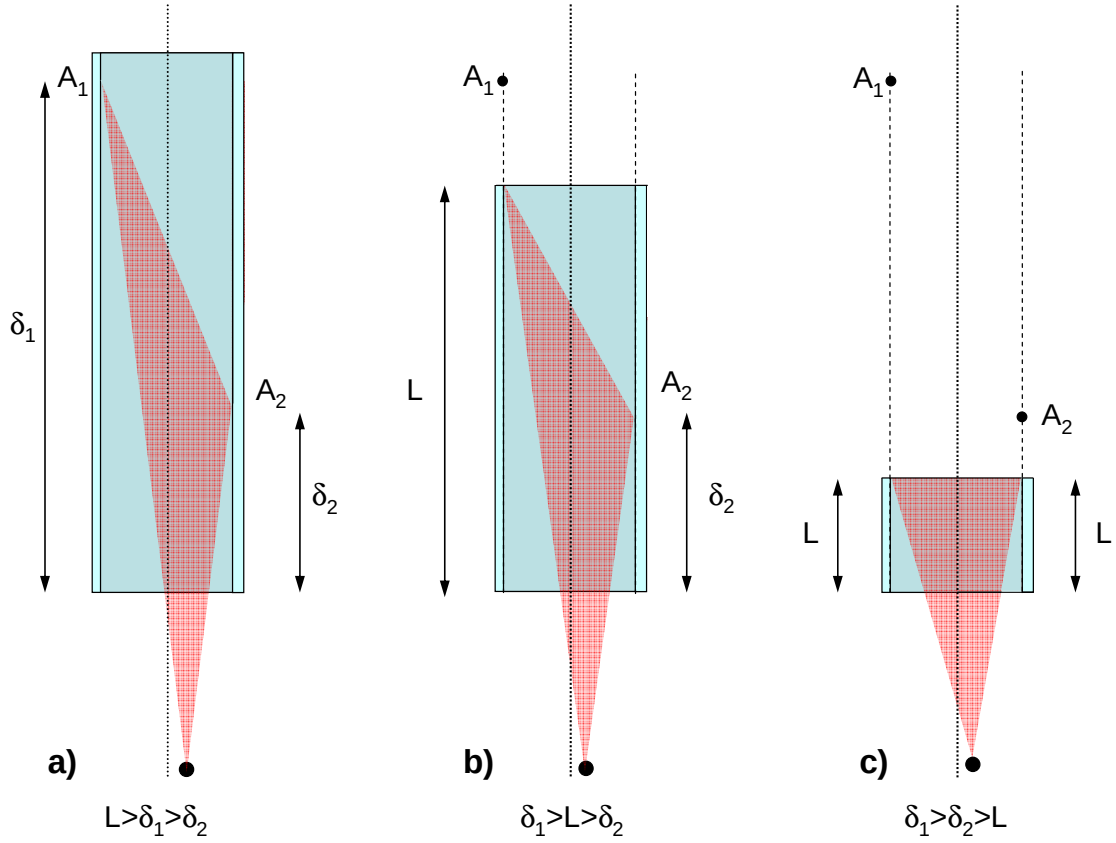

Fig. A.3 : Influence of capillary length L *at fixed WD*. a) Same case as in Fig. A.2. b) L has decreased and point A_1 is beyond the capillary rear aperture. c) For a tiny capillary, the collection solid angle is limited by the capillary rear aperture.

C-type cells

Fluorescence collection from C-type cells is illustrated in Fig.A4.

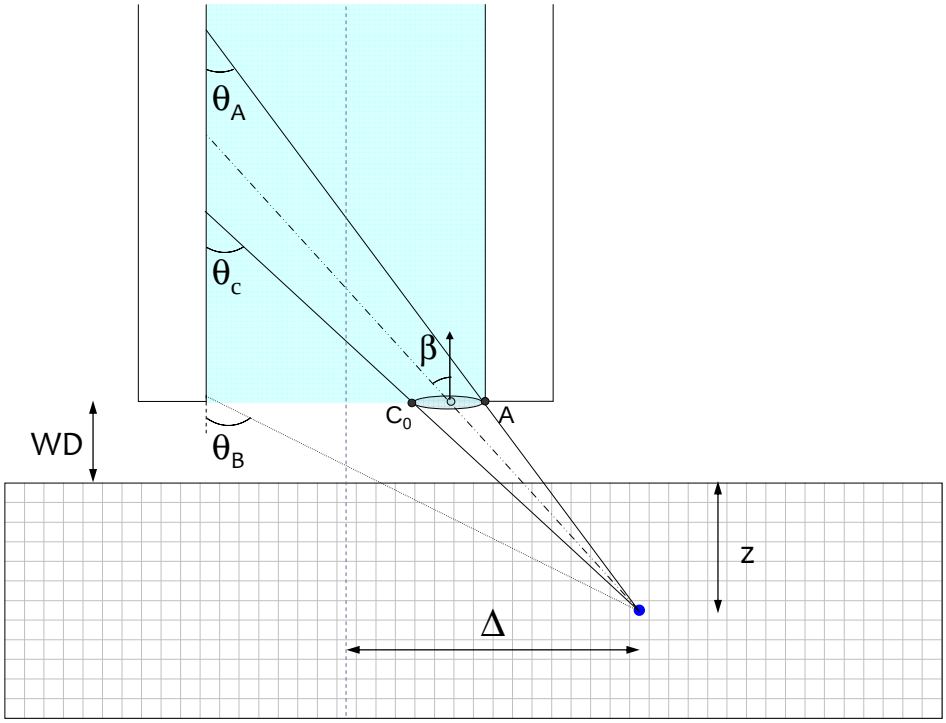

Fig.A.4: *System cross section presenting the case of fluorescence collection from C-type cells.*

All rays enter the capillary under an incidence θ regarding the capillary axis. The rays describe a slanted conus, as shown in Fig. A4. θ is between two extreme values, θ_A and θ_B, with $\theta_A < \theta_B$, given by the following equations:

$$\theta_A = Arc\tan(\frac{\Delta - r_{cap}}{WD + z}) \qquad \text{Eq (A.10a))}$$

$$\theta_B = Arc\tan(\frac{\Delta + r_{cap}}{WD + z}) \qquad \text{Eq (A.10b))}$$

Three cases must be considered.

i) If $\theta_c < \theta_A < \theta_B$ no fluorescence photon can be transmitted to the detector.

ii) If $\theta_A < \theta_B < \theta_c$, the effective collection solid angle is the angle under which the whole geometrical capillary front aperture is seen from the emitting cell:

$$\Omega = \frac{\pi . r_{cap}{}^2 . \cos(\beta)}{\Delta^2 + (WD + z)^2} \qquad \text{Eq (A.11a))}$$

Where:

$$\beta = Arc\tan(\frac{\Delta}{WD+z}) \qquad \text{Eq (A.11b))}$$

iii) If $\theta_A < \theta_c < \theta_B$ only a part of X-ray photons collected by the capillary front aperture will be transmitted to the detector. The collection is limited by θ_c on one side and by the capillary edge on the other side (see Fig. A4). Fig. A5a) presents the system geometry and all the points used for intermediate calculations. P is the plane perpendicular to the capillary axis and positioned at the cell depth z. The distance between this plane and the capillary front aperture is thus WD + z. M Is the emitting cell centre. O is the capillary front aperture centre. O' is its projection on the P plane.

We can now define the area S inside which photons coming from M can be reflected on the capillary wall and guided to the detector. C_0, C_1 and C_2 and A (see Fig. A5a)) are the four extreme points that allow to define this surface. M,A and C_0 are not aligned. MC_0, MC_1 and MC_2 rays impinge the capillary wall under an incidence θ_c. C_1 and C_2 belong to the capillary front aperture edge. C_0 is the point of the capillary aperture surface positioned at minimum distance from point O. A is the point of the capillary edge at minimum distance from M. C_0', C_1', C_2' and A' are the corresponding projections on the P plane. C_0, C_1 and C_2 points satisfy the equation $\|MC_0\| = \|MC_1\| = \|MC_2\| = \frac{WD+z}{\cos(\theta_c)}$.

the intersect between the effective emission solid angle and the capillary aperture defines an area S that does not fill exactly the capillary aperture. Two cases should be considered as shown in Fig. A5b) and c) where S is hatched. Fig. A5b) corresponds to the case described in Fig. A4. S is the sum of two surfaces, one defined by the curve C_1'A'C_2' and the line segment C_1'C_2'; the other by the curve C_1'C_0'C_2' and the line segment C_1'C_2'.This latter surface is assumed to be a semi-ellipse whose surface can be calculated indroducing the angle α equal to (A', O', C_1'). The ellipse major-axis is given by C'$_1$C'$_2$. The minor-axis depends on α angle. If α is lower (respectively higher) than $\frac{\pi}{2}$ it is defined by the difference between the height of the triangle (C_1', O', C_2') and O'C_0'(see Fig. A5b)) (respectively by the difference between O'C_0' and the height of the triangle (C_1', O', C_2'), see Fig. A5c)).

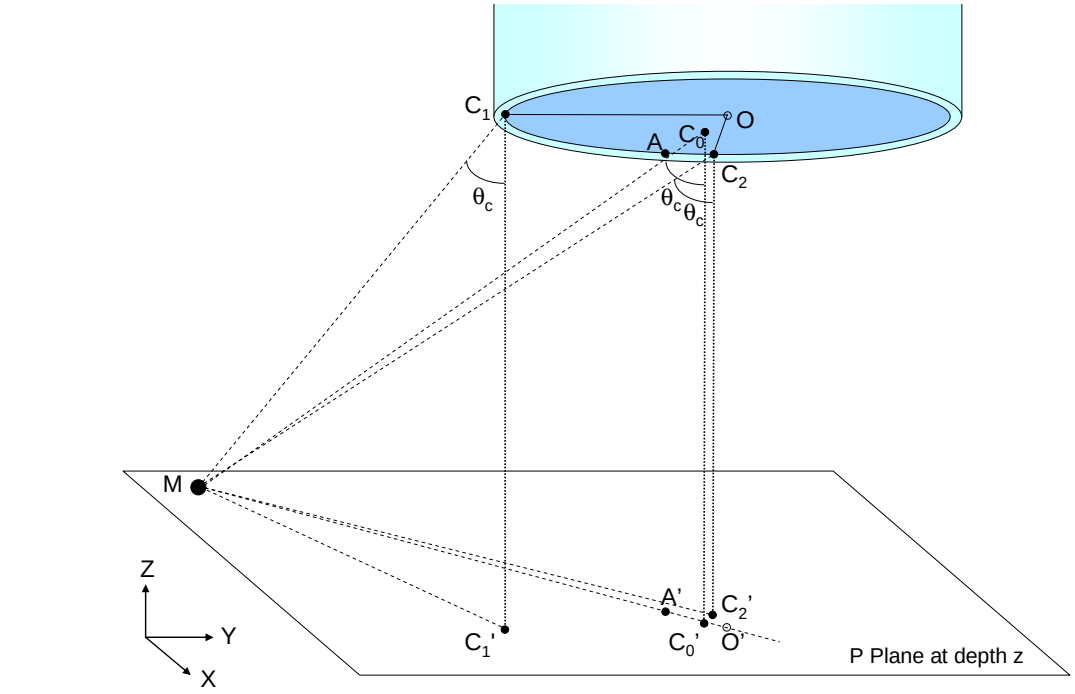

(a)

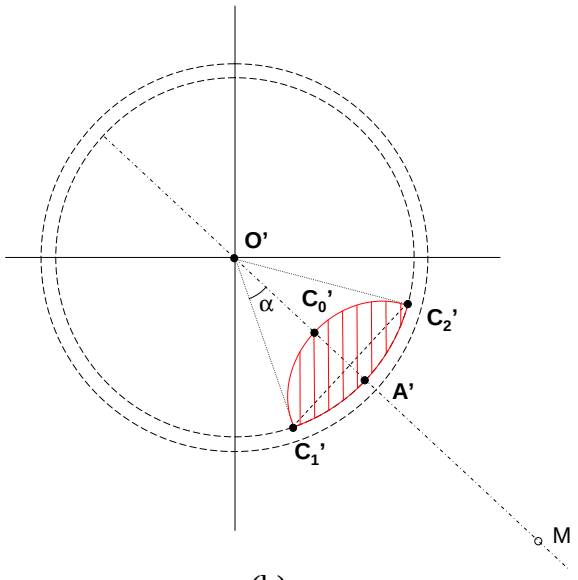

(b)

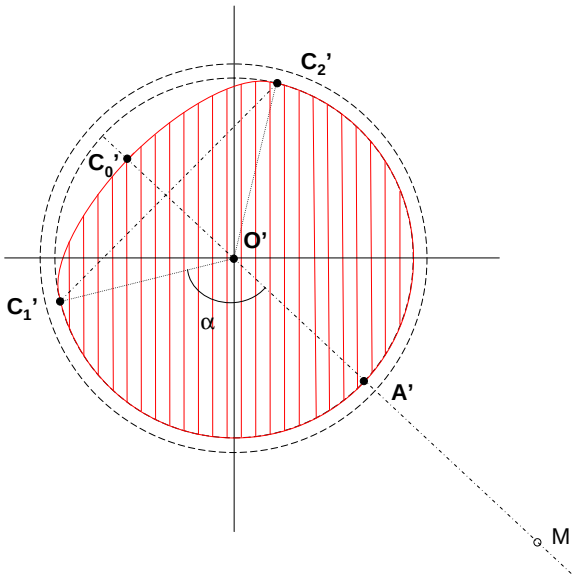

(c)

Fig A.5: *(a) 3D scheme of the collection system. Top view of the collection surface in the P plane for* $\alpha < \frac{\pi}{2}$ *(b) and for* $\alpha > \frac{\pi}{2}$ *(c)*

Still starting from the expression of the solid angle given by Eq (A.5)

$$\cos(\beta) = \frac{WD + z}{r} \qquad \text{Eq (A.12a))}$$

$$r = \sqrt{(WD + z)^2 + (\frac{\Delta - r_{cap} + (\tan(\theta_c).(WD + z))}{2})^2} \qquad \text{Eq (A.12b))}$$

If $\alpha \leq \frac{\pi}{2}$ (Fig (A.5b)) we consider that the effective collection area is given by:

$$S_1 = S_\alpha - S_T + S_E \qquad \text{Eq (A.12c))}$$

Where S_α is the part of the capillary entrance surface delimited by 2α, S_T is the area of the triangle ($O'C'_1C'_2$) and S_E is the half ellipse limited by $C'_0C'_1$ and C'_2.

$$S_\alpha = \pi.r_{cap}{}^2.\frac{2\alpha}{2\pi} = r_{cap}{}^2.\alpha \qquad \text{Eq (A.12d))}$$

$$S_T = \frac{1}{2}\left\|\overrightarrow{C_1'C_2'}\right\|.h \qquad \text{Eq (A.12e))}$$

$$S_E = \frac{1}{2}\pi\frac{\left\|\overrightarrow{C_1C_2}\right\|}{2}(\left\|C_0'O'\right\| - h) \qquad \text{Eq (A.12f))}$$

Where h is the height of the triangle $O'C'_1C'_2$

Then:

$$S_1 = r_{cap}{}^2\alpha + \frac{1}{2}\left\|\overrightarrow{C_1C_2}\right\|[(\frac{1}{2}(\left\|\overrightarrow{C_0'O'}\right\| - h)\pi) - h] \qquad \text{Eq (A.12g))}$$

If $\alpha > \frac{\pi}{2}$ (case presented fig A.5(c)) we have to add all the triangle areas, i.e.:

$$S_2 = S_\alpha + S_T + S_E \qquad \text{Eq (A.12h))}$$

$$S_2 = r_{cap}{}^2\alpha + \frac{1}{2}\left\|\overrightarrow{C_1C_2}\right\|[(\frac{1}{2}(\left\|\overrightarrow{C_0'O'}\right\| - h)\pi) + h] \qquad \text{Eq (A.12i))}$$

Finally:

$$\Omega = \frac{S.(WD + z)}{[(WD + z)^2 + (\frac{\Delta - r_{cap} + (\tan(\theta_c).(WD + z))}{2})^2]^{3/2}} \qquad \text{Eq (A.12j))}$$

Where S = S_1 if $\alpha \leq \frac{\pi}{2}$ and S = S_2 if $\alpha > \frac{\pi}{2}$.

RESUME

Les microscopes en champ proche permettent d'obtenir la topographie d'un échantillon avec une résolution pouvant atteindre la résolution atomique. Ces techniques permettent également d'accéder à certaines propriétés locales de la surface telles que le potentiel, l'élasticité, la densité d'états… Ces spectroscopies locales sont de type 'contraste' et ne permettent pas de dresser la cartographie chimique de la surface sans connaissance a priori des éléments qui la composent.

Les spectroscopies de rayons-X sont des méthodes de caractérisation puissantes qui permettent de déterminer la composition et la structure élémentaire de l'échantillon avec une précision inférieure à l'Ångström. La résolution latérale est essentiellement limitée par la taille du faisceau primaire, couramment de plusieurs µm². Deux voies sont possibles pour l'améliorer:

- réduire l'étendue du faisceau primaire excitateur;
- limiter la collecte du rayonnement émis à une portion du volume excité, tout en approchant le détecteur au maximum pour garder un rapport signal/bruit suffisant.

C'est cette deuxième option que nous avons choisi de développer. Pour cela nous avons collecté localement la luminescence visible issue de l'échantillon par la pointe-sonde d'un microscope à force de cisaillement, constituée d'une fibre optique effilée de faible ouverture. Cette technique a été utilisée pour caractériser des échantillons semiconducteurs micro- et nano-structurés afin d'en obtenir simultanément la topographie et la cartographie de luminescence locale. Ces résultats ont été obtenus non seulement sur une ligne synchrotron mais également à l'aide d'une microsource de laboratoire équipée d'une lentille polycapillaire.

Afin de pouvoir étendre ce concept à d'autres types de matériaux, la faisabilité de la collecte de la fluorescence X locale a été évaluée avec la microsource. Pour cela la fluorescence X émise par un échantillon de cobalt a été collectée par un capillaire cylindrique équipant un détecteur EDX. L'influence du diamètre du capillaire sur le niveau de signal a été mesurée. Une simulation numérique a été développée afin d'estimer le niveau de signal obtenu en utilisant un capillaire de 1 µm de diamètre et d'optimiser la géométrie du système. En couplant la microscopie en champ proche et l'analyse XRF, à la lumière de ces résultats, il sera possible d'atteindre 100 nm de résolution latérale en environnement synchrotron et moins de 1 µm à l'aide d'une source de laboratoire. Il serait alors possible de sélectionner un objet particulier sur une surface et d'en faire l'analyse élémentaire.

ABSTRACT

Scanning Probe Microscopes allow to obtain sample topography up to atomic resolution. Local surface properties such as potential, elasticity, density of states… can also be determined. However, an a priori knowledge of the sample chemistry is required to completely identify the objects present on the sample surface.

X-ray spectroscopies allow elemental and structural analysis of a sample with accuracy better than 1 Å. The lateral resolution is limited by the primary beam diameter, currently a few µm². Two different ways can be followed to enhance the lateral resolution:

- further primary beam focusing
- detector aperture shrinking to collect the fluorescence coming only from a part of the emitting volume, while keeping a significant signal/noise ratio. This is ensured approaching the detector as much as possible toward the surface.

We have chosen to develop this second option. Local sample visible luminescence is collected through a low aperture sharp optical fibre, probe of a shear force microscope. This technique was used to characterize microstructured semiconducting samples to achieve simultaneously the surface topography and luminescence mapping. The results were obtained using either synchrotron radiation or a laboratory microsource equipped with a polycapillary lens.

To extend this concept to a wider variety of materials, local XRF collection by an EDX detector equipped with a cylindrical X-ray capillary was tested. A cobalt sample irradiated with the microsource was used for technique evaluation. The signal magnitude dependence with the capillary diameter was measured. Modelling and numerical calculations were developed to estimate the signal magnitude that could be detected using a 1 µm diameter capillary. The optimal system geometry was determined. Scanning Probe Microscopy combined to XRF analysis could thereby lead to simultaneous acquisition of sample topography and chemical mapping. The expected lateral resolution using synchrotron radiation is 100 nm while sub 1 µm resolution is realistic with a laboratory source. This technique would allow to point a peculiar micro- or nano-object on the surface and to perform its chemical analysis.